Doctoral theses at NTNU, 2015:77

Tian Li

Gasification of Biomass for Second Generation Biofuel Production

Doctoral Thesis

Tian Li

NTNU
Norwegian University of
Science and Technology
Faculty of Engineering
Science and Technology
Department of Energy and
Process Engineering

Doctoral theses at NTNU, 2015:77

NTNU

ISBN 978-82-326-0810-2 (printed version)
ISBN 978-82-326-0811-9 (electronic version)
ISSN 1503-8181

NTNU – Trondheim
Norwegian University of
Science and Technology

NTNU – Trondheim
Norwegian University of
Science and Technology

Tian Li

Gasification of Biomass for Second Generation Biofuel Production

Thesis for the degree of Philosophiae Doctor

Trondheim, April 2015

Norwegian University of Science and Technology
Faculty of Engineering Science and Technology
Department of Energy andProcess Engineering

NTNU – Trondheim
Norwegian University of
Science and Technology

NTNU
Norwegian University of Science and Technology

Thesis for the degree of Philosophiae Doctor

Faculty of Engineering Science and Technology
Department of Energy andProcess Engineering

ISBN 978-82-326-0810-2 (printed version)
ISBN 978-82-326-0811-9 (electronic version)
ISSN 1503-8181

Doctoral theses at NTNU, 2015:77

Printed by Skipnes Kommunikasjon as

Preface

The doctoral work presented here was carried out at the Norwegian University of Science and Technology (NTNU) under the supervision of Prof. Terese Løvås, Dr. Berta Matas Güell (2012–2014), and Dr. Judit Sandquist (2011–2012).

This work was performed within the Gasification for Biofuels (GasBio) project led by the SINTEF Energy Research and funded by the Research Council of Norway, Statoil Petroleum ASA, Metso, Avinor, and Statkraft. Support was also provided through the Combustion Institute and Sandia's Laboratory Directed Research and Development (LDRD) program.

Abstract

Gasification of biomass is perceived as one of the most attractive thermochemical processes to produce carbon neutral syngas that can be burned to release energy or used as the building blocks for the production of value-added chemicals, especially liquid fuel in the heavy transport sector. In the present thesis, both experimental and numerical approaches were applied to investigate the behavior of biomass gasification at high temperature and high heating rate conditions.

Devolatilization of biomass and conversion of solid char are two most important steps in the gasification process. In order to assess the behavior of the rapid devolatilization of biomass, biomass particles (forest residue, torrefied forest residue, Norwegian spruce, and torrefied Norwegian spruce) were subjected to devolatilization experiments at 1073 K and 1473 K in an electrical heated drop tube reactor (DTR). A computational fluid dynamic (CFD) simulation with a proposed two-competing rate devolatilization model was also performed and compared to the experimental results. The conversion behavior of forest residue char and torrefied forest residue char were further examined under oxidation and gasification conditions at 1473 K and 1573 K in the same DTR. The morphological analysis of the parent biomass and corresponding char were showed. In addition, time-resolved data on compositional transformation of the biomass and char were presented based on the metal tracer technics.

In parallel, Eulerian–Lagrangian CFD models were developed to study the overall gasification process in two types of reactors: entrained-flow reactor (EFR) and fluidized-bed reactor (FBR). Comprehensive CFD simulations were conducted to evaluate the performance of biomass gasification in an EFR operating at 1273-1673 K. The model was validated against a wide range of experimental data. Several influential factors including reactor temperature, steam/carbon molar ratio, excess air ratio, biomass type, and particle size were discussed. Regarding the FBR, particle flow pattern, bed expansion, bed pressure drop and fluctuation frequency were compared by using three different well-known inter-phase drag force correlations in a non-reactive condition. Steam gasification in FBRs was analyzed by the CFD model developed from a non-reactive study. Both qualitative and quantitative results were presented to reveal the effects of reactor temperature, steam/biomass ratio, and biomass injection position on gasification of biomass.

List of Selected Publications

The thesis is based on work presented in the following papers, referred to in the text by Roman numerals:

I. **Tian Li,** Liang Wang, Xiaoke Ku, Berta Matas Güell, Terese Løvås, Christopher R. Shaddix.
Experimental and modeling study of the effect of torrefaction on the rapid devolatilization of biomass.
Submitted to Energy & Fuels.

II. **Tian Li,** Manfred Geier, Liang Wang, Xiaoke Ku, Berta Matas Güell, Terese Løvås, Christopher R. Shaddix.
Effect of torrefaction on physical properties and conversion behavior of high heating rate char of forest residue.
Energy & Fuels, **29***,* 177-184, (**2015**).

III. Xiaoke Ku, **Tian Li**, Terese Løvås.
Eulerian−Lagrangian Simulation of Biomass Gasification Behavior in a High-Temperature Entrained-Flow Reactor.
Energy & Fuels, **28**, 5184–5196, **(2014**).

IV. Xiaoke Ku, **Tian Li**, Terese Løvås.
Influence of drag force correlations on periodic fluidization behavior in Eulerian–Lagrangian simulation of a bubbling fluidized bed.
Chemical Engineering Science, **95**, 94–106, **(2013**).

V. Xiaoke Ku, **Tian Li**, Terese Løvås.
CFD–DEM simulation of biomass gasification with steam in a fluidized bed reactor.
Chemical Engineering Science, **122**, 270–283, **(2015**).

Author's Contribution

The papers are co-authored. The author of the thesis has performed the following work for the presented papers:

Paper I. Planning the experiments, performing the fuel preparation (expect for the torrefaction), the rapid devolatilization experiments, the SEM measurements, the TGA measurements, the ash tracer calculation, the kinetic calculation, and the CFD simulation. The author was responsible for writing paper with interpretation of the results and discussion.

Paper II. Planning the experiments, performing the fuel preparation (expect for the torrefaction), the char reactivity experiments, the SEM measurements, the TGA measurements, the ash tracer calculation, and the CFD simulation. The author was responsible for writing paper with interpretation of the results and discussion.

Paper III. Co-developing OpenFOAM code with comparison study in Ansys Fluent, implementation of sub-model, and determination of model parameters (especially with turbulent model and reaction model). The author was directly involved in co-authoring and revising paper with interpretation of the results and discussion.

Paper IV. Co-developing OpenFOAM code with comparison study in MFiX, implementation of sub-model, and determination of model parameters. The author was directly involved in co-authoring and revising paper with interpretation of the results and discussion.

Paper V. Co-developing OpenFOAM code with model implementation and determination of model parameters (especially with turbulent model and reaction model). The author was directly involved in co-authoring and revising the paper with interpretation of the results and discussion.

Additional Publications and Presentations

Journal Papers

VI. **Tian Li**, Lihao Zhao, Xiaoke Ku, Helge I. Andersson, Terese Løvås.
Numerical investigation on turbulent dispersion of particles in channel flow.
Thermal Science, **16**, 1510–1514, **(2012)**.

VII. Xiaoke Ku, **Tian Li**, Terese Løvås.
Eulerian–Lagrangian simulation of a bubbling fluidized bed reactor: Assessment of drag force correlations.
Thermal Science, **16**, 1442–1445, **(2012)**.

Conference and Presentation

VIII. Liang Wang ,**Tian Li**, Berta Matas Güell, Terese Løvås, Judit Sandquist.
An SEM–EDX Study of High Heating Rate Chars of Forest Residues. (*Paper*/*Oral presentation*)
The 7th International Conference on Applied Energy, Abu Dhabi, United Arab Emirates, 28–31 March 2015.

IX. **Tian Li**, Xiaoke Ku, Terese Løvås.
CFD modelling of soot formation in high-temperature lignocellulosic biomass entrained flow gasifier. (*Abstract/Poster*)
34th International Symposium on Combustion, Warsaw, Poland. 29 July–3 August 2012.

X. Xiaoke Ku, **Tian Li**, Terese Løvås.
Euler–Lagrangian simulation of biomass gasification in a high-temperature entrained flow reactor. (*Abstract/Poster*)
34th International Symposium on Combustion, Warsaw, Poland. 29 July–3 August 2012.

XI. **Tian Li**, Lihao Zhao, Xiaoke Ku, Helge I. Andersson, Terese Løvås.
Numerical investigation on turbulent dispersion of particles in channel flow. (*Paper published as paper VI/Oral presentation*)
4th International Symposium on Nonlinear Dynamics, Suzhou, China, 27–30 Oct 2012.

XII. Xiaoke Ku, **Tian Li**, Terese Løvås.
Eulerian–Lagrangian simulation of a bubbling fluidized bed reactor: Assessment of drag force correlations. (*Paper published as paper VII/Oral presentation*)
4th International Symposium on Nonlinear Dynamics, Suzhou, China, 27–30 Oct 2012.

XIII. Xiaoke Ku, **Tian Li**, Terese Løvås.
Eulerian–Lagrangian simulation of wood gasification in a high-temperature entrained flow reactor: effects of biomass type and particle size. (*Paper/Poster*)
6th European Combustion Meeting, Lund, Sweden, 26–28 June 2013.

XIV. **Tian Li**, Liang Wang, Xiaoke Ku, Berta Matas Güell and Terese Løvås.
Effect of torrefaction on rapid devolatilization of biomass. (*Extended abstract/Oral presentation*)
Joint meeting of the British and Scandinavian–Nordic Sections of the Combustion Institute – The 7th Biennial Meeting for the Scandinavian–Nordic Section, Cambridge, UK, 27–28 March, 2014.

XV. Xiaoke Ku, **Tian Li**, Terese Løvås.
CFD–DEM simulation of biomass gasification with steam in a fluidized bed reactor. (*Extended abstract/Oral presentation*)
Joint meeting of the British and Scandinavian–Nordic Sections of the Combustion Institute – The 7th Biennial Meeting for the Scandinavian–Nordic Section, Cambridge, UK, 27–28 March, 2014.

XVI. **Tian Li,** Manfred Geier, Liang Wang, Xiaoke Ku, Berta Matas Güell, Terese Løvås, Christopher R. Shaddix.
Effect of torrefaction on physical properties and reactivity of high heating rate char of forest residue. (*Abstract/Poster*)
35th International Symposium on Combustion, San Francisco, USA, 3–8 August 2014.

XVII. Xiaoke Ku, **Tian Li**, Terese Løvås.
Eulerian–Lagrangian simulation of biomass gasification in a high-temperature entrained flow reactor: effects of biomass type and particle size. (*Abstract/Poster*)

35th International Symposium on Combustion, San Francisco, USA, 3–8 August, 2014.

Table of Contents

Preface i
Abstract ii
List of Selected Publications iv
Author's Contribution v
Additional Publications and Presentations vi
Table of Contents ix
List of Figures xi
List of Tables xii
Abbreviations xiii

Chapter 1 Introduction 1

1.1 Lignocellulosic biomass and torrefaction 1
1.2 Gasification of biomass 2
1.3 Second generation biofuel 6
1.4 Thesis objective 7
1.5 Thesis organization 8

Chapter 2 Literature Review 11

2.1 Devolatilization behavior and pyrolysis kinetics of biomass 11
2.2 Conversion behavior of biomass char 14
2.3 CFD simulation of biomass gasification 17
2.3.1 CFD Simulation of biomass gasification in the fluidized bed reactor 17
2.3.2 CFD Simulation of biomass gasification in the entrained-flow reactor 19

Chapter 3 Experimental Approach 21

3.1 Fuel and pretreatment 21
3.2 Drop tube reactor 22
3.3 Experimental procedures 24
3.3.1 Rapid devolatilization/char production experiments 24
3.3.2 Char gasification and oxidization experiments 24
3.4 Analytical methods 25
3.5 Ash tracer technique 25

Chapter 4 Modeling Approach 27

4.1 Modeling of the drop tube reactor 27
4.2 Modeling of the entrained-flow reactor 29
4.3 Modeling of the fluidized-bed reactor 31
4.3.1 The non-reacting case 31
4.3.2 The reacting case 32

Chapter 5 Summary of Selected Papers 35

5.1 Paper I Experimental and modeling study of the effect of torrefaction on the rapid devolatilization of biomass 35
5.2 Paper II Effect of torrefaction on physical properties and conversion behavior of high heating rate char of forest residue 36
5.3 Paper III Eulerian–Lagrangian simulation of biomass gasification behavior in a high-temperature entrained-flow reactor 37
5.4 Paper IV Influence of drag force correlations on periodic fluidization behavior in Eulerian–Lagrangian simulation of a bubbling fluidized bed. 38
5.5 Paper V CFD–DEM simulation of biomass gasification with steam in a fluidized bed reactor 39

Chapter 6 Recommendations for Further Work 41

References 43

Acknowledgements 51

Selected Papers 53

Appendix: Additional publication

List of Figures

Figure 1-1 Chemical conversion processes involving syngas 4

Figure 1-2 Two main types of FBR 5

Figure 1-3 Two main types of EFR 6

Figure 3-1 Fuel samples used in the experiments.. 22

Figure 3-2 Schematic sketch of the DTR at Sandia National Laboratories.................... 23

Figure 4-1 Three-dimensional computational domain of the DTR 28

Figure 4-2 Schematic of experimental setup 29

Figure 4-3 (a) Three-dimensional (3D) computational mesh for the DTU laboratory-scale entrained-flow reactor and (b) the top view of the reactor inlet 29

Figure 4-4 Geometry of the FBR... 32

List of Tables

Table 1 Properties of biomass fuel 22

Abbreviations

BTL	Biomass-to-liquids
CFD	Computational Fluid Dynamics
DEM	Discrete Element Method
DME	Dimethyl ether
DTR	Drop tube reactor
EBU	Eddy break-up
EFR	Entrained-flow reactor
EHKL	Extended Hill–Koch–Ladd
FBR	Fluidized-bed reactor
FR	Forest residue
HKL	Hill–Koch–Ladd
ICP–MS	Inductively coupled plasma mass spectrometry
ICP–OES	Inductively coupled plasma optical emission spectrometry
IEA	International Energy Agency
LES	Large eddy simulation
MTBE	Methyl tert-butyl ether
NS	Norwegian spruce
PaSR	Partially stirred reactor
RANS	Reynolds-averaged Navier–Stokes
SEM	Scanning electron microscope
SFOR	Single first order reaction
SLPM	Standard Liter per Minute
TFR	Torrefied forest residue
TGA	Thermal gravimetric analysis
TNS	Torrefied Norwegian spruce
UDF	User defined function

Chapter 1

Introduction

1.1 Lignocellulosic biomass and torrefaction

Biomass is an abundant carbon-neutral renewable resource, whose enhanced use would reduce both CO_2 emissions and society's dependence on fossil fuels. Among the various types of biomass, lignocellulosic biomass has attracted significant interest in recent years due to minimal impact on traditional agricultural production and its wide availability, especially in Northern Europe. For example, the potential annual harvest of forest residue (FR) is around 2.7 million m^3 per year in Norway [1]. The Norwegian government has a goal of increasing the use of bioenergy from 14 TWh by 2008 to 28 TWh by 2020, and particular attention has been given to lignocellulosic biomass to meet this target [2]. According to International Energy Agency (IEA), in order to achieve a sustainable development, biofuels, primarily produced from lignocellulosic biomass feedstocks, are expected to replace 25 exajoules of oil products worldwide (the equivalent of total US transport oil demand in 2011) [3]. A large number of studies has been carried out focusing the production of biofuel from the lignocellulosic biomass [4–6]. This will be discussed in more detail later.

Further utilization of lignocellulosic biomass is often limited because of its inherent fuel properties such as low energy density, heterogeneous size and shape, and high moisture content. Torrefaction is a promising approach to upgrade biomass into high quality fuel for efficient thermochemical conversion [7]. During the torrefaction process, biomass is exposed to an inert atmosphere in the temperature range of 473 K to 573 K. Torrefaction can significantly improve the energy density of biomass [8]. Typically for woody biomass, around 30% of the dry mass will be released during torrefaction through torrefaction gases and vapors, which contain only approximately 10% of the initial energy content. The result is an energy densification with a factor of 1.3. Torrefied biomass becomes also hydrophobic and less sensitive to degradation. The presence of OH groups makes raw biomass easy to absorb water [9]. Study shows that torrefied biomass exhibits water repellent properties because of the destruction of OH groups during torrefaction process [10]. In addition, chemical rearrangement reactions occur, causing the formation of nonpolar unsaturated structures, which helps torrefied biomass better withstand biological degradation [11,12]. Another benefit of torrefaction is to increase the grindability of biomass. The breakdown of the hemicellulose matrix and depolymerization of the cellulose during torrefaction decrease the fiber length and reduce its mechanical strength [13,14]. The energy consumption of milling biomass can reduce 70-90% by torrefaction based on the types of biomass and the conditions of torrefaction [12]. Compared to raw material, torrefied biomass is superior in terms of storage, transportation, and energy production [15]. Furthermore, the energy loss associated with torrefaction can be partly recuperated by integrating torrefaction with thermal process technologies such as gasification [16].

1.2 Gasification of biomass

Thermochemical gasification is the conversion process by partial oxidation of a carbonaceous feedstock into a gaseous energy carrier consisting of permanent, non-condensable gases at elevated temperatures [17]. Thermochemical conversion of biomass during the gasification process is complicated and is often described by the following partially overlapping steps [18,19]:

- Drying, during which biomass particles are heated up and liquid water leaves the biomass in the form of steam.
- Thermal decomposition (pyrolysis or devolatilization), during which gases, such as H_2, CH_4, CO,CO_2, H_2O, etc., as well as tar, are released to the surroundings. In

addition, important reactions and transformations take place inside the biomass particle and consequently char is produced.
- Gasification of solid chars, during which part of solid char components react with gases in the surrounding atmosphere and produce syngas.

Gasification of biomass is perceived as one of the most attractive thermochemical processes to produce carbon neutral syngas (mainly consists of CO and H_2) that can be burned to release energy or used as the building blocks for production of value-added chemicals especially liquid fuels in the transport sector. A comprehensive review of technical and economic assessment of biomass-derived syngas to fuels and chemicals can be found by Spath and Dayton [20], which is briefly shown in Figure 1-1. Hydrogen is known as a clean fuel, but the majority of the worldwide hydrogen consumption is for producing ammonia, which is the second largest synthetic chemical product. Currently, the dominant technology for hydrogen production is steam methane reforming. However, syngas produced from biomass contains hydrogen and CO can be further converted to hydrogen through the CO shift conversion, which makes hydrogen production the largest use of syngas. Methanol, one of the top ten chemicals produced globally, can be also synthesized from syngas. The produced methanol can be used as a transportation fuel or an important chemical intermediate for production of formaldehyde, dimethyl ether (DME), methyl tert-butyl ether (MTBE), acetic acid, olefins and so on. A well-developed commercial catalytic process for methanol synthesis from syngas has reached the overall conversion efficiency of 99%. Another synthetic route using syngas is the Fischer–Tropsch process that converts syngas into hydrocarbons over transition metal catalysts. It is a promising source for producing synthetic lubrication oils and liquid synthetic fuel, especially low-sulfur diesel fuel. As shown in Figure 1-1, syngas can be also used for production of alternative fuels, ethanol; octane enhancement additives, mixed higher alcohols; aldehydes and alcohols through hydroformylation of olefins; isobutene and isobutene through isosynthesis.

Various types of reactors have been industrially employed in biomass gasification processes. Commonly, gasifiers can be classified into one of the following categories:
- Moving bed reactor

- Fluidized bed reactor (FBR)
- Entrained-flow reactor (EFR)

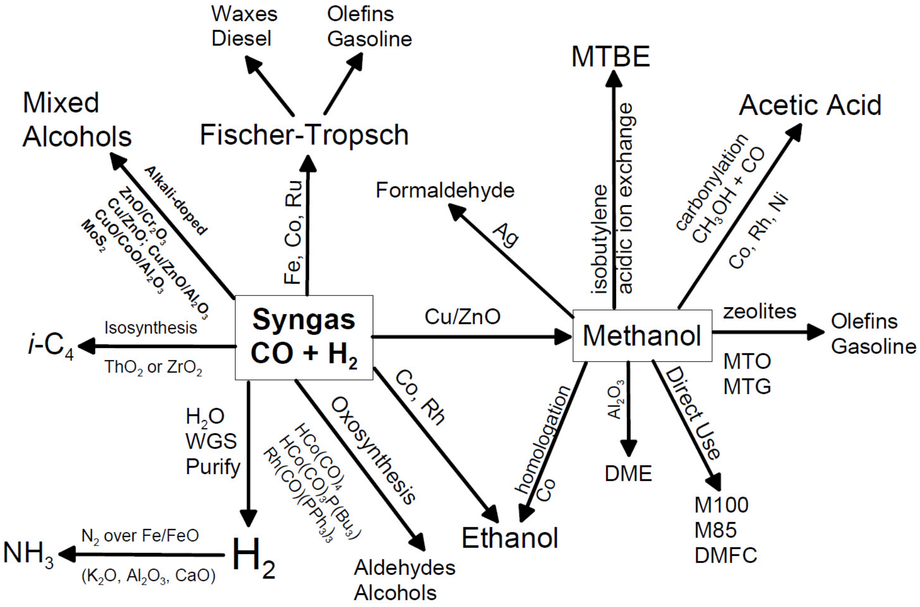

Figure 1-1 Chemical conversion processes involving syngas [20]

Moving-bed reactors have been commonly applied due to their simplicity and degree of controllability [19]. However, the produced syngas would be heavily contaminated with tars in a counter flow moving bed gasifier due to insufficient tar cracking. This tar problem could be reduced in the co-current flow configuration by forcing tar rich gases to cross the combustion region, but the necessity to maintain good control over the blast distribution in the bed restricts this solution to units of very small size [21,22]. Therefore only FBRs and EFRs are considered in this study and a brief description follows.

Typical types of FBRs, namely the bubbling fluidized bed reactor and circulating fluidized bed reactor, are illustrated in Figure 1-2. The FBR offers excellent mixing between feed and oxidant, which promotes both heat and mass transfer. Hence, a wider range of fuels or a mixture of them can be gasified. This feature is especially attractive for biomass fuels, such as agricultural residues and wood, that may be available for gasification at different times of the year. For these reasons, many developmental activities on large-scale biomass gasification are focused on the fluidized bed technologies. FBRs typically operate in relatively low temperatures (800 to 1000 °C) restricted by the softening point of ash to avoid ash agglomeration. However, this places a limitation on the carbon conversion of the fluid-bed processes since the carbon conversion ratio is highly temperature dependent. In addition, tar contamination is unavoidable due to the comparatively low operating temperatures.

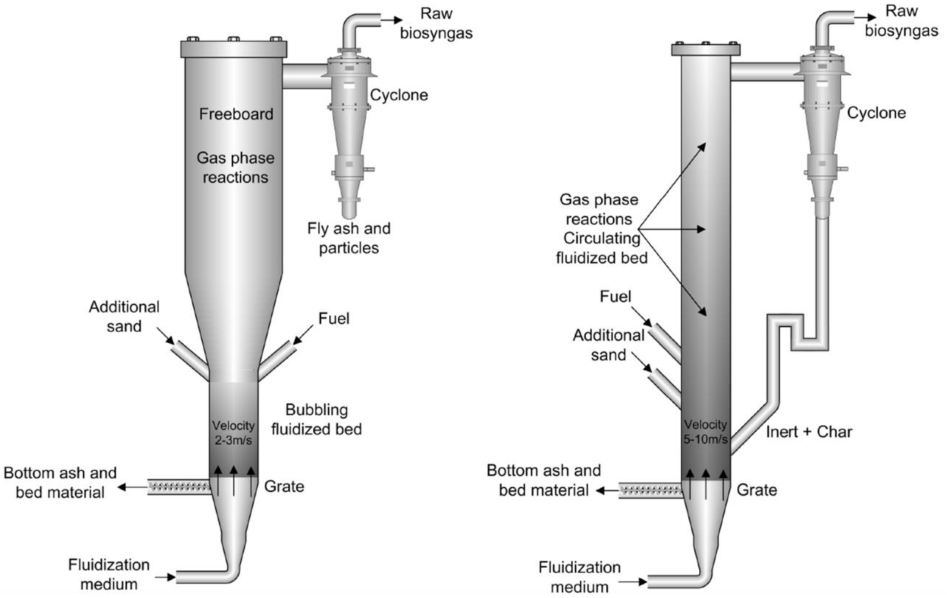

Bubbling fluidized bed reactor **Circulating fluidized bed reactor**

Figure 1-2 Two main types of FBR [22]

Two types of EFRs which operates either with bottom-feeding or top-feeding are shown in Figure 1-3. The powdered fuel is injected into the reactor chamber along with gasification agents such as air, oxygen, or steam. Upon the releasing of volatiles, violent reactions occur among gasification agents, volatiles and char. Benefiting from the high operating temperature, a very high level of carbon conversion with clean, tar free syngas can be achieved with the EFR. In addition, EFRs are attractive for large scale systems. Despite all the advantages mentioned above, a special attention needs to be paid when using biomass in such reactors. Due to the short residence time of the fuel particles, significantly small sizes of particles are required for promoting heat and mass transfer in an EFR. Certain pretreatment methods, like torrefaction, are needed for an economical reduction of the particle size for biomass as mentioned in the section 1.1. Furthermore, the aggressive nature of molten slag (such as alkali metal chlorides) from biomass ash will cause corrosion of reactor lining [23].

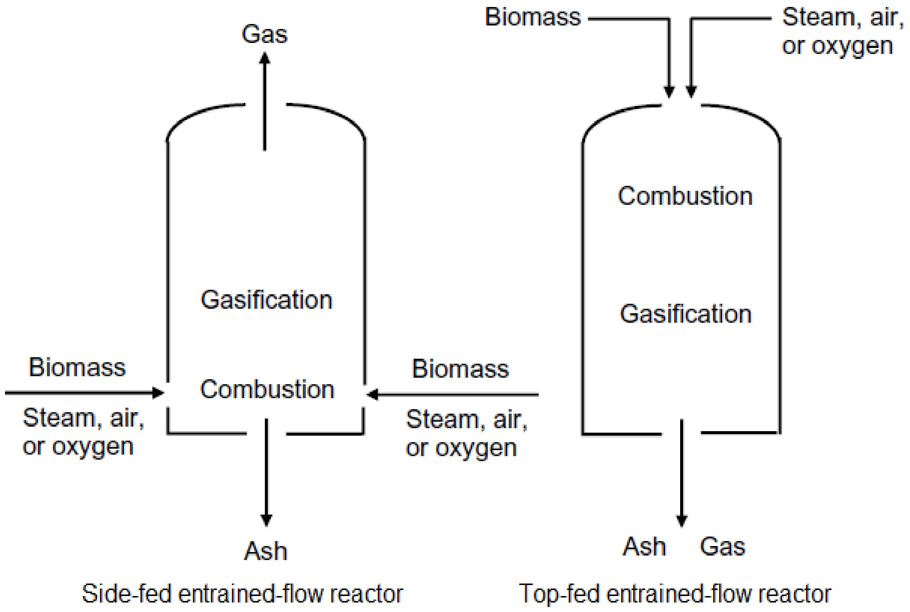

Figure 1-3 Two main types of EFR [18]

1.3 Second generation biofuel

Second generation biofuels usually refer to the liquid fuels produced from the non-food biomass, which is in contrast to first generation biofuels produced primarily from food crops such as cereals, sugar crops and oil seeds. As concluded in a report by the International Energy Agency [24], several concerns of the first generation biofuels have been raised, such as, contribution to higher food prices, limited greenhouse gas reduction benefits, a negative impact on biodiversity, and competing for scares water resources in some regions. Thus an increasing attention has been devoted to the development of production of second generation biofuels. The second generation biofuel are not widely commercially available yet, but a considerable number of pilot and demonstration plants have been announced or set up in recent years, with research activities taking place mainly in North America, Europe and a few emerging countries (e.g. Brazil, China, India and Thailand) [25]. The production of second generation biofuels especially from lignocellulosic feedstocks can be achieved through two very different processing routes [24,26]:

- Biochemical – in which enzymes and other micro-organisms are used to convert cellulose and hemicellulose components of the feedstock to sugars prior to their fermentation to produce ethanol;
- Thermochemical (also known as biomass-to-liquids, BTL) – where pyrolysis/gasification technologies produce a synthesis gas from which a wide range of long carbon chain biofuels, such as synthetic diesel, aviation fuel, or ethanol, can be reformed, based on the Fischer–Tropsch conversion as shown in the Figure 1-1.

The conversion of the lignin component in the biomass is one of the key differences between the above two paths. In biochemical enzymatic hydrolysis processes, lignin cannot be converted and is usually used for heat and power generation, whereas in the BTL process, lignin is used for producing syngas. Despite this difference, similar *overall* yield in energy and biomass to biofuel conversion efficiencies could be expected from the two processes, which are around 6.5 GJ/t and 35% respectively [27]. In addition, it seems that there is no clear commercial or technical advantage between the biochemical and thermochemical pathways. However, the final products from thermochemical routes are much more flexible compared to ethanol, the only produced chemical from biochemical routes.

1.4 Thesis objective

Biomass gasification is primarily characterized by devolatilization and subsequent char conversion. A good understanding of these two steps is essential for optimization of reactors applied for biomass gasification. However, analysis of biomass gasification is usually performed using thermogravimetric analyzers which are operated far from practical conditions. Quantitative studies of biomass devolatilization and char conversion under high temperatures and high heating rates were rarely reported and worth investing for an efficient gasification process in practical systems.

Furthermore, computational fluid dynamics (CFD) simulations as a relatively cheap, non-intrusive technique have gained its popularity recently. Taking account of fluid mechanics, heat and mass transfer, solid-fluid interaction, etc., the CFD simulation can provide detailed information of both the gas and the solid fuel inside a reactor which is usually difficult to measure directly from experiments. This powerful technique helps to comprehend more details of the conversion process of biomass and to evaluate different configurations of gasifiers.

The aims of this Ph.D. project are: 1) to carry out a series of experiments that unveil crucial characteristics of devolatilization and char conversion for a number of lignocellulosic biomass under high temperatures and high heating rates, and 2) to develop CFD models that allow for the prediction of biomass gasification in both FBRs and EFRs.

1.5 Thesis organization

Chapter 2 provides a literature review covering various aspects of biomass gasification related to this study, i.e. devolatilization of biomass, conversion of biomass-derived char, and CFD simulation of biomass gasification. An introduction of the experimental approach is given in Chapter 3 which contains the tested fuel and torrefaction process, the drop tube reactor (DTR) used for devolatilization and char conversion experiments, experimental procedures, analytical methods, and ash tracer technique for assessing conversion ratio of tested fuels. In Chapter 4, all three Eulerian–Lagrangian CFD models developed in this study are described, including the model for assisting experiments carried out in the DTR, the model for simulating entrained-flow biomass gasification, and the model for evaluating drag correlations and biomass gasification in the dense gas-solids fluidized beds. Results and discussions are concluded as summary of the selected papers in Chapter 5. Chapter 6 offers the comments and recommendations for the further work. Five selected papers are attached presenting on each specific subject. One additional publication is included in the Appendix at last. This represents related work, yet at more fundamental nature and hence exclude from further discussion. Papers I–V are to be considered the main contribution to this thesis.

Chapter 2

Literature Review

2.1 Devolatilization behavior and pyrolysis kinetics of biomass

Biomass often contains large percentage of volatile contents. Therefore, extensive understand of its devolatilization process is crucial for a more efficient biomass gasification processes [28]. Solid thermal degradation, as mentioned in the introduction, resulting in production of a variety of chemical compounds, are often lumped into three groups: permanent gases, a pyrolytic liquid (bio-oil/tar) and char [29] or simply into volatiles and char for engineering applications. The overall pyrolysis may consist of two separate steps, primary decomposition of solid fuel and secondary reactions of volatile condensable organic products into low-molecular weight gases and char [28]. The present work and corresponding review are mainly focused on the primary decomposition reaction.

Thermal gravimetric analysis (TGA) is one of the most commonly applied techniques for investigating thermal decomposition of solid fuel. Only very small amounts of the sample are usually required by the TGA in order to accurately record mass loss and temperature of the tested fuel. It was found that at kinetically controlled conditions, primary degradation of biomass initiated at around 500 K followed by rapid release of volatiles at about 573 K and the process finished at 700–750 K [28,30–32]. The primary decomposition of three main components of lignocellulosic biomass, including cellulose, hemicellulose, and lignin, can be identified from thermogravimetric curves under either isothermal or dynamic conditions. Decomposition of cellulose, hemicellulose, and lignin happens at 598–648 K, 498–598 K, and 523–773 K, respectively [30]. Due to the low availability of hemicellulose, Xylan has been studied as a replacement, which decomposes at 493–588 K [33–35]. Using thermogravimetric data, kinetic parameters of global or semi-global mechanisms can be conducted. However, difficulties exist in kinetic analysis in separating the effects of chemistry and transport phenomena [28]. Spatial gradients of temperature during the TGA have been extensively studied and may cause deviation for estimating the devolatilization kinetic [32,36–38]. Furthermore, traditional thermogravimetric analyzers can be only operated at relatively low heating rates, which differ a lot from most practical applications of thermal conversion of biomass. Heating rates of biomass influence behavior of biomass devolatilization and lead to different kinetic parameters [32,39,40]. Indeed, the applicability of kinetic parameters of biomass devolatilization obtained by the TGA in various heating rates has been discussed by Mehrabian *et al.* [41]. It was suggested that the pyrolysis of wood dust and wood pellets occurs always in high heating rate regimes in the state-of-the-art combustion/gasification plants. Thus the kinetic parameters obtained by low heating rate TGA systems (heating rates lower than 50 K/min) are not applicable. However, those parameters may be used for wood logs which usually undergo pyrolysis process at low heating rate during practical conditions.

An alternative way to mimic such conditions is to use a DTR or an EFR. However, important information about the fuel particle such as residence time and temperature is difficult to be measured directly in a DTR or an EFR. A lack of knowledge of the detailed thermal history of fuel particles makes precise determination of devolatilization kinetics challenging. Li *et al.* studied rapid devolatilization of raw and torrefied palm kernel shell in a DTR operating between 773 K and 1473 K [42]. It was found that the devolatilization rate of palm kernel shell decreased as a result of torrefaction. In addition, torrefied biomass displayed higher activation energies of devolatilization reactions. Xiu *et al.* investigated the devolatilization characteristics of several biomass materials using a plasma-heated laminar EFR operating between 750 K and 900 K [43]. Conversion of biomass fuel particles was determined by the ash tracer method and a single first-order reaction (SFOR) model was used to investigate the devolatilization process. For the studies briefly reviewed above, particle temperatures were assumed constant during the devolatilization process, and equal to the reactor wall temperature. In addition, residence time was assumed to be the same for all fuel particles fed into a reactor and was calculated based on the velocity of the particle entrainment gas. These assumptions may lead to considerable errors when deriving biomass devolatilization kinetics.

Different models have been developed to estimate the biomass devolatilization rate, based on calculated particle residence times and/or particle temperatures in a DTR. Tolvanen *et al.* studied the mass loss behavior of several types of solid fuels, including peat and torrefied wood, in a DTR over a temperature range of 973 K to 1173 K [44]. Devolatilization kinetic parameters were obtained using an SFOR model and a two-competing step model. In addition, the predicted evolution of fuel particle diameters was compared against the measured values. Lu *et al.* investigated the effects of particle shape and size on biomass devolatilization at 1600 K [45]. The intraparticle temperature distribution was calculated by discretizing the particle into a one-dimensional domain, with wall temperature and gas temperature as inputs. A similar model that considered intraparticle heat and mass transfer was used by Dupont *et al.*, who predicted the main product yields of woody biomass devolatilization [46]. In addition, Bharadwaj *et al.* found that intraparticle mass transfer was crucial for predicting devolatilization of millimeter-sized biomass [47]. However, several parameters, such as gas temperature, gas velocity and particle velocity, are needed as raw data for kinetic evaluation via the models, which can be obtained by either experiments or empirical equations. Therefore the applicability of these types of particle models is restricted.

Several studies have investigated devolatilization of biomass in DTRs with CFD assistant analysis. Sun *et al.* examined flash pyrolysis of rice husk and sawdust over 973-1273 K via Ansys Fluent CFD software [48]. An SFOR was used to describe the thermal decomposition of biomass. The overall gas yield predicted by the CFD model agreed well (deviations less than 7%) with measured values. However, large errors existed between predicted and measured values of the gas yield of individual components. Simone *et al.* systematically evaluated the biomass devolatilization kinetics over 673 -1073 K with CFD-aided experiments [49]. The Ansys CFX CFD software was used in this study, with an Eulerian/Lagrangian approach. A sub-routine was used to search optimal kinetic parameters of an SFOR model for biomass devolatilization. Some important observations were noted, such as the importance of the particle size distribution, the limited utility of complicated swelling or shrinking models, and that the SFOR model is insufficient for predictions of biomass devolatilization over an extended temperature range. Papadikis *et al.* investigated the fast pyrolysis of a single large biomass particle (diameter of 5 cm) using a two-stage semi-global model [50]. A modified particle model considering the temperature gradient inside the particle was implemented as a user defined function (UDF) in Ansys Fluent. They concluded that the temperature gradient inside the particle is important to the biomass degradation rate. However, the CFD simulation was computationally intensive because of the detailed particle model.

2.2 Conversion behavior of biomass char

Char conversion is a slow process compared to thermal decomposition of biomass and gas-phase reactions of volatile products. Therefore it is usually considered to be the rate-limiting step of the entire thermochemical conversion process.[51] A comprehensive review of the conversion behavior and reactivity of lignocellulosic biomass char has been given by Di Blasi [52]. The influence of several factors, such as heating rate, temperature, and external pressure, on char reactivity was thoroughly reviewed and discussed. The thermal histories experienced by fuel particles during pyrolysis have a strong effect on char reactivity. As fuel particles are heated to a high temperature at a high heating rate, volatiles are rapidly released in connection with the destruction of the original cell wall structure. Therefore high temperatures and high heating rates promote the formation of char particles with a macroporous structure that facilitates reactant penetration and therefore char reactivity [53–57]. However, because of thermal annealing, the concentration of active sites on the char decreases with prolonged retention time at high temperatures, decreasing char reactivity [53,58]. At low heating rates, the natural microporosity of the fuel particles is better preserved [59]. Yet it is believed that microporosity contributes less to char reactivity at high temperatures than a macroporous structure created at high heating rates [54]. In general, char reactivity is reduced for devolatilization at elevated external pressures. High external pressures impede volatile release and cause deposition of secondary char fragments and reduction of active sites [55,56]. Moreover, the negative effect of external pressure on char reactivity may be partly attributed to the formation of graphitic structures in chars produced at high external pressures [55,60].

In the recent years, increased efforts have been given to investigate the characteristics and reactivity of biomass char produced at high temperature and high heating rate conditions that are relevant to industrial reactors. DTRs or EFRs are often used for achieving such intense conditions for thermal conversion of biomass char. The conversion behavior of high heating rate biomass char produced from DTR or EFR under different combustion and/or gasification conditions has been previously studied and reported.

Matsumoto *et al.* examined the gasification kinetics of Japanese cedar char, Japanese cedar bark char, and a mixture of hardwood char and Japanese lawn grass char, each of which was obtained from an entrained-flow gasifier with steam and oxygen at 1173–1273 K [61]. They suggested that the order of CO_2 and H_2O reactivities was positively correlated to the content of alkali metals ($K_2O + Na_2O$) and the oxygen to carbon ratio in biomass char. Silimar findings were also reporeted by Mermoud *et al.* [62] who concluded that the initial apparent reactivities of the charcoals are proportional to the initial ash content of the charcoals. Fermoso *et al.* studied the high-pressure CO_2 gasification reactivity of slash pine char obtained at 1273 K and 1673 K [63]. An increase in total pressure of the gasification system led to a decrease in the reaction rate, whereas the reaction rate was observed to increase proportionally to the increase in the partial pressure of CO_2. The mixed CO_2 and H_2O gasification of high heating rate beech wood char was also investigated by Guizani *et al.* [64]. It was observed that increasing the CO_2 concentration from 0% to 30% in a 10% steam-containing atmosphere resulted in a 2.7-times-higher char reactivity. They demostrated the validatity of an additive law reflecting a passive cooperation of steam and carbon dioxide in the gasification reaction.

The effect of devolatilization atmosphere (CO_2 vs. N_2) on the characterization and oxidation reactivity of char produced from rice husk, forest residuals and wood chips at a temperature of 1223 K was investigated by Borrego *et al.* [65]. It was found that char yield under CO_2 was slightly higher than that under N_2 for all three biomass. A higher apparent reactivity was observed for all biomass chars produced under N_2 than under CO_2. Moreover, an inverse relationship between the weight loss in the DTF and the intrinsic reactivity was revealed. Similar studies were also conducted by Guizani *et al.* [66]. However, they found that char yield from wood-chips was lower under 20% CO_2 in N_2 than that under pure N_2, which indicated that either less char was formed, or that char was consumed. In addition, the reactivity of the char produced in N_2 towards H_2O, CO_2 and O_2 was slightly lower that that char produced in mixed atmosphere.

Reactivities of coal chars and a biomass char prepared in primary N_2 atmosphere (with around 0.5 % O_2 to prevent tar condensation on the car particles) at 1473–1673 K were compared by Karlström *et al.* [67]. The result revealed that the tested biomass char, with an apparent reaction order of 0.78, had higher oxidation reactivity than the coal char. Kajitani *et al.* [68] investigated co-gasification reactivity of coal char and woody biomass char produced at 1673 K. They found that CO_2 gasification reactivity of the mixtures of coal char and biomass char was almost the same as that of single coal char at the high temperature gasification, whereas, slightly improvement of reactivity was found in low temperature cases because of the catalysis of alkaline and alkaline-earth metal species in the biomass char.

Due to the difficulties for accessing particle information inside DTR, few CFD assistant char reactivity experiments were also reported. Meesri *et al.* performed both experimental studies and CFD simulations of combustion behavior of sawdust char produced at 1673 K [69]. The CFD simulation have yielded reasonably results compared to the experimental data of char burnout. However, some inconsistencies were observed to predict the near-extinction burnout characteristic of the sawdust char due to the reactivity-independent approach of the model.

Publications regarding the effects of torrefaction on the conversion behavior of high heating rate char are scarce. As reported by Jones *et al.* [70] and Fisher *et al.* [71] devolatilization of raw willow and torrefied willow was carried out in a pyroprobe at 1273 K with a heating rate around 1000 K/s and in a DTR at 1173 K with a heating rate over 500 K/s, respectively. The reactivity of the resultant char samples was further investigated using a TGA. It was found that char produced from torrefied willow has a lower reactivity than char produced from raw willow. In addition, torrefaction was reported to have a significant impact on the reactivity of char samples produced at a high heating rate [71]. However, to the best of the author's knowledge, the effect of torrefaction on the reactivity of forest residue char produced at high heating rate conditions has not been previously studied.

2.3 CFD simulation of biomass gasification

2.3.1 CFD Simulation of biomass gasification in the fluidized bed reactor

CFD Modelling of a gas-solid FBR can be generally categorized into Eulerian–Eulerian or Eulerian–Lagrangian approaches. For Eulerian–Eulerian approach, both particle and fluid phases are treated as interpenetrating continua with appropriate interaction terms representing the coupling between the phases. This approach can capture the macroscopic characteristics of the FBR and has been developed for many years due to the relatively low computational cost [72–74]. However, the Eulerian–Eulerian approach does not recognize the discrete character of the particle phase. In addition, when the Eulerian–Eulerian approach applies to the poly-disperse fluid-particle systems, which are characterized by a continuous distribution of the particle properties, such as size or velocity, moment transport equations are mathematically unclosed. On the other hand, for the Eulerian–Lagrangian approach, the fluid phase is modelled as a continuum by solving the Navier–Stokes equations, whereas for the dispersed phase individual particles are tracked in space and time by directly integrating the equations of motion. It can also offer detailed microscopic information at the particle level, such as particle trajectory, particle-particle and particle-fluid interaction, and transient forces acting on each particle, which is extremely difficult, even impossible to obtain by the Eulerian–Eulerian approach. When the particle phase is solved by the discrete element method (DEM), the Eulerian–Lagrangian approach is also called CFD–DEM model. For the explicit consideration of particulate interactions, two methods are widely used in the CFD–DEM: the hard sphere model [75] and the soft sphere model [76]. For dense particle systems with multiple contacts between particles the soft-sphere collision model is usually applied. The use of CFD–DEM for fluidized bed modeling was pioneered by Tsuji *et al.* [77] and since then, thanks to the dramatic increase in computational capacity, the CFD–DEM has gained its popularity among engineers and researchers.

For multiphase simulations, a key consideration is the coupling between the phases. From a physical point of view, the coupling currently comprises the effect of (a) volume displacement by the particles, and (b) fluid-solid interaction forces exerted on the particles. These non-linear fluid-solid interaction forces or called generalized drag forces are believed to play a very important role in the formation of heterogeneous flow structures in dense gas-fluidized beds [78]. There are various drag correlations available in the literature. The Gidaspow correlation [79] is a combination of the Ergun equation [80] for the dense granular regime (gas volume fraction less than 0.8) and the Wen and Yu equation [81] for dilute granular regime (gas volume fraction lager than 0.8). This model is often used in the literature, but the transition between the two regimes is discontinuous, which may lead to convergence problems [82]. Di Felice using an empirical fit to a wide range of fixed and suspended-particle systems covering the full practical range of flow regimes and porosities, proposed a continuous single-function correlation for the drag force [83]. More recently, Hill *et al.* proposed a Hill–Koch–Ladd (HKL) correlation applicable to different ranges of Reynolds numbers and solid volume fractions based on the data from Lattice–Boltzmann simulations [84,85]. Later Benyahia *et al.* blended the HKL correlation with known limiting forms of the gas-solids drag function and constructed an extended HKL drag correlation (EHKL) which is applicable to the full range of solid volume fractions and Reynolds numbers [86]. Although some works have investigated the effects of different drag models within the Eulerian–Eulerian framework [87–89], few are reported for Eulerian–Lagrangian approaches [78].

The CFD–DEM is computational expensive due to monitoring particle collisions. Therefore, modeling of reactive dense gas-solid mixtures in FBRs using CFD–DEM is challenging. To date, most of the CFD–DEM studies have been focused on the hydrodynamics of the isothermal fluidized bed and there have been few works on the simulation of dense gas-solid flow coupling with chemical reactions. Liu *et al.* used a

CFD–DEM model to study char and propane combustion in a FBR [90]. Their simulation conditions were strongly simplified, e.g., only 300 char particles were added at the start of simulation and there was no more fuel injection at later times. Bruchmüller *et al.* carried out a biomass fast pyrolysis simulation in a bubbling fluidized bed but did not take turbulence into account [91]. Gerber and Oevermann used a 2D CFD–DEM model to simulate wood gasification in a FBR but they used only charcoal as the bed material without any inert bed material such as sand used in ordinary experimental beds [92].

2.3.2 CFD Simulation of biomass gasification in the entrained-flow reactor

The concentration of fuel particles is much lower in the EFR than in the FBR during the gasification process and thus particle-particle collisions could be ignored. This dramatically reduces computational cost of the Eulerian–Lagrangian simulation and makes this approach especially attractive for the solid fuel gasification in the EFR.

Due to the challenge related to the required high grindability of the fuel and problems with slagging, relevant experimental data of biomass gasification in EFRs have been rarely reported. Therefore, also CFD simulations of biomass gasification in an EFR are scarce. Fletcher *et al.* investigated biomass gasification in an EFR using CFX4 [93,94]. The CFD simulation provided detailed information on the flow characteristics, gas composition and temperature distribution. However, because of the computational limitations at that time, only a crude devolatilization model, a global gas phase reaction mechanism and the Eddy break-up (EBU) combustion model were implemented, which resulted in a high discrepancy on gas composition estimations compared with experimental results. Recently, Chen *et al.* performed a comparison study of gasification phenomena among biomass, torrefied biomass and coal in an EFR using the ANSYS Fluent V12 [95]. It was found that the cold gas efficiency of raw biomass was dramatically improved by torrefaction. However, the CFD model has only been validated in their previous study by experimental data of coal gasification [96].

Compared to rarely reported CFD simulations of biomass gasification in EFRs, a variety of sub-models have been developed and applied for CFD simulation of coal gasification.

The performance of Reynolds-averaged Navier–Stokes (RANS) turbulence models were examined by Kumar and Ghoniem [97,98]. They concluded that the SST k−ω model performed best among the tested RANS models for both a non-reacting sudden expansion case and a pilot scale gasifier. A advanced large eddy simulation (LES) has been performed by Abani and Ghoniem who found that the radial distribution of species were improved by the LES and unsteady flow structures of various sizes throughout the gasifier domain were captured [99]. Vascellari *et al.* proposed an iterative procedure for an accurate modeling of the pyrolysis process [100]. The optimal kinetic parameters for the empirical models could be obtained from detailed pyrolysis models such as CPD [101,102], FLASHCHAIN [103] or FG–DVC [104]. Various char consumption models have been studied and implemented into CFD simulations [98,105–108], including the moving flame front model [109,110] , the simplified Single Nth Order Reaction model [111], the shrinking core model [112], and the char consumption models for C-CO reaction [113], C-H_2O reaction [114], and C-O_2 reaction [115] in the kinetics-controlled regime. Gas phase reactions, especially the water-gas shift reaction, are important in the gasification process. Most of the reaction rates for the water-gas shift reaction were obtained with specific catalysts or with the pressure much higher than typical gasification conditions. The evaluation and calibration of three sets of water-gas shift reaction rates were performed by Lu and Wang [116,117]. The original published rates [118–120] were found unsuitable for simulating water quench of the tested gasifier. The calibrated global reaction rates were also proposed. Investigation of radiation models in the entrained-flow coal gasification has also been carried out by Lu and Wang [121]. Five different radiation models were tested and compared including the Discrete Transfer Radiation Model, the P-1 Radiation Model, the Rosseland Radiation Model, the Surface-to-Surface Radiation Model, and the Discrete Ordinates Radiation Model. The result reveals that predicted syngas composition was heavily influenced by the radiation model. The P-1 method was found to behave stably and robustly in predicting the syngas temperature and composition. Other aspects of the gasification process such as slagging behavior have also been thoroughly studied by Yong and Ghoniem [122], Chen and Ghoniem [123], Gibson *et al.* [124], and Ambrosino *et al.* [125] using CFD simulation, but will not be discussed further here.

Chapter 3

Experimental Approach

Experiments of rapid devolatilization and char reactivity were conducted in order to investigate the thermochemical conversion of biomass and to provide important input for modelling. Description of fuel and pretreatment, reactor, experimental procedures, analytical methods, and ash tracer technique are briefed in this chapter.

3.1 Fuel and pretreatment

Two types of lignocellulosic biomass and corresponding torrefied biomass were tested: Norwegian spruce (NS), forest residue (FR), torrefied Norwegian spruce (TNS), and torrefied forest residue (TFR). NS is a relatively clean and pure biomass compared to FR which is a mixture of tops and branches (including needles). Both NS and FR were ground and compressed to 6 mm pellets without additional binders. TNS and TFR were produced in a torrefaction reactor consisting of four electrically heated horizontal screw conveyors and one water-cooled horizontal screw conveyor positioned on top of one another. The pellets fed from the top of the reactor were initially heated at 498 K for 5 min, torrefied at 548 K for 30 minutes, and then cooled to room temperature before being discharged from the reactor. The reactor was purged with N_2 to ensure inert conditions during operation. The details of the torrefaction process have been presented elsewhere [126]. All tested biomass was ground using a Thomas Model 4 Wiley Mill and then sieved to the size range of 212 to 300 μm. Figure 3-1 shows appearances of all types of pellet and sieved fuel particles used in the experiments. The properties of fuel are listed in Table 1.

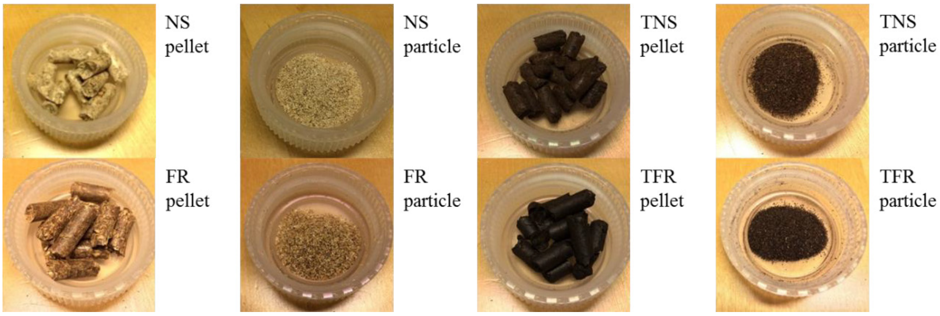

Figure 3-1 Fuel samples used in the experiments

Table 1 Properties of biomass fuel

		FR	TFR	NS	TNS
Proximate analysis (as received, wt%)	Moisture	6.3	4.2	5.0	3.8
	Volatiles	70.0	61.6	77.1	72.3
	Fixed carbon	21.5	31.5	17.5	23.4
	Ash	2.2	2.7	0.4	0.5
	Volatiles (dry, ash-free)	76.5	66.2	81.5	75.6
Ultimate analysis (daf, wt%)	C	52.1	59.5	46.7	52.8
	H	6.1	5.6	6.2	5.8
	N	0.5	0.6	0.1	0.1
	S	< 0.02	< 0.02	< 0.02	< 0.02
	O (diff)	41.3	34.3	47.0	41.3
Ash measured by TGA (dry basis, wt%)		2.0	2.9	0.4	0.4

3.2 Drop tube reactor

Both rapid devolatilization and char reactivity experiments were carried out in an electrically heated DTR (Figure 3-2 Schematic sketch of the DTR at Sandia National Laboratories), located at the Combustion Research Facility of Sandia National Laboratories, Livermore, California. The DTR features a 1.5 m long vertical reactor section with a diameter of 5.08 cm and a 1.0 m long horizontal gas preheater section. Its operation range spans temperatures up to 1650 K and pressures up to 20 atm. Particle and gas samples for further analysis can be collected at different positions along the vertical reactor section. The particulate fuel samples are continuously fed into the reactor by a custom-made particle feeder located on top of the DTR. The feeding rate is determined by the rate of displacement of the fuel-containing test tube and is therefore a volumetric rate (differences in bulk density thus result in different mass feeding rates). Fuel particles similar in size will thus enter the reactor in roughly the same number per unit time, if the rate of displacement is the same.

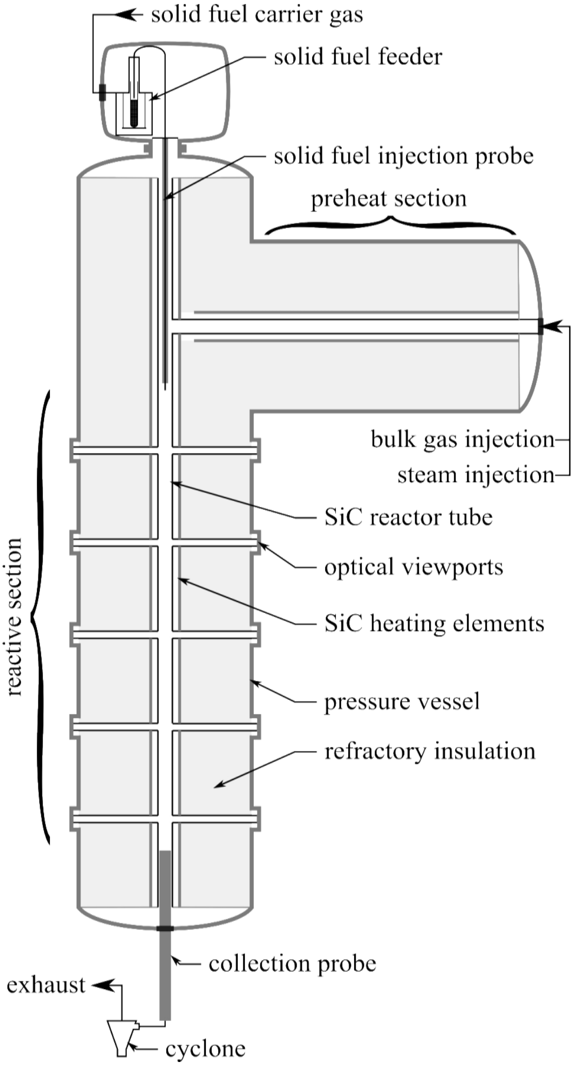

Figure 3-2 Schematic sketch of the DTR at Sandia National Laboratories

3.3 Experimental procedures

3.3.1 *Rapid devolatilization/char production experiments*

The sieved fuel particles were supplied by the feeding system at an approximate mass flow rate of 50 g/h. A 4 Standard Liter per Minute (slpm) room temperature N_2 carrier gas transported fuel particles into the DTR through a water-cooled tube. A 182 slpm of N_2 was injected into the horizontal gas preheat section regulated by a mass flow controller, where it was heated to the desired reaction temperature (either 1073 K or 1473 K). After the heated N_2 stream entered the reactor tube, it first passed a honeycomb straightener and then mixed with the cold particle-laden carrier flow. The particles passed through the reactor and were subjected to devolatilization. Char residue was produced and extracted at various heights of the reactive section by a water-cooled sampling probe. An addition 40 slpm of cool N_2 flow was injected at the tip of the probe to ensure quenching of char. The resulting char particles were eventually collected using a cyclone separator which was connected to the sampling probe. Specifically, char used in reactivity experiments was produced at 1473 K and sampled where distance between the tip of the feeding tube and the quench gas inlet in the sampling tube was 101 cm.

3.3.2 *Char gasification and oxidization experiments*

The conversion of char under gasification and oxidation conditions was also carried out in the DTR system. In the gasification experiments 50 slpm of pure CO_2 was injected into the gas preheater. A slightly higher reactor temperature (1573 K) was used, on account of the expected low reaction rate of CO_2 with the char. The DTR was purged with pure CO_2 for at least 5 min prior to each experiment. The char oxidation experiments were carried out with a similar procedure, but with the reactor operating at 1473 K. However, considering the high oxidation rate of the biomass char at such a temperature, a mixture of 2.0% O_2 in N_2 was chosen (180 slpm N_2 and 3.6 slpm O_2) to avoid complete char burnout and facilitate the assessment of reactivity differences of the two fuel types. Residual char samples were collected at three different heights in the DTR for further characterization and reactivity study. The feeding rate of FR char and TFR char was approximately 40 g/h using a 4 slpm N_2 carrier flow.

3.4 Analytical methods

The microscopic structures of parent fuel particles, char particles, and residues collected from the char gasification and oxidization experiments were characterized using a scanning electron microscope (SEM, HITACHI S-3400). Elementary analysis was carried out using an element analyzer (EA-1008 CHNS-O). According to ASTM standard, the oxygen content was calculated by difference after determining the content of C, H, N and S. Average values of the elemental composition of each sample were calculated from at least three duplicate analyses. The ash contents of parent fuel particles and corresponding char samples were determined using a thermogravimetric analyzer (TA Instrument SDT Q600). Approximately 10 mg of sample was oxidized in air at 823 K until the weight of the residues is stable. A similar method has been applied in another study [67]. For each sample, at least three duplications of ash content determination were performed to get more reproducible results. The content of ash forming elements in the samples was analyzed by inductively coupled plasma mass spectrometry (ICP–MS) and inductively coupled plasma optical emission spectrometry (ICP–OES). The diameter distributions of the parent fuel particles and char particles were measured using a laser diffraction analysis (Beckman Coulter LS230).

3.5 Ash tracer technique

The extent of fuel conversion can be calculated from the changes in the content of non-volatile tracer elements and organic elements from the original fuel to the partly reacted sample. Specifically, the conversion ratio of carbon, X_{carbon}, is defined as

$$X_{carbon} = 1 - \left(\frac{Tr_0}{Tr} \times \frac{Q_{carbon}}{Q_{carbon,0}} \right) \tag{3-1}$$

where $Q_{carbon,0}$ and Q_{carbon} represent the mass fraction of carbon in the char before and after char conversion, respectively. Tr_0 and Tr are the contents of the selected tracer element in the char before and after char conversion. For a reliable tracer element, it should not volatilize over the investigated experimental conditions and should also be present at such a quantity in the raw fuel that it can be readily measured with small uncertainty. In a number of studies, the total ash content has been used as a tracer for assessing fuel conversion [61,67,68,127–130]. However, decomposition and vaporization of some inorganic mineral compounds [131,132] may yield biased estimates of ash content and consequently of fuel conversion. Based on thermodynamic equilibrium calculations, titanium, silicon, calcium, manganese, barium, and magnesium, all present in wood, are stable at temperatures as high as 1573 K [133]. In addition, experimental studies have shown that calcium, manganese, and magnesium only slightly volatilize up to 1673 K [134,135]. Due to their relatively refractory nature, titanium [136–140], silicon [138,139,141], aluminum [138–140], calcium [140], magnesium [140], and iron [140] have been previously used as tracers to evaluate weight loss of fuel at high temperature. Calcium, Manganese, barium, and magnesium are used in Paper II as fuel tracers, whereas Manganese, barium, and magnesium are used in Paper I. Titanium is not selected because of the low concentration in our fuel samples. Silicon is also not considered, to avoid potential interferences from entrained particles from the reactor's thermal insulation.

Chapter 4

Modeling Approach

Several CFD models have been developed for devolatilization and gasification of biomass. The Eulerian–Lagrangian approach was selected to both diluted (in a DTR and an EFR) and dense (in a FBR) particle systems. The modeling approach is briefly introduced in this chapter.

4.1 Modeling of the drop tube reactor

A CFD model was developed using the Ansys Fluent 14.0 to simulate the rapid devolatilization of biomass in the DTR showed in Figure 3-2. The three-dimensional computational domain of the DTR was discretized with a hexahedral mesh (338084 cells in total), shown in Figure 4-1. The wall temperature and inlet conditions were set to match the corresponding experimental conditions. Radiation was taken into account using the discrete ordinates model which spans the entire range of optical thicknesses. The species transport equations were solved for both N_2 and volatiles released from the biomass. The standard k-ω model was chosen to match the measured gas temperature profiles in the DTR at various bulk gas flow rates. The temperature profiles were measured by thermocouples placed in the flow at 5 equally spaced vertical positions along the reactive section of the DTR. Gas phase reactions were not considered due to the N_2 dominated inert environment.

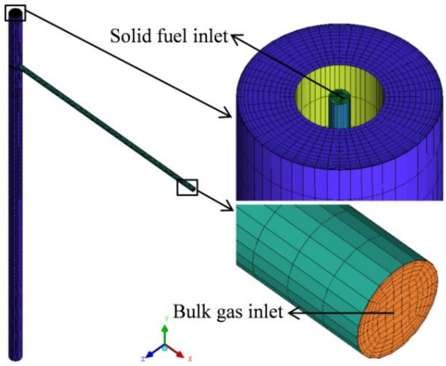

Figure 4-1 Three-dimensional computational domain of the DTR

The simulated biomass particles were assumed to be spherical and were tracked using a Lagrangian approach. Every 5 ms, biomass particles with diameters following a Rosin-Rammler distribution (10 discrete diameters) were injected through the inlet at the top of the reactor. A modified two-competing rate devolatilization model was developed and used in the CFD simulation, which can be described below:

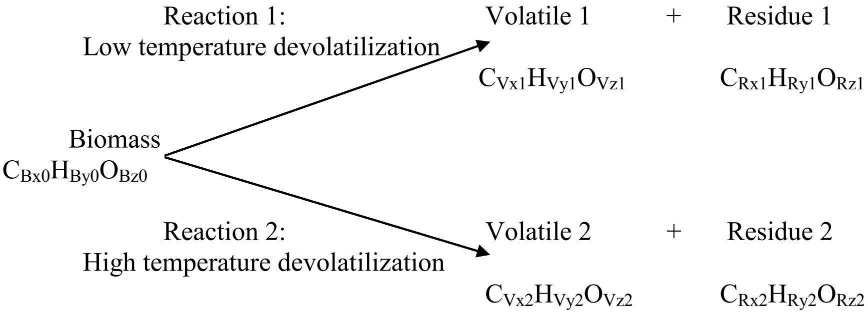

(4-1)

This model is applicable over a broad range of temperatures and has capacity to estimate transformation of organic elements in biomass char. The model is an extension from previously published two-competing rate devolatilization model and is further discussed in Paper I. During devolatilization, the biomass particle diameter was assumed to stay constant, whereas the particle density was updated according to mass loss. At each corresponding experimental collection position, information on every individual particle, such as its mass, temperature, residence time and location, was recorded in the CFD simulation over a computational duration of 2.5 s (over 5×10^5 particles in total). More detailed information related to the mathematical equations can be found from the ANSYS Fluent Theory Guide [142].

4.2 Modeling of the entrained-flow reactor

A CFD model was formulated using an open source code, OpenFOAM, to investigate entrained-flow gasification. The model was set up according to experiments performed by Qin *et al.* [143] in a high-temperature (1273-1673 K) laboratory-scale EFR, which provides abundant data at various conditions and sufficient detail of experimental setup. Figure 4-2 shows the schematic of the entrained-flow reactor [143], which operates at atmospheric pressure, with a length of 202 cm and a diameter of 8 cm. A three-dimensional structured grid consisting of 281280 cells was employed as shown in Figure 4-3.

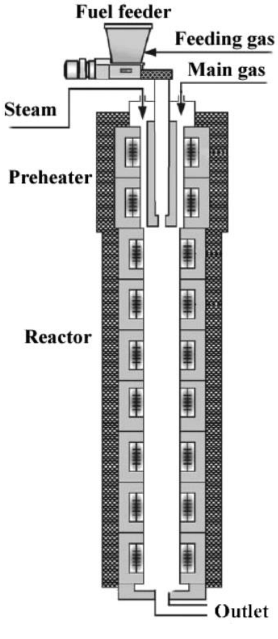

Figure 4-2 Schematic of experimental setup

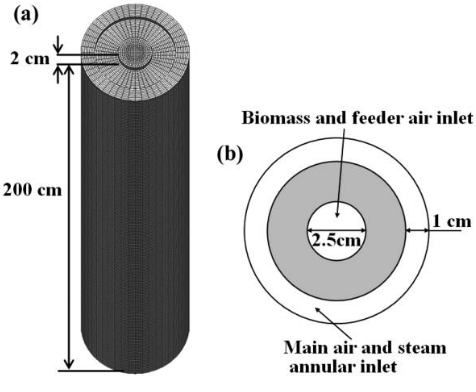

Figure 4-3 (a) Three-dimensional (3D) computational mesh for the DTU laboratory-scale entrained-flow reactor and (b) the top view of the reactor inlet

Transport equations were solved for the continuous gas phase. The *k*-*ε* model was employed in order to resolve the turbulence induced by large temperature gradients and a large amount of gas products from biomass by devolatilization and gasification. Simple global reactions were used to describe the gas-phase chemistry and the effect of turbulence on combustion and gasification was resolved by the partially stirred reactor (PaSR) model [99]. Considered gas phase reactions are listed below:

$$\begin{aligned}
&\mathrm{CH_4 + 2O_2 \rightarrow CO_2 + 2H_2O}\\
&\mathrm{CH_4 + HO_2 \rightarrow CO + 3H_2}\\
&\mathrm{H_2 + 0.5O_2 \rightarrow H_2O}\\
&\mathrm{CO + 0.5O_2 \rightarrow CO_2}\\
&\mathrm{CO + H_2O \leftrightarrow CO_2 + H_2}
\end{aligned} \tag{4-2}$$

The trajectories of discrete particles were tracked in a Lagrangian manner. It was assumed that the fuel particles, which consist of a mixture of volatile matter, char, and ash, can be represented as spherical particles with a prescribed size distribution. The pyrolysis compositions released from the fuel can be expressed by the following Equation 4-3 and each product yield was solved with the help of the elemental conservation relationships.

$$\begin{aligned}
\mathrm{Biomass} \rightarrow\ &\alpha_1\mathrm{CO} + \alpha_2\mathrm{H_2O} + \alpha_3\mathrm{CO_2} + \alpha_4\mathrm{H_2} + \alpha_5\mathrm{CH_4}\\
&+\alpha_6\mathrm{char(s)} + \alpha_7\mathrm{ash(s)} \qquad \sum_i \alpha_i = 1
\end{aligned} \tag{4-3}$$

Consistent with Abani and Ghoniem's work [99], the devolatilization rate was modeled using an SFOR Arrhenius reaction. After devolatilization, the fuel particle was left with char and ash. The ash was assumed to be carried along with the particle, exiting the reactor without taking part in any reactions. Char will react in the presence of oxygen, carbon dioxide, and steam and gets converted to carbon monoxide and hydrogen. The following heterogeneous reactions were assumed and implemented in OpenFOAM:

$$\begin{aligned}
&C + 0.5O_2 \rightarrow CO \\
&C + CO_2 \rightarrow 2CO \\
&C + H_2O \rightarrow CO + H_2
\end{aligned} \tag{4-4}$$

The char consumption rate was determined by both bulk diffusion and chemical reaction rates. More detailed information related to the mathematical equations can be found in the attached Paper III.

4.3 Modeling of the fluidized-bed reactor

4.3.1 The non-reacting case

The CFD–DEM model was developed using OpenFOAM. The continuum gas phase hydrodynamics were calculated from the continuity and volume-averaged Navier–Stokes equations which were coupled with those of the particle phase through the porosity and the inter-phase momentum exchange [144]. For discrete phase particles, both translational and rotational motions were considered. Trajectories of individual particle were determined by three types of forces: gravitational force, fluid-particle drag force, and force due to inter-particle or particle-wall contacts. Fluid-particle drag force included both viscous drag force and pressure gradient force. Three well-known inter-phase drag force correlations (Gidaspow model [79], Di Felice model [83], and EHKL model [86]), were evaluated, accordingly. The soft sphere model was implemented taking account for particle collision.

The simulated fluidized bed geometry as shown schematically in Figure 4-4 was similar to those well-known studies by Tsuji *et al.* [77], and Xu and Yu [145] for comparative reasons. It consisted of a rectangular container of dimension 0.15m (width) × 0.9 m (height) × 0.004 m (thickness) with a jet orifice of 0.01 m in width at the center of the bottom wall. The left, right, bottom walls, the bottom orifice and the top exit consisted of the whole calculation domain boundaries. The fluidization solid particles were a group of 2400 spherical particles with a diameter of 4 mm which were also taken from Tsuji *et al.* [77], and Xu and Yu [145]. Note that the thickness of the bed was set equal to the particle diameter (one layer of particles) for simplicity. Air at a temperature of 293 K and standard atmospheric pressure was used as the fluidizing agent and introduced from the bottom orifice with a uniform velocity. The semi-three-dimensional domain consisted of 675 (15×45×1) hexahedral meshes. More detailed information related to the mathematical equations can be found in the attached Paper IV.

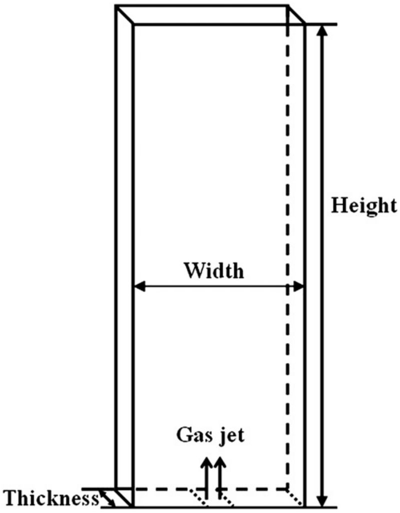

Figure 4-4 Geometry of the FBR

4.3.2 *The reacting case*

The CFD–DEM model was formulated based on the non-reacting model as in Paper IV and enlarged to account for the dense and reacting flows including models for turbulence, heat and mass transfer, radiation, particle shrinkage, pyrolysis, and heterogeneous and homogeneous reactions.

The gas phase was modeled as a continuum, known as an Eulerian type model. The modified k-ε turbulence model was implemented with consideration of volume fraction of gas, which is suitable for the dense gas-particle simulation system. For the sake of simplification, two global reactions (steam reforming of methane and water-gas shift) were used to describe the major conversion rates in the reactor and the effect of turbulence on reactions was resolved by the PaSR model [99].

The discrete particle phase consisted of sand and biomass particles were modeled in a Lagrangian manner. Sand played only the role of heat carrier in the biomass gasification without taking part in any reactions, whereas biomass underwent successive physical and chemical processes. The motion of both types of particles was calculated in a similar manner as the non-reacting simulation in Paper IV. Pyrolysis and char conversion were modeled based on Equation 4-2 and Equation 4-3. Due to the absence of oxygen, char oxidation reaction was not considered in this study.

The reactive CFD-DEM simulation is computational expensive, therefore the present study was configured according to the experimental study of Song *et al.* [146] in which a relatively small size of FBR was used. A semi-three-dimensional domain (0.23 m × 1.5 m × 0.0015 m) as shown in Figure 4-4 was discretized by 1725 hexahedral meshes. Initially, the reactor was filled completely with N_2 and a packed sand bed which was composed of 40,000 spherical sand particles with a diameter of 1.5mm.The initial temperature of the sand and the gas in the domain was set equal to the operating reactor temperature. At the bottom inlet, mass flow rates for gas and biomass were specified, respectively. At the walls, no-slip conditions were applied for the gas phase and the wall temperature was specified according to the operating reactor temperature. At the top outlet, the atmospheric pressure boundary condition was adopted and particles were allowed to exit the computational domain during the simulation, modeling a fine solids entrainment phenomenon. In the simulations, biomass was fed through the bottom orifice, together with a mixture of steam and nitrogen which was used as the gasifying agent as well as the fluidizing gas. The initial diameter of biomass particle was 1.5 mm which was taken from the experiment. Note that in order to study the effect of injection position on biomass gasification, biomass particles were injected at various positions. More detailed information related to the mathematical equations can be found in the attached Paper V.

Chapter 5

Summary of Selected Papers

5.1 Paper I Experimental and modeling study of the effect of torrefaction on the rapid devolatilization of biomass

In this paper, a combined experimental and a CFD approach has been conducted to study the rapid devolatilization of biomass and to access the effect of torrefaction. The rapid devolatilization of raw and torrefied biomass has been carried out in a DTR under high heating rate conditions. Characterization of the parent fuel and solid residues collected after DTR experiments has been performed to evaluate the extent of fuel conversion and morphological variations in different operation conditions. The SEM and size analysis revealed significant morphological changes (fragmentation and melting) and size reduction of char residues. Torrefaction affects the morphology and size distribution of char particles produced in the devolatilization process. Despite generally smaller fuel particles of torrefied biomass after grinding and sieving operations, substantially larger char particles are produced at 1473 K from torrefied biomass than non-torrefied biomass. The release of violates is slower for torrefied biomass than non-torrefied biomass. Furthermore, torrefied biomass has a higher char yield. Mass loss caused by volatiles release is accompanied by compositional changes of char, specifically the enrichment of carbon and the loss of oxygen and, especially, hydrogen. The evolution of composition from fuel particle to char is found to be insensitive to variations in the test conditions.

The CFD simulation of devolatilization shows a large dependence of particle temperature on particle diameter. Torrefied biomass particles have a higher initial temperature than that of non-torrefied biomass because of the shorter drying period. Using a procedure to best match predicted mass loss to measured mass loss during devolatilization, optimal kinetic parameters are obtained for use in a modified two-competing rate devolatilization model. The mass loss of fuel as well as its compositional transformation in char is well simulated with this approach.

The results of this study have several implications for investigating thermochemical conversion of biomass: (1) torrefied biomass has a longer overall conversion process than the corresponding raw fuel (thus a reactor with a large dimension (or lower gas flow rate) may be required to ensure complete conversion of torrefied biomass), (2) char produced from rapid devolatilization contains non-negligible amounts of oxygen and hydrogen. With a slight modification, the two-competing devolatilization model can adequately predict the char yield and composition of char throughout devolatilization of biomass, (3) biomass fuel often contains a variety of shapes and sizes of particles, and (4) extensive fragmentation of biomass occurs during rapid devolatilization. The simplified CFD model presented in this study can only capture some basic phenomena of the devolatilization process. More advanced CFD model, including treatment of non-spherical particles, shrinkage of particles, and fragmentation is required to reveal the complex structural changes of biomass particles during devolatilization.

5.2 Paper II Effect of torrefaction on physical properties and conversion behavior of high heating rate char of forest residue

In this paper, the effect of torrefaction on physical properties and conversion behavior of biomass char has been investigated. Char from FR and TFR was produced at high temperatures and high heating rates using a DTR under dilute fuel loading conditions. Torrefaction i found to strongly influence the morphology of the processed particles. Analysis of the particle size distributions after applying the same grinding and sieving procedure shows that TFR particles are smaller than FR particles, indicating that the grindability is improved in the torrefaction process. However, comparison of particle sizes after devolatilization reveals that the volume-mean size of TFR char particles is significantly larger than that of FR char. It is partially attributed to more intensive fragmentation of the FR particles during the devolatilization process. A tracer method has been used to assess the conversion of carbon, oxygen and hydrogen in FR char and TFR char after oxidation and gasification reactions in the DTR. Calcium, manganese, barium, and magnesium are found to be suitable tracers for both types of char. The widely used tracer, total ash content, is found to be very suitable for estimating conversion of FR char, but only roughly suitable for assessing conversion of TFR char. The results show that the fractional release rate of hydrogen in both types of char is much faster than that of the other organic elements. In contrast to previous studies of coal char conversion, the fractional release rate of oxygen is slower than that of the total mass for both types of biomass char in this study. In addition, TFR char shows a lower reactivity than FR char. Compared to FR char, TFR char has a larger particle size, more aromatic carbon structure, lower O/C ratio, and less catalytic alkali metal contents, which may explain its lower reactivity. However, based on current experimental data, it is difficult to separate the effect of these different factors. Additional experiments should be performed in the future to clarify the impact of these factors on the observed char reactivity.

5.3 Paper III Eulerian–Lagrangian simulation of biomass gasification behavior in a high-temperature entrained-flow reactor

In this paper, an Eulerian–Lagrangian CFD model based on OpenFOAM has been constructed, validated, and applied to a laboratory-scale biomass entrained-flow reactor operating at high temperatures (1000−1400 °C). Effects of five operating parameters (reactor temperature, steam/carbon molar ratio, excess air ratio, biomass type, and particle size) on the species production, particle residence time and carbon conversion are particularly addressed. Results show that the reactor temperature has a positive effect on the quality of the product gas and rising temperatures lead to a substantial increase in the H_2 and CO productions; increasing the steam/carbon ratio increases the H_2 production but decreases the CO production; increasing the excess air ratio decreases both the H_2 and CO productions; the biomass type appears to have influence on the gasification behavior to some extent, because it results in variations in species production and carbon conversion. However, the variations are not so significant because of similar biomass nature; hence, one type can be replaced by another without any major consequences in the gasification performance. Both the CO and H_2 productions and carbon conversion decrease with an increase in particle size for all of the biomasses. Moreover, the predicted results follow the same trends as the wide range of experimental data for both pyrolysis and gasification experiments obtained from the literature [143]. Quantitative comparisons are also made and the agreement is good. Therefore, the established numerical models and chemical kinetics are suitable for simulating wood gasification in high temperature entrained-flow reactor.

5.4 Paper IV Influence of drag force correlations on periodic fluidization behavior in Eulerian–Lagrangian simulation of a bubbling fluidized bed.

In this paper, Numerical simulations of a bubbling gas-solid fluidized bed reactor have been performed in a pseudo-3D domain using the Eulerian–Lagrangian approach to investigate the effects of three widely used drag correlations on the hydrodynamic behaviors. A soft-sphere model is adopted to resolve the inter-particle and particle-wall collision dynamics. The results have been analyzed in terms of particle flow pattern, bed expansion height, bed pressure drop, and fluctuation frequency. Qualitatively, formation of bubbles and slugs and the process of particle mixing are observed to occur for all the drag models, although the Gidaspow model [79] is found to be most energetic and the Di Felice [83] and EHKL [86] models yield minor difference. Quantitatively, the mean pressure drops predicted by the three models agree quite well with each other and the amplitudes of the fluctuations measured by the standard deviation are also comparable. However, a significant difference in the frequency of pressure fluctuations is found in that the Gidaspow model [79] predicts the lowest fluctuation frequency whereas the Di Felice [83] gets the highest one. Considering that there are more than 10 drag correlations available in the literature [88,89], care must be taken to make a suitable choice for one's particular application.

The effects of restitution coefficient, friction coefficient, and spring stiffness on the fluidization behavior are also investigated in this study. It is found that no bubbling and slugging occur at all for the ideal-collision case and that both mean bed pressure drop and fluctuation frequency slightly decrease as the spring stiffness increases for all the three drag models. Finally, the discontinuity in the Gidaspow model [79] is removed by a linear interpolation scheme and no significant differences are observed in the mean bed pressure drop and fluctuation frequency between the original Gidaspow model [79] and the linear continuous model. However, fluidized beds are a huge and very complicated multi- phase-flow system, and is affected by many related issues such as container geometry, operational conditions, particle size distribution and material properties. Further modeling efforts are required to study the influence of all these parameters. Moreover, new experimental studies should be carried out using recent advancements in instrumentation engineering in order to compare with our modeling results.

5.5 Paper V CFD–DEM simulation of biomass gasification with steam in a fluidized bed reactor

In this paper, a comprehensive CFD–DEM numerical model has been developed to simulate the steam gasification of biomass in a fluidized bed reactor. Effects of different operating conditions, such as reactor temperature, steam/biomass mass ratio, and biomass injection position, on the gasification performance are analyzed. Simulation results are analyzed both qualitatively and quantitatively in terms of particle flow pattern, particle mixing and entrainment, bed pressure drop, product gas composition, and carbon conversion. Results show that higher temperatures are favorable for the products in endothermic reactions (e.g. H_2 and CO). With the increase of steam/biomass mass ratio, H_2 and CO_2 concentrations increase while CO concentration decreases. The carbon conversion decreases as the height of injection point increases owing to both an increase of solid entrainment and a decrease of particle residence time and particle temperature. Meanwhile, the integrated model has also been validated by comparing the calculated results with the experimental data. This indicates that the proposed CFD–DEM model can provide not only the macro structures at fluidized bed scale (bubble or slug) but also detailed microscopic information at the particle level which is impossible to obtain by an Eulerian–Eulerian approach. So the proposed model can be a powerful tool to gain an insight into the complex dense gas-particle flow behaviors and chemical reaction characteristics simultaneously in the process of biomass gasification in a fluidized bed reactor.

Chapter 6

Recommendations for Further Work

For further experimental studies the following are suggested:

- Following the transformation and conversion of organic elements, the vaporization and distribution of ash forming elements during torrefaction and gasification should be revealed.
- Further studies of char using the Nuclear Magnetic Resonance and the Fourier Transform Infrared Spectroscopy may aid in understanding transformation of carbon structure and functional groups during gasification process.
- Volatile gas released during rapid devolatilization should also be collected and characterized. The results could be applied to verify conversion ratios calculated by the metal tracer technique. Furthermore, the accurate measurement of the distribution of volatile gas is crucial for developing a comprehensive devolatilization model.

For further numerical studies the following are suggested:

- In order to better predict the trajectories of non-spherical biomass particles, the effect of particle shape on momentum exchange between solid and fluid should be carefully examined. A modified drag coefficient or model for the non-spherical particles, especially for the widely existed needle-like particles in our grinded biomass samples, should be developed.

- Clear fragmentation of biomass caused by volatiles release has been observed. Therefore, more dedicated fragmentation models are required to reflect structural changes of biomass particle during devolatilization process. In addition, the observed fragment size differences between non-torrefied biomass and torrefied biomass should be addressed.
- Advanced char conversion models taking into account consumption of oxygen remaining in char should be developed since the oxygen-rich nature of char is produced after rapid devolatilization.
- Inorganic alkali metals play an important role on char gasification and their catalytic effects should be implemented.
- The CFD model developed from the lab scale reactors should be further tested and verified with large scale reactors and used to study scale-up issues.
- Models account for soot formation and oxidation should be developed and implemented into the CFD simulation.

References

[1] M. Langerud, B., Størdal, R., Wiig, H., Ørbeck, Bioenergi I Norge – Potensialer, Markeder Og Virkemidler (Bioenergy in Norway – Potentials, Markets and Policy Measures), 2007.

[2] Norsk Klimapolitikk (Norwegian Climate Policy), St.meld.nr.21, Oslo, 2012.

[3] Energy Technology Perspectives 2014, IEA report, Paris, 2014.

[4] A. Limayem, S.C. Ricke, Prog. Energy Combust. Sci. 38 (2012) 449.

[5] C.A. Cardona, O.J. Sánchez, Bioresour. Technol. 98 (2007) 2415.

[6] A.J. Ragauskas, C.K. Williams, B.H. Davison, G. Britovsek, J. Cairney, C. a Eckert, W.J. Frederick, J.P. Hallett, D.J. Leak, C.L. Liotta, J.R. Mielenz, R. Murphy, R. Templer, T. Tschaplinski, Science 311 (2006) 484.

[7] T.G. Bridgeman, J.M. Jones, I. Shield, P.T. Williams, Fuel 87 (2008) 844.

[8] J.H.A. Kiel, F. Verhoeff, H. Gerhauser, B. Meuleman., in:, 16th Eur. Biomass Conf. Exhib., Valencia, 2008.

[9] J. Shankar Tumuluru, S. Sokhansanj, J.R. Hess, C.T. Wright, R.D. Boardman, Ind. Biotechnol. 7 (2011) 384.

[10] I. Pastorova, P.W. Arisz, J.J. Boon, Carbohydr. Res. 248 (1993) 151.

[11] M.R. Wooten, J.B., Crosby, B., Hajaligol, ACS Div. Fuel Chem. 46 (2001) 191.

[12] P.C.A. Bergman, J.H.A. Kiel, in:, 14th Eur. Biomass Conf. Exhib., Paris, 2005.

[13] B. Arias, C. Pevida, J. Fermoso, M.G. Plaza, F. Rubiera, J.J. Pis, Fuel Process. Technol. 89 (2008) 169.

[14] P.C.A. Bergman, A.R. Boersma, R.W.R. Zwart, J.H.A. Kiel, Torrefaction for Biomass Co-Firing in Existing Coal-Fired Power Stations, ECN Report ECN-C-05-013, Petten, 2005.

[15] J. Deng, G. Wang, J. Kuang, Y. Zhang, Y. Luo, J. Anal. Appl. Pyrolysis 86 (2009) 331.

[16] M.J. Prins, K.J. Ptasinski, F.J.J.G. Janssen, Energy 31 (2006) 3458.

[17] A. V Bridgwater, A.J. Toft, J.G. Brammer, Renew. Sustain. Energy Rev. 6 (2002) 181.

[18] P. Basu, Biomass Gasification and Pyrolysis : Practical Design and Theory, Elsevier, Burlington, 2010.

[19] M.L. de Souza-Santos, Solid Fuels Combustion and Gasification: Modeling, Simulation, and Equipment Operations, CRC Press, Boca Raton, 2004.

[20] P.L. Spath, D.C. Dayton, Preliminary Screening — Technical and Economic Assessment of Synthesis Gas to Fuels and Chemicals with Emphasis on the Potential for Biomass-Derived Syngas, National Renewable Energy Laboratory NREL Report NREL/TP-510-34929, Golden, 2003.

[21] C. Higman, M.J. Burgt, Gasification, Second Edi, Gulf Professional Publishing, 2008.

[22] I. Olofsson, A. Nordin, U. Söderlind, Initial Review and Evaluation of Process Technologies and Systems Suitable for Cost-Efficient Medium-Scale Gasification for Biomass to Liquid Fuels, University of Umeå and Mid Sweden University, 2005.

[23] A. Gómez-Barea, B. Leckner, Prog. Energy Combust. Sci. 36 (2010) 444.

[24] R. Sims, M. Taylor, J. Saddler, W. Mabee, From 1st - to 2nd-Generation Biofuel Technologies – an Overview of Current Industry and RD&D Activities, IEA Report, Paris, 2008.

[25] A. Eisentraut, Sustainable Production of Second-Generation Biofuels, IEA Report, Paris, 2010.

[26] R.E.H. Sims, W. Mabee, J.N. Saddler, M. Taylor, Bioresour. Technol. 101 (2010) 1570.

[27] W.E. Mabee, D.J. Gregg, C. Arato, A. Berlin, R. Bura, N. Gilkes, O. Mirochnik, X. Pan, E.K. Pye, J.N. Saddler, Appl. Biochem. Biotechnol. 129 (2006) 55.

[28] C. Di Blasi, Prog. Energy Combust. Sci. 34 (2008) 47.

[29] C. Di Blasi, Prog. Energy Combust. Sci. 19 (1993) 71.

[30] D. Pyle, C. Zaror, Chem. Eng. Sci. 39 (1984) 147.

[31] F. Shafizadeh, Pyrolytic Reactions and Products of Biomass. In: Overend RP, Milne TA, Mudge LK, Editors. Fundamentals of Biomass Thermochemical Conversion., Elsevier, London, 1985.

[32] M.J.J. Antal, G. Varhegyi, Ind. Eng. Chem. Res. 34 (1995) 703.

[33] H. Yang, R. Yan, H. Chen, C. Zheng, D.H. Lee, D.T. Liang, Energy & Fuels 20 (2006) 388.

[34] S.D. Stefanidis, K.G. Kalogiannis, E.F. Iliopoulou, C.M. Michailof, P.A. Pilavachi, A. a. Lappas, J. Anal. Appl. Pyrolysis 105 (2014) 143.

[35] C.A. Koufopanos, A. Lucchesi, G. Maschio, Can. J. Chem. Eng. 67 (1989) 75.

[36] M. Stenseng, A. Jensen, K. Dam-Johansen, J. Anal. Appl. Pyrolysis 58-59 (2001) 765.

[37] R. Narayan, M.J. Antal, Ind. Eng. Chem. Res. 35 (1996) 1711.

[38] R. Bilbao, J. Arauzo, A. Millera, Thermochim. Acta 120 (1987) 121.

[39] C. Branca, A. Albano, C. Di Blasi, Thermochim. Acta 429 (2005) 133.

[40] G. Várhegyi, M.J. Antal, E. Jakab, P. Szabó, J. Anal. Appl. Pyrolysis 42 (1997) 73.

[41] R. Mehrabian, R. Scharler, I. Obernberger, Fuel 93 (2012) 567.

[42] J. Li, G. Bonvicini, L. Tognotti, W. Yang, W. Blasiak, Fuel 122 (2014) 261.

[43] X. Shuangning, L. Zhihe, L. Baoming, Y. Weiming, B. Xueyuan, Fuel 85 (2006) 664.

[44] H. Tolvanen, L. Kokko, R. Raiko, Fuel 111 (2013) 148.

[45] H. Lu, E. Ip, J. Scott, P. Foster, M. Vickers, L.L. Baxter, Fuel 89 (2010) 1156.

[46] C. Dupont, L. Chen, J. Cances, J.-M. Commandre, A. Cuoci, S. Pierucci, E. Ranzi, J. Anal. Appl. Pyrolysis 85 (2009) 260.

[47] A. Bharadwaj, L.L. Baxter, A.L. Robinson, Energy & Fuels 18 (2004) 1021.

[48] S. Sun, H. Tian, Y. Zhao, R. Sun, H. Zhou, Bioresour Technol 101 (2010) 3678.

[49] M. Simone, E. Biagini, C. Galletti, L. Tognotti, Fuel 88 (2009) 1818.

[50] K. Papadikis, S. Gu, A. V Bridgwater, Chem. Eng. Sci. 64 (2009) 1036.

[51] A. V Bridgwater, Fuel 74 (1995) 631.

[52] C. Di Blasi, Prog. Energy Combust. Sci. 35 (2009) 121.

[53] M. Guerrero, M.P. Ruiz, M.U. Alzueta, R. Bilbao, a. Millera, J. Anal. Appl. Pyrolysis 74 (2005) 307.

[54] C. Fushimi, K. Araki, Y. Yamaguchi, A. Tsutsumi, Ind. Eng. Chem. Res. 42 (2003) 3922.

[55] E. Cetin, B. Moghtaderi, R. Gupta, T.. Wall, Fuel 83 (2004) 2139.

[56] E. Cetin, R. Gupta, B. Moghtaderi, Fuel 84 (2005) 1328.

[57] F. Kurosaki, K. Ishimaru, T. Hata, Carbon N. Y. 41 (2003) 3057.

[58] K. Whitty, R. Backman, M. Hupa, Carbon N. Y. 36 (1998) 1683.

[59] P. Rocca, Biomass and Bioenergy 16 (1999) 79.

[60] Y. Okumura, T. Hanaoka, K. Sakanishi, Proc. Combust. Inst. 32 (2009) 2013.

[61] K. Matsumoto, K. Takeno, T. Ichinose, T. Ogi, M. Nakanishi, Fuel 88 (2009) 519.

[62] F. Mermoud, S. Salvador, L. Vandesteene, F. Golfier, Fuel 85 (2006) 1473.

[63] J. Fermoso, C. Stevanov, B. Moghtaderi, B. Arias, C. Pevida, M.G. Plaza, F. Rubiera, J.J. Pis, J. Anal. Appl. Pyrolysis 85 (2009) 287.

[64] C. Guizani, F.J. Escudero Sanz, S. Salvador, Fuel 108 (2013) 812.

[65] A. G. Borrego, L. Garavaglia, W.D. Kalkreuth, Int. J. Coal Geol. 77 (2009) 409.

[66] C. Guizani, F.J. Escudero Sanz, S. Salvador, Fuel 116 (2014) 310.

[67] O. Karlström, A. Brink, E. Biagini, M. Hupa, L. Tognotti, Proc. Combust. Inst. 34 (2013) 2427.

[68] S. Kajitani, Y. Zhang, S. Umemoto, M. Ashizawa, S. Hara, Energy & Fuels 24 (2010) 145.

[69] C. Meesri, B. Moghtaderi, Combust. Sci. Technol. 175 (2003) 793.

[70] J.M. Jones, T.G. Bridgeman, L.I. Darvell, B. Gudka, A. Saddawi, A. Williams, Fuel Process. Technol. 101 (2012) 1.

[71] E.M. Fisher, C. Dupont, L.I. Darvell, J.-M. Commandré, A. Saddawi, J.M. Jones, M. Grateau, T. Nocquet, S. Salvador, Bioresour. Technol. 119 (2012) 157.

[72] S. Gerber, F. Behrendt, M. Oevermann, Fuel 89 (2010) 2903.

[73] F. Taghipour, N. Ellis, C. Wong, Chem. Eng. Sci. 60 (2005) 6857.

[74] J. Wang, M.A. van der Hoef, J.A.M. Kuipers, Chem. Eng. Sci. 64 (2009) 622.

[75] C. S.Campbell, Shear Flows in Granular Material, PhD thesis, California Institute of technology, 1982.

[76] P.A. Cundall, O.D.L. Strack, Géotechnique 29 (1979) 47.

[77] Y. Tsuji, T. Kawaguchi, T. Tanaka, Powder Technol. 77 (1993) 79.

[78] J. Li, J.A.M. Kuipers, Chem. Eng. Sci. 58 (2003) 711.

[79] D. Gidaspow, Multiphase Flow and Fluidization, 1st ed., Academic Press, San Diego, 1994.

[80] S. Ergun, Chem. Eng. Prog. 48 (1952) 89.

[81] C.Y. Wen, Y.H. Yu, Chem. Eng. Prog. Symp. Ser. 62 (1966) 100.

[82] C. Kloss, C. Goniva, G. Aichinger, S. Pirker, Seventh International Conference on CFD in the Minerals and Process Industries CSIRO, Melbourne, 2009.

[83] R. Di Felice, Int. J. Multiph. Flow 20 (1994) 153.

[84] R.J. Hill, D.L. Koch, A.J.C. Ladd, J. Fluid Mech. 448 (2001) 213.

[85] R.J. Hill, D.L. Koch, A.J.C. Ladd, J. Fluid Mech. 448 (2001) 243.

[86] S. Benyahia, M. Syamlal, T.J. O'Brien, Powder Technol. 162 (2006) 166.

[87] W. Du, X. Bao, J. Xu, W. Wei, Chem. Eng. Sci. 61 (2006) 1401.

[88] E. Esmaili, N. Mahinpey, Adv. Eng. Softw. 42 (2011) 375.

[89] C. Loha, H. Chattopadhyay, P.K. Chatterjee, Chem. Eng. Sci. 75 (2012) 400.

[90] D. Liu, X. Chen, W. Zhou, C. Zhao, Proc. Combust. Inst. 33 (2011) 2701.

[91] J. Bruchmüller, B.G.M. van Wachem, S. Gu, K.H. Luo, R.C. Brown, AIChE J. 58 (2012) 3030.

[92] S. Gerber, M. Oevermann, Fuel 115 (2014) 385.

[93] D.F. Fletcher, B.S. Haynes, J. Chen, S.D. Joseph, Appl. Math. Model. 22 (1998) 747.

[94] D.F. Fletcher, B.S. Haynes, F.C. Christo, S.D. Joseph, Appl. Math. Model. 24 (2000) 165.

[95] W.-H. Chen, C.-J. Chen, C.-I. Hung, C.-H. Shen, H.-W. Hsu, Appl. Energy 112 (2013) 421.

[96] C.-J. Chen, C.-I.I. Hung, W.-H. Chen, Appl. Energy 100 (2012) 218.

[97] M. Kumar, A.F. Ghoniem, Energy & Fuels 26 (2012) 451.

[98] M. Kumar, A.F. Ghoniem, Energy & Fuels 26 (2012) 464.

[99] N. Abani, A.F. Ghoniem, Fuel 104 (2013) 664.

[100] M. Vascellari, R. Arora, M. Pollack, C. Hasse, Fuel 113 (2013) 654.

[101] D.M. Grant, R.J. Pugmire, T.H. Fletcher, A.R. Kerstein, Energy & Fuels 3 (1989) 175.

[102] T.H. Fletcher, A.R. Kerstein, R.J. Pugmire, M.S. Solum, D.M. Grant, Energy & Fuels 6 (1992) 414.

[103] S. Niksa, A.R. Kerstein, Energy & Fuels 5 (1991) 647.

[104] P.R. Solomon, D.G. Hamblen, R.M. Carangelo, M.A. Serio, G. V Deshpande, Energy & Fuels 2 (1988) 405.

[105] M. Kumar, A.F. Ghoniem, Fuel 108 (2013) 565.

[106] J. Ma, S.S.E. Zitney, Energy & Fuels 26 (2012) 7195.

[107] L. Yan, B. He, X. Pei, C. Wang, X. Li, Z. Duan, Energy & Fuels 27 (2013) 6388.

[108] M. Vascellari, R. Arora, C. Hasse, Fuel 118 (2014) 369.

[109] M. Zhang, J. Yu, X. Xu, Combust. Flame 143 (2005) 150.

[110] J. Yu, M.C. Zhang, Energy & Fuels 23 (2009) 2874.

[111] G.-S. Liu, S. Niksa, Prog. Energy Combust. Sci. 30 (2004) 679.

[112] C.Y. Wen, T.Z. Chaung, Ind. Eng. Chem. Process Des. Dev. 18 (1979) 684.

[113] G. Liu, A.. Tate, G.. Bryant, T.. Wall, Fuel 79 (2000) 1145.

[114] M. Weeda, H.H. Abcouwer, F. Kapteijn, J.A. Moulijn, Fuel Process. Technol. 36 (1993) 235.

[115] S. Kajitani, S. Hara, H. Matsuda, Fuel 81 (2002) 539.

[116] X. Lu, T. Wang, Fuel 108 (2013) 620.

[117] X. Lu, T. Wang, Fuel 108 (2013) 629.

[118] T. Sato, S. Kurosawa, R.L. Smith, T. Adschiri, K. Arai, J. Supercrit. Fluids 29 (2004) 113.

[119] S.L. Wade JP, Evar WT, Bryan LH, in:, Proc. 2008 AIChE Spring Natl. Meet., n.d.

[120] W.P. Jones, R.P. Lindstedt, Combust. Flame 73 (1988) 233.

[121] X. Lu, T. Wang, Int. J. Heat Mass Transf. 67 (2013) 377.

[122] S.Z. Yong, A. Ghoniem, Fuel 97 (2012) 457.

[123] L. Chen, A.F. Ghoniem, Fuel 113 (2013) 357.

[124] L. Gibson, N. Soundarrajan, J. Spenik, J. Ma, L. Shadle, S. V. Pisupati, Energy & Fuels 27 (2013) 7681.

[125] F. Ambrosino, A. Aprovitola, P. Brachi, F.S. Marra, F. Montagnaro, P. Salatino, Fuel 114 (2013) 44.

[126] R.A. Khalil, Q. Bach, Ø. Skreiberg, K. Tran, Energy & Fuels 27 (2013) 4760.

[127] A.G.A. Borrego, D. Alvarez, Energy & Fuels 21 (2007) 3171.

[128] L. Lu, V. Sahajwalla, D. Harris, 32 (2001) 811.

[129] C. Ulloa, A. G. Borrego, S. Helle, a. L. Gordon, X. García, Fuel 84 (2005) 247.

[130] P.M. Hald, Ash Tracer Technique, Forskningscenter Risø, Denmark, 1995.

[131] H. Kobayashi, J.B. Howard, A. F. Sarofim, Symp. Combust. 16 (1977) 411.

[132] A.F. Sarofim, J.B. Howard, A.S. Padia, Combust. Sci. Technol. 16 (1977) 187.

[133] K. Froment, F. Defoort, C. Bertrand, J.M. Seiler, J. Berjonneau, J. Poirier, Fuel 107 (2013) 269.

[134] P. Thy, C.. Lesher, B.. Jenkins, Fuel 79 (2000) 693.

[135] P. Thy, B. Jenkins, S. Grundvig, R. Shiraki, C. Lesher, Fuel 85 (2006) 783.

[136] T.K. Gale, C.H. Bartholomew, T.H. Fletcher, Energy & Fuels 10 (1996) 766.

[137] R. Pace, P. Hedman, L. Smoot, Prepr. Pap. Am. Chem., Div. Fuel Chem. 27 (1982) 167.

[138] J.J. Murphy, C.R. Shaddix, Combust. Flame 144 (2006) 710.

[139] R.E. Mitchell, R.H. Hurt, L.L. Baxter, D.R. Hardesty, Compilation of Sandia Coal Char Combustion Data and Kinetic Analyses, Milestone Report, SAND92-8208; Sandia National Laboratories, Albuquerque, 1992.

[140] H. Yeasmin, J.F. Mathews, S. Ouyang, Fuel 78 (1999) 11.

[141] M.J. Wornat, R.H. Hurt, N.Y.C. Yang, T.J. Headley, Combust. Flame 100 (1995) 131.

[142] ANSYS FLUENT Theory Guide, ANSYS, Inc., Canonsburg, 2012.

[143] K. Qin, P.A. Jensen, W. Lin, A.D. Jensen, Energy & Fuels 26 (2012) 5992.

[144] K.D. Kafui, C. Thornton, M.J. Adams, Chem. Eng. Sci. 57 (2002) 2395.

[145] B.H. Xu, A.B. Yu, Chem. Eng. Sci. 52 (1997) 2785.

[146] T. Song, J. Wu, L. Shen, J. Xiao, Biomass and Bioenergy 36 (2012) 258.

Acknowledgements

First and foremost I would like to express my sincere gratitude to my main supervisor Prof. Terese Løvås for all the support and trust she has provided. She gave me complete freedom to voice and to explore my own research ideas. By sharing her experience, knowledge, competence, and values, she taught me not only how to pursue a PhD degree, but more importantly how to systematically conduct a scientific research project. She led me to overcome obstacles by offering constructive suggestions and cheered me up through the encouraging words and hearty laughter. With strong backing from her, I never had fear for confronting all the challenges in my PhD study.

I am grateful to work under co-supervision of Berta Masta Güell who organized the wonderful GasBio project. I am glad to work in such a multidisciplinary project where I could share my results and learn from others. Special thanks to Judit Sandquist for her co-supervision of my early PhD work. Thanks also go to Liang Wang for helping me characterize samples, understand experimental data, and correct manuscripts. It is enjoyable to collaborate with him. I still feel a little "guilty" when I see numerous emails that he replied to me after 11:00 pm.

My three-month stays in the Sandia National Laboratories in Livermore builds the backbone of my thesis. I wish to express my gratitude to Christopher R. Shaddix for providing me such a fantastic opportunity. He brought me to the "other side of world", the experimental studies of thermochemical conversion of solid fuels. Thanks for all the fruitful discussions and the efforts he has put into my manuscripts. I would also like to thank Manfred Geier, "the fixer", who could literally fix anything in the lab. He kept cleaning all the messes I created in the lab with the "dark cloud above my head". His strict and precise Austrian engineering skill is truly admirable. Thanks also go to Ethan Hecht for his assistant in the experiments.

I would like to thank Lihao Zhao who I met the first day when I arrived in NTNU. He provided me tremendous help through all the period of my PhD study. With the minute information and instruction from him, I spent little time familiarizing myself with living and working in Trondheim. My very first publication was also resulted from the joint

efforts with him and his supervisor Prof. Helge I. Andersson. I am especially grateful to Xiaoke Ku who patiently showed me the derivations of equations and explained me the numerical method in detail. I was greatly inspired by his down-to-earth attitude and solid mathematical foundation. His countless suggestions and inputs on CFD simulation are invaluable for my PhD work.

I wish to express my gratitude towards all the colleagues and friends at the Department of Energy and Process Engineering: Bjørn, Luca, Rengarajan, Vu, and Jonas for every joyful coffee break and Friday-risgrøt-gathering; Erik for offering me a comfortable and affordable place to live; Amlaku and Tymofii for happily sharing apartment with me; Han, Qingqing, Wei, Peng, Chao, and Zhequan for all those cheerful non-work-related conversation in cordial and familiar Chinese. In addition, I would like to thank the administrative staffs in our department, especially Gerd Randi and Anita for being so helpful.

I am particularly grateful to my best friends Danfeng Li and Dainai Zhang who grew up with me. Thank you for letting me share with you all my joys and sorrows during my PhD study. All those travels with you in the past three years have made my life colorful and exciting.

Finally, special thanks are given to my parents Xiaomin Zhang and Mao Li. I can always deeply feel all your love no matter how far away I am from home.

Selected Papers

Paper I

Experimental and modeling study of the effect of torrefaction on the rapid devolatilization of biomass

Tian Li, Liang Wang, Xiaoke Ku, Berta Matas Güell, Terese Løvås, Christopher R. Shaddix

Submitted to *Energy & Fuels*

Is not included due to copyright

Paper II

Effect of torrefaction on physical properties and conversion behavior of high heating rate char of forest residue

Tian Li, Manfred Geier, Liang Wang, Xiaoke Ku, Berta Matas Güell, Terese Løvås, Christopher R. Shaddix

Energy & Fuels, 29, 177−184, 2015

---

energy&fuels

Article

pubs.acs.org/EF

Effect of Torrefaction on Physical Properties and Conversion Behavior of High Heating Rate Char of Forest Residue

Tian Li,*[†] Manfred Geier,[‡] Liang Wang,[§] Xiaoke Ku,[†] Berta Matas Güell,[§] Terese Løvås,[†] and Christopher R. Shaddix[‡]

[†]Department of Energy and Process Engineering, Norwegian University of Science and Technology, Kolbjørn Hejes vei 1b, 7491 Trondheim, Norway

[‡]Combustion Research Facility, Sandia National Laboratories, Livermore, California 94550, United States

[§]SINTEF Energy Research, P.O. Box 4761, Sluppen, 7465 Trondheim, Norway

ABSTRACT: In the work reported here, both forest residue (FR) and torrefied forest residue (TFR) were devolatilized in a drop tube reactor at 1473 K at a heating rate greater than 10^4 K/s. The physical properties of parent fuel particles and their corresponding char particles were examined by using a scanning electron microscope and a granulometer. After the same milling and sieving process, the TFR particles had a smaller size and smaller aspect ratio than the FR particles. The char particles consisted of two types of particles with different sizes and morphologies: a small particle mode (presumably char fragments) and a large particle mode. The volume fraction of char fragments in the TFR char was considerably less than for the FR char. Both types of char were converted in a drop tube reactor under oxidation and gasification conditions at 1473 and 1573 K, respectively. The total organic mass loss and release of individual organic elements during char conversion were determined using a tracer method. Calcium, manganese, barium, and magnesium were found to be suitable for use as tracers. The fractional carbon conversion rate of TFR char was found to be slower than that of FR char under both oxidation and gasification conditions. The fractional release rate of hydrogen was much higher than that of total organic mass loss, while the corresponding oxygen release was lower for both types of char and for different reactive environments.

1. INTRODUCTION

Biomass is an abundant carbon-neutral renewable resource, whose enhanced use would reduce both CO_2 emissions and society's dependence on fossil fuels. Among the various types of biomass, lignocellulosic biomass has attracted significant interest for bioenergy purposes in recent years due to its wide availability and minimal impact on traditional agricultural production. Moreover, lignocellulosic biomass is often derived from forest and agricultural sectors as wastes or byproducts at low cost. There have been several recent reviews of production of biofuel from lignocellulosic biomass.[1−3]

Forest residue (FR) is one of the most relevant sources of lignocellulosic biomass for producing heat, power, and biofuels. In Northern Europe, there are significant quantities of FR available. For example, the potential annual harvest of FR is around 2.7 million m^3 per year in Norway.[4] The Norwegian government has a goal of increasing the use of bioenergy from 14 TWh by 2008 to 28 TWh by 2020, and particular attention has been given to FR to meet this target.[5] However, further utilization of FR is often limited because of its inherent fuel properties such as low energy density, heterogeneous size and shape, and high moisture content. Torrefaction is a potentially promising approach to upgrade FR into high quality fuel for efficient thermochemical conversion.[6] During the torrefaction process, biomass is exposed to an inert atmosphere in the temperature range of 473−573 K. Torrefaction can significantly improve the energy density, water resistance, and grindability of biomass. Compared to raw material, torrefied biomass is superior in terms of storage, transportation, and energy production.[7] Furthermore, the energy loss associated with torrefaction can be partly recuperated by integrating torrefaction with thermal process technologies such as gasification.[8] However, a better understanding of the behavior of torrefied biomass during its thermochemical conversion is needed.

Thermochemical conversion of biomass, such as through combustion or gasification, is a complex process. Primarily, it consists of two partially overlapping steps: (1) pyrolysis of biomass to produce volatiles and solid char, and (2) conversion of the volatiles and solid char. Because heterogeneous reactions are inherently slow compared to devolatilization of raw fuel particles, char conversion is usually considered to be the rate-limiting step of the whole conversion process.[9] Depending on the temperature and the characteristic gas atmosphere, either char oxidation reactions with oxygen or gasification reactions with carbon dioxide and steam may be important. In fact, even in combustion environments, in which oxidation reactions have been widely assumed to be dominant, recent measurements and analysis have revealed that gasification reactions can play an important role.[10,11] As a result, knowledge of both gasification and oxidation behavior of char is crucial for a better understanding of the efficient thermochemical conversion of biomass.

A comprehensive review of the conversion behavior and reactivity of lignocellulosic biomass char has been given by Di Blasi.[12] The influence of several factors, such as heating rate,

Received: July 15, 2014
Revised: December 8, 2014
Published: December 8, 2014

DOI: 10.1021/ef5016044
Energy Fuels 2015, 29, 177−184

Table 1. Chemical Properties of Parent Fuel Particles and Corresponding Char

		parent biomass		char	
		FR	TFR	FR	TFR
ultimate analysis (dry ash free, wt %)	C	52.1	59.5	69.8	78.1
	H	6.1	5.6	2.7	2.2
	N	0.5	0.6	0.5	0.7
	O[a]	41.3	34.3	27.0	19.0
ash (dry basis, wt %)		2.0	2.9	14.7	10.8
major ash elements in corresponding parent biomass and char (dry basis, wt %)	Si	0.4817	1.0200	1.7709	1.0744
	Ca	0.4972	0.7498	3.7288	2.4194
	K	0.2296	0.3302	1.7886	1.1242
	Fe	0.0140	0.0383	0.1139	0.1526
	Mn	0.0659	0.0882	0.4735	0.2964
	Na	0.0087	0.0473	0.1383	0.0828
	Mg	0.0528	0.0707	0.3676	0.2256
	Al	0.0480	0.0756	0.1699	0.1340
	Zn	0.0084	0.0111	0.0272	0.0122
	Ba	0.0065	0.0106	0.0484	0.0275

[a] Oxygen content was calculated by difference.

temperature, and external pressure, on char reactivity was thoroughly reviewed and discussed. The thermal histories experienced by fuel particles during pyrolysis have a strong effect on char reactivity. As fuel particles are heated to a high temperature at a high heating rate, volatiles are rapidly released in concert with the destruction of the original cell wall structure. Therefore, high temperature and high heating rate promote formation of char particles with a macroporous structure that facilitates reactant penetration and therefore char reactivity.[13−17] However, because of thermal annealing, the concentration of active sites on the char decreases with prolonged retention time at high temperature, decreasing char reactivity.[13,18] At low heating rates, the natural microporosity of the fuel particles is better preserved.[19] However, it is believed that microporosity contributes less to char reactivity at high temperatures than a macroporous structure created at high heating rate.[14] In general, char reactivity is reduced for devolatilization at elevated external pressure. High external pressure impedes volatile release and causes deposition of secondary char fragments and reduction of active sites.[15,16] Moreover, the negative effect of external pressure on char reactivity may be partly attributed to the formation of graphitic structure in chars produced at high external pressures.[15,20]

Recently, increased efforts have been given to investigate the characteristics and reactivity of biomass char produced at high temperature and high heating rate conditions that are relevant to industrial reactors. Drop tube reactors (DTRs) or entrained flow reactors (EFRs) are often used for achieving such intense conditions for thermal conversion of biomass. The reactivity of high heating rate biomass char under different combustion and/or gasification conditions has been previously studied and reported.[15,16,21−29] However, publications regarding the effects of torrefaction on the conversion behavior of high heating rate char are scarce. As reported by Jones et al.[28] and Fisher et al.[29] devolatilization of raw willow and torrefied willow was carried out in a pyroprobe at 1273 K with a heating rate around 1000 K/s and in a DTR at 1173 K with a heating rate over 500 K/s, respectively. The reactivity of the resultant char samples was further investigated using a thermogravimetric analyzer (TGA). It was found that char produced from torrefied willow has a lower reactivity than char produced from raw willow. In addition, torrefaction was reported to have a significant impact on the reactivity of char samples produced at a high heating rate.[29] However, to the best of the authors' knowledge, the effect of torrefaction on the reactivity of forest residue char produced at high heating rate conditions has not been previously studied.

The fuel conversion rate is one of the key aspects that needs to be determined for prospective fuels. Ash tracer techniques have been developed and applied to quantify the conversion of coal and coal char in DTRs for several decades.[30−33] However, the ash tracer method has been rarely applied for assessing the conversion of biomass fuel at high temperature[23−25,34] due to the small contents of suitable refractory tracer elements. Consequently, the applicability of the ash tracer method for studying the thermal conversion of biomass requires further evaluation.

The main objective of this work was to investigate the effect of torrefaction on the characteristics and conversion behavior of FR char produced from a DTR at a high heating rate. The morphology and composition, including the microstructure, diameter distribution, and organic contents of the char and solid residues collected from reactivity experiments were examined. The char conversion behavior was also evaluated using the DTR instead of a traditional TGA, because conversion of solid fuel particles in a TGA under high reaction rates are influenced by heat and mass transfer associated with the sample crucible (or pan) and multiparticle interactions.[35,36] An elemental tracer technique was carefully assessed and used to determine organic element release and total char conversion.

2. EXPERIMENTAL SECTION

2.1. Materials and Torrefaction. The fuel studied was FR collected in the Hobøl forest in Southern Norway, which mainly consists of tops and branches (including needles) of Norway spruce. It was ground and compressed to 6 mm pellets without additional binders. Torrefied forest residue (TFR) was produced in a torrefaction reactor consisting of four electrically heated horizontal screw conveyors and one water-cooled horizontal screw conveyor positioned on top of one another. The pellets fed from the top of the reactor were initially heated at 498 K for 5 min, torrefied at 548 K for 30 min, and then cooled to room temperature before being discharged from the reactor. The reactor was purged with N_2 to ensure inert conditions during operation. The details of the torrefaction process have been presented elsewhere.[37] Both FR and TFR pellets were ground using a

Thomas Model 4 Wiley Mill and then sieved to the size range of 212–300 μm. The ultimate analysis, ash contents, and major ash elements of both types of sieved fuel particles, and their corresponding char are listed in Table 1.

2.2. Drop Tube Reactor. Both char production and char reactivity experiments were carried out in an electrically heated DTR (Figure 1), located at the Combustion Research Facility of Sandia National Laboratories, Livermore, California. The DTR features a 1.5 m long vertical reactor section (with a diameter of 5.08 cm) and a 1.0 m long horizontal gas preheater section. Its operation range spans temperatures up to 1650 K and pressures up to 20 atm. Particle and gas samples for further analysis can be collected at different positions along the (vertical) reactor section. The particulate fuel samples are continuously fed into the reactor by a custom-made particle feeder on top of the DTR. The feeding rate is determined by the rate of displacement of the fuel-containing test tube and is therefore a volumetric rate (differences in bulk density thus result in different mass feeding rates). Fuel particles similar in size will thus enter the reactor in roughly the same number per unit time, if the rate of displacement is the same.

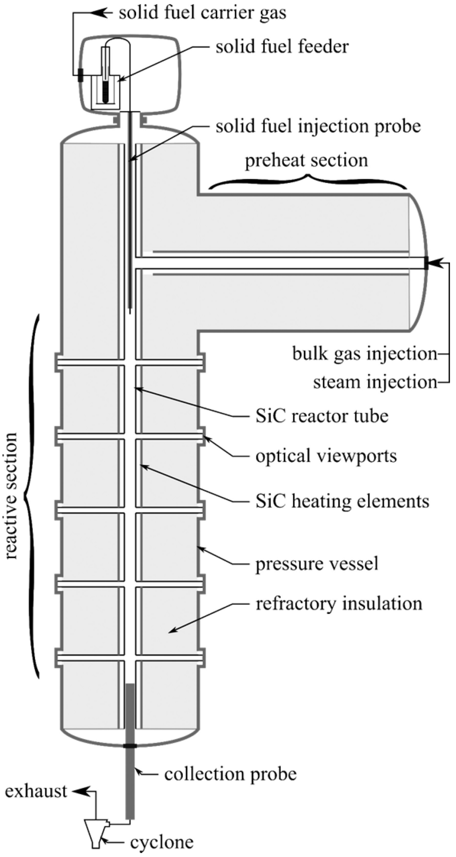

Figure 1. Schematic of the drop tube reactor at Sandia National Laboratories.

2.3. Char Production Procedure. Char particles were prepared from both FR and TFR. The sieved fuel particles were supplied by the feeding system at an approximate mass flow rate of 50 g/h. A 4 standard liter per minute (SLPM) room temperature N_2 carrier gas transported fuel particles into the DTR through a water-cooled tube. A mass flow controller metered 182 SLPM of N_2 into the horizontal gas preheat section, where it was heated to the desired reaction temperature. After the heated N_2 stream entered the reactor tube, it first passed a honeycomb straightener and then mixed with the cold particle-laden carrier flow. The average velocity of gas in the vertical test section was 6.2 m/s. The particles passed through the reactor, which was set at 1473 K, and were extracted by a water-cooled sampling tube positioned near the bottom of the reactor. At the tip of the sampling tube, 40 SLPM of cool N_2 quench flow was introduced. The distance between the tip of the feeding tube (where mixing of hot N_2 gas and fuel particles occurred) and the quench gas inlet in the sampling tube was set to 101 cm for all char production experiments. The resulting char particles were collected using a cyclone separator at the end of the sampling tube. Because of the low char yield from one single experiment, char was produced from multiple experiments but with good reproducibility. The char yields of FR and TFR were approximately 14% and 33%, respectively, according to metal tracer analysis (to be described in detail in section 2.6).

A CFD model was developed with Ansys Fluent 14.0 to estimate particle residence time and particle heating rate. The computational domain contains the fuel feeding tube, sampling tube, and both horizontal and vertical sections of the DTR. Boundary conditions, such as gas flow rates and gas composition, were configured according to corresponding experimental conditions. Radiation was treated using the discrete ordinates model. The heat transfer characteristics of the model were validated previously collected data on gas temperature profiles in the DTR as a function of flow rates. Fuel and char particles were simulated using a Lagrangian approach. A large numbers of particles, varying from 60 000 to 80 000, were tracked at each experimental condition. The particle residence time was calculated by averaging the residence times of all particles at a given reactor position and condition. However, because of the wide size distributions of the fuel particles and the reduction in particle size after devolatilization, it is difficult to precisely quantify the particle heating rate during the char production process. The maximum particle heating rate was calculated to always be greater than 10^4 K/s, with smaller particles experiencing a heating rate of approximately 10^5 K/s. The particle residence time during the char production step was approximate 0.2 s.

2.4. Char Gasification and Oxidization Experiments. Conversion of char under gasification and oxidation conditions was also carried out in the DTR system. In the gasification experiments 50 SLPM of pure CO_2 was injected into the gas preheater. A slightly higher reactor temperature (1573 K) was used, on account of the expected low reaction rate of CO_2 with the char. The DTR was purged with pure CO_2 for at least 5 min prior to each experiment. The char oxidation experiments were carried out with a similar procedure, but with the reactor operating at 1473 K. However, considering the high oxidation rate of the biomass char at such a temperature, a mixture of 2.0% O_2 in N_2 was chosen (180 SLPM N_2 and 3.6 SLPM O_2) to avoid complete char burnout and facilitate the assessment of reactivity differences of the two fuel types. Residual char samples were collected at three different heights in the DTR for further characterization and reactivity study. The corresponding residence times were calculated by CFD simulation as 0.16, 0.26, and 0.36 s for the gasification experiments, and 0.08, 0.14, and 0.19 s for the oxidization experiments. Char burnout was estimated from the tracer technique detailed in section 2.6. The feeding rate of FR char and TFR char was approximately 40 g/h using a 4 SLPM N_2 carrier flow.

2.5. Characterization Method. The microscopic structures of parent fuel particles, char particles, and residues collected from the char gasification and oxidization experiments were characterized using a scanning electron microscope (SEM, HITACHI S-3400). Elementary analysis was carried out using an element analyzer (EA-1008 CHNS-O). According to ASTM standard, the oxygen content was calculated by difference after determining the content of C, H, N, and S. Average values of the elemental composition of each sample were calculated from at least three duplicate analyses. The ash contents of parent fuel particles and corresponding char samples were determined using a TGA (TA Instrument SDT Q600). Approximately 10 mg of sample was oxidized in air at 823 K until the weight of the residues was stable. A similar method has been applied in another study.[23] For each sample, at least three duplications of ash content determination were performed to get more reproducible results. The content of ash forming elements in the samples was analyzed by inductively coupled plasma mass spectrometry (ICP-MS) and inductively coupled plasma optical emission spectrometry (ICP-OES). The diameter distributions of the parent fuel particles and char particles were measured using a laser diffraction analysis (Beckman Coulter LS230).

2.6. Ash Tracer Technique. The extent of fuel conversion can be calculated from the changes in the content of nonvolatile tracer elements and organic elements from the original fuel to the partly reacted sample. Specifically, the conversion ratio of carbon, X_{carbon}, is defined as

$$X_i = 1 - \frac{Tr_0}{Tr}\frac{Q_{\text{carbon}}}{Q_{\text{carbon},0}} \tag{1}$$

where $Q_{\text{carbon},0}$ and Q_{carbon} represent the mass fraction of carbon in the char before and after char conversion, respectively. Tr_0 and Tr are the contents of the selected tracer element in the char before and after char conversion. For a reliable tracer element, it should not volatilize over the investigated experimental conditions and should also be present at such a quantity in the raw fuel that it can be readily measured with small uncertainty. In a number of studies, the total ash content has been used as a tracer for assessing fuel conversion.[23−25,38−41] However, decomposition and vaporization of some inorganic mineral compounds[30,42] may yield biased estimates of ash content and consequently of fuel conversion. On the basis of thermodynamic equilibrium calculations, titanium, silicon, calcium, manganese, barium, and magnesium, all present in wood, are stable at temperatures as high as 1573 K.[43] In addition, experimental studies have shown that calcium, manganese, and magnesium only slightly volatilize up to 1673 K.[44,45] Because of their relatively refractory nature, titanium,[32,46−49] silicon,[32,34,48] aluminum,[32,48,49] calcium,[49] magnesium,[49] and iron[49] have been previously used as tracers to evaluate weight loss of fuel at high temperature. In the present work, we have chosen calcium, manganese, barium, and magnesium as fuel tracers. Titanium was not selected because of the low concentration in tested fuel samples. Silicon was also not considered, to avoid potential interferences from entrained particles from the reactor's thermal insulation.

3. RESULTS AND DISCUSSION

3.1. Effect of Torrefaction on Morphology of Parent Fuel and Char Particles.

SEM images of the parent fuel particles and corresponding char particles are shown in Figure 2. The parent FR is a mixture of fibrous particles with irregular shapes and different aspect ratios. The fracture properties of wood particles (during milling) are strongly related to their cellular structure.[50] Wood strength is anisotropic (stronger in the direction of wood fibers than across the fibers). Therefore, the long needlelike particles in the direction of the fiber axis in Figure 2a are most likely the wood from tree branches. Compared to wood, the strength properties of bark are much more isotropic, and hence the particles with rather block-like shapes could be the ground bark. During sieving of the milled fuel samples, the sieve was easily blocked by parent FR particles, due to the presence of particles with large aspect ratios. As shown in Figure 2d, in comparison to FR particles, the TFR contains more isolated particles and fewer long needlelike fiber particles were observed. In addition, the TFR particles have small aspect ratios and a relatively homogeneous particle size. Also, there is a noticeable reduction in the quantity of isolated fiber branching on the TFR particle surfaces compared to the FR particle surfaces. The mechanical strength and elasticity of wood decrease as a result of torrefaction treatment.[51] As a consequence of shape differences of particles, significantly more TFR particles were collected with sizes less than 212 μm after the milling and sieving processes than for FR.

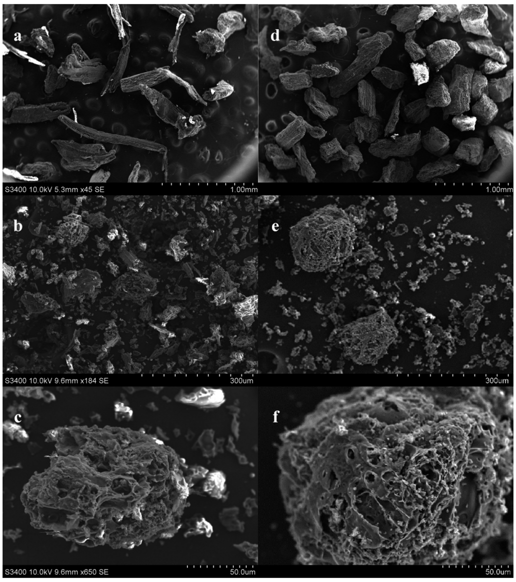

Figure 2. SEM images of parent fuel particles (a: FR parent, d: TFR parent) and corresponding char produced at high heating rate (b and c: FR char, e and f: TFR char). Images of TFR (d, e, and f) were originally taken at magnification of 44, 152, and 550, respectively. They were resized to the same magnification for corresponding images of FR.

Regardless of whether the FR was torrefied, the resulting char particles are smaller than their corresponding parent particles. Some of this size reduction would be expected due to conversion of a large fraction of the fuel mass during devolatilization. However, the presence of a large number of much smaller particles in the produced FR and TFR char residues might be partially related to intensive fragmentation of fuel particles occurred during the severe devolatilization process. In addition, collection of the char particles in the cyclone may have resulted in some char fragmentation. It can be seen from Figure 2e that two characteristic types of TFR char particles are present: one with a large spherical shape (Figure 2f) and another with much smaller irregular shapes, suggestive of char fragments. The FR char particles shown in Figure 2b also appear to exhibit two major size groups, but the larger particles (Figure 2c) seem somewhat smaller than the larger TFR particles and more irregular than the TFR char. A similar finding was also reported by Fisher et al.,[29] who observed a deformed fibrous structure and a spherical cenospheric open shell structure for raw willow char and torrefied willow char, respectively. The authors concluded that the char morphology differences resulted mainly from initial particle size differences. In our study, both fuels were sieved into narrow size fractions before converting them to char. Although the TFR particles are slightly smaller than the FR particles (see also section 3.2), such a size effect is a minor concern. More likely, the FR fuel devolatilized more explosively than the TFR fuel, due to the higher content of volatiles in FR particles.

Both FR and TFR char particles have a pronounced porous structure with openings and fissures as shown in Figure 2c,f. The multivacuolated structures are mainly caused by rapid release of volatiles, which increases the microscopic surface area. The visual appearance of both chars in the present work is consistent with findings of char produced in DTRs as reported previously.[15,16,22,29,52] One should note that relatively high heating rate char can also be produced through rapid pyrolysis using a wire mesh reactor[15,53,54] and a high frequency furnace.[55] However, char particles from such processes are normally less porous with smoother surfaces. This aspect arises primarily because the char particles need to be cooled down before collection and therefore experience high temperatures for a longer duration than chars produced using a DTF with rapid particle quench during collection.[15,55] During the cooling process, polymerization and resolidification of tarry vapors produced during rapid pyrolysis may occur, which condense on char particle surfaces and cause reduction of particle porosity and surface areas.[56]

3.2. Effect of Torrefaction on Size Distribution. Figure 3 shows the particle size distribution of parent fuel and corresponding char samples. It can be clearly seen that upon torrefaction, the volume frequency peak of the parent fuel shifts to a smaller diameter. Both types of fuel particles were produced following the same grinding and sieving procedure. Hence, the size reduction of torrefied fuel can be attributed to an improvement of the grindability, as also found by Repellin et al.[57] The particles of both types of char are much smaller than the particles of the respective parent material as a consequence of particle shrinkage and fragmentation (consistent with the SEM results discussed earlier). The size distributions of both raw and torrefied fuels appear to be composed of two distinct unimodal distribution functions. The one with a peak around 105 μm is presumably associated with whole, unfragmented particles. The other one with a broad peak around 30 μm might represent fines formed due to intensive fragmentation of raw feedstock particles. The noticeable difference in the shape of the size distributions for the char stems from the relative distribution of “shrunk” intact particles and fragmented particles. While the char from the torrefied material retains a predominant fraction of unfragmented particles, most of the mass of the char from the raw material is found in small particle fragments.

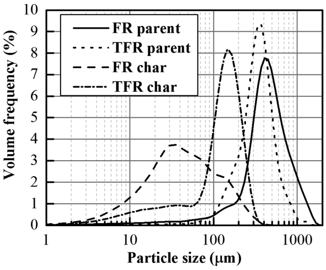

Figure 3. Size distribution of parent fuel particles and char produced at high heating rate.

3.3. Effect of Torrefaction on Char Conversion Behavior. *3.3.1. Comparison of Different Tracers.* Char conversion, represented by the carbon conversion ratio X_{carbon}, is shown in Figure 4. It was determined by analyzing the changes in the contents of four nonvolatile ash-forming elements (calcium, manganese, barium, and magnesium) and total ash in the char samples before and after conversion at different conditions. The X_{carbon} calculated from these four tracer elements lies consistently within 2 percentage points of the average conversion ratios for these four tracers for both FR and TFR. The X_{carbon} calculated by the total ash content agree well with the X_{carbon} calculated by other tracer elements for FR char, while significant differences exist for TFR char. For consistency for both types of char, the conversion ratios in later discussion were obtained by averaging the values calculated by those four tracer elements. It should be noted, however, that if one were to use the total ash content as a tracer, even for the TFR char, the deduced trends with burnout would likely not be greatly different.

3.3.2. Effect of Torrefaction on the Conversion of Elements of Char Gasification and Oxidation. As shown in Figure 4, the carbon conversion rates that can be deduced from the measured char loss as a function of residence time do not extrapolate linearly back to zero conversion at $t = 0$. Rather the rate appears to be significantly faster over the first 30−40% of char conversion than at later times. This behavior might be explained by the reduction of reaction surface at the late stage of conversion of char particles, as predicted by some models,[24,58,59] or it might reflect the effects of thermal annealing of the char. In agreement with previous results,[28,29,60] the carbon conversion rate of the torrefied fuel char is noticeably slower than that of the raw fuel char under both gasification and oxidation conditions. This difference in char reactivity might be explained by differences in the char particle size distribution. As shown in Figure 3, FR char particles are significantly smaller than the TFR char particles and therefore have a greater ratio of external surface to volume. In addition, the transformation of carbon structure of lignocellulosic biomass during torrefaction may also ultimately affect char reactivity. A previous study has suggested that the amount of both aromatic carbons and the aromatic ring clusters increases in torrefied biomass.[61] It has been reported that after torrefaction, cellulose with randomly and highly cross-linked precursors tends to yield char with lumping carbon clusters (consisting of a large number of cross-linked monomers connected by glycosidic and hydrogen bonds) in the fast pyrolysis process.[62,63] The potentially more aromatic and larger carbon clusters would be expected to reduce the reactivity of char produced from TFR.

It is well-known that alkali metals have a catalytic effect and promote conversion of low rank coals and char produced from them especially at low temperatures.[64−67] A similar catalytic effect for calcium, sodium, and potassium on the reactivity of biomass char produced at high heating rate was also recently reported.[24,25] As shown in Table 1, FR char contains more alkali metals than TFR char (although both chars come from the same feedstock, the torrefied material contains more carbon relative to the amount of minerals present). Thus, one would expect higher intrinsic reactivity of FR char than TFR char.

The extent of carbon, hydrogen, and oxygen release for both types of char are presented in Figure 5. The diagonal unity line in each subplot represents the total release of organic mass. Data points above and below the line indicate that the release rate is, respectively, higher and lower than the total daf mass release rate. The fractional release rate of hydrogen is seen to

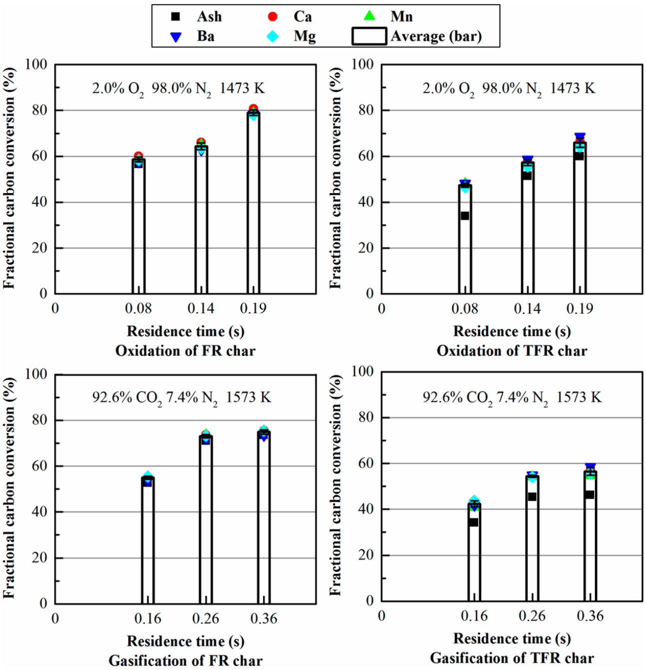

Figure 4. Fractional carbon conversion of char calculated by use of different tracers.

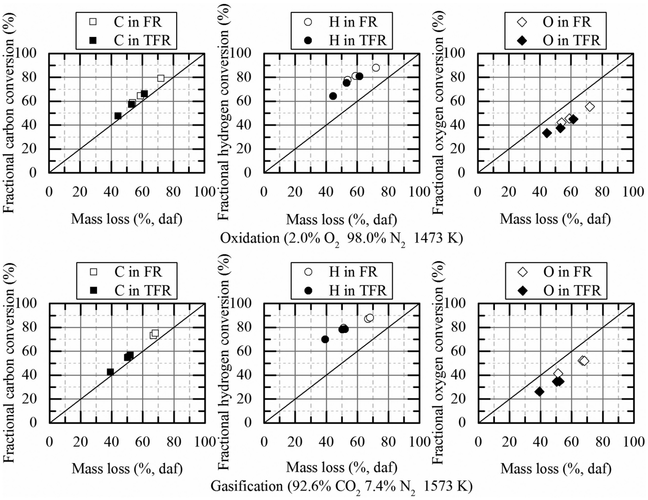

Figure 5. Fractional organic element conversion vs daf mass loss for chars produced from FR and TFR (oxygen content was calculated by difference).

be faster than that of oxygen or carbon, for both types of char. The fractional release rate of oxygen is slower than loss of the organic mass. In addition, oxygen content in the char remains at high levels even at the highest conversion stage of char, which accounts for approximately 50% of the organic portions of the char. Similar findings were reported for char produced from both woody biomass by Matsumoto et al.[24] and Wornat et al.[34] and from low rank coals by Mitchell et al.[32] The fast release of hydrogen is expected since the C−H bond is easily broken and labile peripheral groups such as −OH and −COOH group are more readily released than aromatic carbon.[32] The slow release of oxygen suggests that a significant amount of the oxygen in char is in the form of aliphatic ether structures like C−O−C instead of alcohol (−OH) groups or carbonyls (−COOH). It is also interesting to note differences between biomass char conversion and coal char conversion. As reported in previous studies, the fractional release rate of both hydrogen and oxygen is greater than the daf mass loss for intermediate rank coal char under combustion conditions.[32,48] No obvious effect of torrefaction can be observed in Figure 5. The release of oxygen for FR char seems to be slightly faster than for TFR char. As mentioned before, this may be due to the differences of distributions of oxygen moieties in char. Further study of char structure using nuclear magnetic resonance and Fourier transform infrared spectroscopy may aid in understanding these behaviors.

Some studies have associated the reactivity of biomass char with the oxygen to carbon ratio (O/C ratio) of the char.[24,34] Because of dehydration and release of volatile organic products (mostly CO and CO_2)[61,63,68] during torrefaction, TFR has a lower O/C ratio of 0.58 compared to 0.79 for FR. Following further devolatilization in the char production processes, the TFR char has a lower O/C ratio of 0.24 compared to that of FR char, which is about 0.39. Surprisingly, as shown in Figure 6, O/C ratios increase with carbon consumption regardless of the reactive environment and type of char. In addition, as displayed in Figure 6, the change of the O/C ratios follows the same trend for the same type of char for both oxidation and gasification conditions. This trend of increasing O/C with burnout suggests that char carbon that is *not* bonded to oxygen is preferentially consumed. Further support for this interpretation is given by the observation that the oxidation and gasification rates appear to be decreasing with increasing conversion, even as the O/C ratio increases.

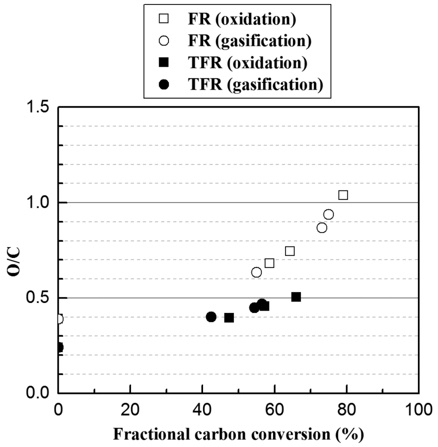

Figure 6. Evolution of O/C ratio of char during char conversion (oxygen content was calculated by difference).

4. CONCLUSION

A Norwegian forest residue was used to study the effect of torrefaction on physical properties and conversion behavior of biomass char. Char from FR and TFR was produced at high temperatures and high heating rates using a DTR under dilute fuel loading conditions. Torrefaction was found to strongly influence the morphology of the processed particles. Analysis of the particle size distributions after applying the same grinding and sieving procedure shows that TFR particles are smaller than FR particles, indicating that the grindability is improved in the torrefaction process. However, comparison of particle sizes after devolatilization reveals that the volume-mean size of TFR char particles is significantly larger than that of FR char. It is partially attributed to more intensive fragmentation of the FR particles during the devolatilization process. A tracer method was used to assess the conversion of carbon, oxygen, and hydrogen in FR char and TFR char after oxidation and gasification reactions in the DTR. Calcium, manganese, barium, and magnesium were found to be suitable tracers for both types of char. The widely used tracer, total ash content, was found to be very suitable for estimating conversion of FR char, but only roughly suitable for assessing conversion of TFR char. The results show that the fractional release rate of hydrogen in both types of char is much faster than that of the other organic elements. In contrast to previous studies of coal char conversion, the fractional release rate of oxygen is slower than that of the total mass for both types of biomass char in this study. In addition, TFR char shows a lower reactivity than FR char. Compared to FR char, TFR char has a larger particle size, more aromatic carbon structure, lower O/C ratio, and less catalytic alkali metal contents, which may explain its lower reactivity. However, based on current experimental data, it is difficult to separate the effect of these different factors. Additional experiments should be performed in the future to clarify the impact of these factors on the observed char reactivity.

■ AUTHOR INFORMATION

Corresponding Author

*Telephone: +47 73592696. E-mail: tian.li@ntnu.no.

Notes

The authors declare no competing financial interest.

■ ACKNOWLEDGMENTS

This work was carried out within the GasBio project, funded by the Research Council of Norway and industry partners. Support was also provided through the Sandia's Laboratory Directed Research and Development (LDRD) program. The authors would like to thank Ethan Hecht from Sandia for providing the schematic of the reactor and for his assistance with the experiments at Sandia. Sandia is a multiprogram laboratory operated by Sandia Corporation, a Lockheed Martin Company, for DOE's National Nuclear Security Administration under Contract DE-AC04-94AL85000.

■ REFERENCES

(1) Limayem, A.; Ricke, S. C. *Prog. Energy Combust. Sci.* **2012**, *38*, 449–467.

(2) Cardona, C. A.; Sánchez, O. J. *Bioresour. Technol.* **2007**, *98*, 2415–2457.

(3) Ragauskas, A. J.; Williams, C. K.; Davison, B. H.; Britovsek, G.; Cairney, J.; Eckert, C. A.; Frederick, W. J.; Hallett, J. P.; Leak, D. J.; Liotta, C. L.; Mielenz, J. R.; Murphy, R.; Templer, R.; Tschaplinski, T. *Science* **2006**, *311*, 484–489.

(4) Langerud, B., Størdal, R., Wiig, H., Ørbeck, M. *Bioenergi i Norge – potensialer, markeder og virkemidler (Bioenergy in Norway – Potentials, Markets and Policy Measures)*; ØF-rapport nr. 17/2007; Report for Norwegian Ministry of Petroleum and Energy: Lillehammer, November 2007.

(5) *Norsk klimapolitikk (Norwegian Climate Policy), St. meld. nr.21*; Det Kongelige Miljøverndepartementet; The Royal Ministry of the Environment, Oslo, Norway, 2012.

(6) Bridgeman, T. G.; Jones, J. M.; Shield, I.; Williams, P. T. *Fuel* **2008**, *87*, 844−856.

(7) Deng, J.; Wang, G.; Kuang, J.; Zhang, Y.; Luo, Y. *J. Anal. Appl. Pyrolysis* **2009**, *86*, 331−337.

(8) Prins, M. J.; Ptasinski, K. J.; Janssen, F. J. J. G. *Energy* **2006**, *31*, 3458−3470.

(9) Bridgwater, A. V. *Fuel* **1995**, *74*, 631−653.

(10) Stanmore, B.; Visona, S. *Combust. Flame* **1998**, *113*, 274−276.

(11) Hecht, E. S.; Shaddix, C. R.; Geier, M.; Molina, A.; Haynes, B. S. *Combust. Flame* **2012**, *159*, 3437−3447.

(12) Di Blasi, C. *Prog. Energy Combust. Sci.* **2009**, *35*, 121−140.

(13) Guerrero, M.; Ruiz, M. P.; Alzueta, M. U.; Bilbao, R.; Millera, A. *J. Anal. Appl. Pyrolysis* **2005**, *74*, 307−314.

(14) Fushimi, C.; Araki, K.; Yamaguchi, Y.; Tsutsumi, A. *Ind. Eng. Chem. Res.* **2003**, *42*, 3922−3928.

(15) Cetin, E.; Moghtaderi, B.; Gupta, R.; Wall, T. F. *Fuel* **2004**, *83*, 2139−2150.

(16) Cetin, E.; Gupta, R.; Moghtaderi, B. *Fuel* **2005**, *84*, 1328−1334.

(17) Kurosaki, F.; Ishimaru, K.; Hata, T.; Bronsveld, P.; Kobayashi, E.; Imamura, Y. *Carbon* **2003**, *41*, 3057−3062.

(18) Whitty, K.; Backman, R.; Hupa, M. *Carbon N. Y.* **1998**, *36*, 1683−1692.

(19) Della Rocca, P. A.; Cerrella, E. G.; Bonelli, P. R.; Cukierman, A. L. *Biomass Bioenergy* **1999**, *16*, 79−88.

(20) Okumura, Y.; Hanaoka, T.; Sakanishi, K. *Proc. Combust. Inst.* **2009**, *32*, 2013−2020.

(21) Wornat, M. J.; Hurt, R. H.; Davis, K. a.; Yang, N. Y. C. *Symp. Combust.* **1996**, *26*, 3075−3083.

(22) Borrego, A. G.; Garavaglia, L.; Kalkreuth, W. D. *Int. J. Coal Geol.* **2009**, *77*, 409−415.

(23) Karlström, O.; Brink, A.; Biagini, E.; Hupa, M.; Tognotti, L. *Proc. Combust. Inst.* **2013**, *34*, 2427−2434.

(24) Matsumoto, K.; Takeno, K.; Ichinose, T.; Ogi, T.; Nakanishi, M. *Fuel* **2009**, *88*, 519−527.

(25) Kajitani, S.; Zhang, Y.; Umemoto, S.; Ashizawa, M.; Hara, S. *Energy Fuels* **2010**, *24*, 145−151.

(26) Fermoso, J.; Stevanov, C.; Moghtaderi, B.; Arias, B.; Pevida, C.; Plaza, M. G.; Rubiera, F.; Pis, J. J. *J. Anal. Appl. Pyrolysis* **2009**, *85*, 287−293.

(27) Meesri, C.; Moghtaderi, B. *Combust. Sci. Technol.* **2003**, *175*, 793−823.

(28) Jones, J. M.; Bridgeman, T. G.; Darvell, L. I.; Gudka, B.; Saddawi, A.; Williams, A. *Fuel Process. Technol.* **2012**, *101*, 1−9.

(29) Fisher, E. M.; Dupont, C.; Darvell, L. I.; Commandré, J.-M.; Saddawi, A.; Jones, J. M.; Grateau, M.; Nocquet, T.; Salvador, S. *Bioresour. Technol.* **2012**, *119*, 157−165.

(30) Kobayashi, H.; Howard, J. B.; Sarofim, a. F. *Symp. Combust.* **1977**, *16*, 411−425.

(31) Suzuki, T.; Hirose, R.; Morimoto, K.; Abe, T. *Symp. Combust.* **1985**, *20*, 1419−1425.

(32) Mitchell, R. E.; Hurt, R. H.; Baxter, L. L.; Hardesty, D. R. *Compilation of Sandia Coal Char Combustion Data and Kinetic Analyses, Milestone Report*, SAND92-8208; Sandia National Laboratories: Albuquerque, NM, 1992.

(33) Kim, J. J.; Ahn, D. H.; Gibbs, B. M.; Ko, K. H. Gasification kinetics of an Indonesian sub-bituminous coal-char with CO_2 at elevated pressure. *Fuel* **2001**, *80*, 1651−1658.

(34) Wornat, M. J.; Hurt, R. H.; Yang, N. Y. C.; Headley, T. J. *Combust. Flame* **1995**, *100*, 131−143.

(35) Janse, A. M. C.; Jonge, H. G. De; Prins, W.; van Swaaij, W. P. M. 1998, *5885*, 3909−3918.

(36) Lin, L.; Gustafsson, E.; Strand, M. *Combust. Flame* **2011**, *158*, 1426−1437.

(37) Khalil, R. A.; Bach, Q.; Skreiberg, Ø.; Tran, K. *Energy Fuels* **2013**, *27*, 4760−4769.

(38) Borrego, A. G.; Alvarez, D. *Energy Fuels* **2007**, *21*, 3171−3179.

(39) Lu, L.; Sahajwalla, V.; Harris, D. *Metall. Mater. Trans B* **2001**, *32*, 811−820.

(40) Ulloa, C.; Borrego, A. G.; Helle, S.; Gordon, A. L.; García, X. *Fuel* **2005**, *84*, 247−257.

(41) Hald, P. M. *Ash Tracer Technique*; Forskningscenter Risø: Denmark, 1995.

(42) Sarofim, A. F.; Howard, J. B.; Padia, A. S. *Combust. Sci. Technol.* **1977**, *16*, 187−204.

(43) Froment, K.; Defoort, F.; Bertrand, C.; Seiler, J. M.; Berjonneau, J.; Poirier, J. *Fuel* **2013**, *107*, 269−281.

(44) Thy, P.; Lesher, C. E.; Jenkins, B. M. *Fuel* **2000**, *79*, 693−700.

(45) Thy, P.; Jenkins, B.; Grundvig, S.; Shiraki, R.; Lesher, C. *Fuel* **2006**, *85*, 783−795.

(46) Gale, T. K.; Bartholomew, C. H.; Fletcher, T. H. *Energy Fuels* **1996**, *10*, 766−775.

(47) Pace, R.; Hedman, P.; Smoot, L. *Prepr. Pap. Am. Chem., Div. Fuel Chem.* **1982**, *27*, 167−173.

(48) Murphy, J. J.; Shaddix, C. R. *Combust. Flame* **2006**, *144*, 710−729.

(49) Yeasmin, H.; Mathews, J. F.; Ouyang, S. *Fuel* **1999**, *78*, 11−24.

(50) Gravelsins, R. *Studies of Grinding of Wood and Bark−Wood mixtures With the Szego Mill.* Ph.D. Thesis, University of Toronto, 1998.

(51) Mišljenović, N.; Bach, Q.-V.; Tran, K.-Q.; Salas-Bringas, C.; Skreiberg, Ø. *Energy Fuels* **2014**, *28*, 2554−2561.

(52) Matsumoto, K.; Takeno, K.; Ichinose, T.; Ogi, T.; Nakanishi, M. *Energy Fuels* **2010**, *24*, 1980−1986.

(53) Biagini, E.; Pintus, S.; Tognotti, L. *Proc. Combust. Inst.* **2005**, *30*, 2205−2212.

(54) Tognotti, L.; Biagini, E. *Clean Air Int. J. Energy Clean Environ.* **2005**, *6*, 439−457.

(55) Yuan, S.; Chen, X.; Li, J.; Wang, F. *Energy Fuels* **2011**, *25*, 2314−2321.

(56) Wang, L.; Trninic, M.; Skreiberg, Ø.; Gronli, M.; Considine, R.; Antal, M. J. *Energy Fuels* **2011**, *25*, 3251−3265.

(57) Repellin, V.; Govin, A.; Rolland, M.; Guyonnet, R. *Biomass Bioenergy* **2010**, *34*, 923−930.

(58) Bhatia, S. K.; Perlmutter, D. D. *AIChE J.* **1980**, *26*, 379−386.

(59) Bhatia, S. K.; Perlmutter, D. D. *AIChE J.* **1981**, *27*, 247−254.

(60) Couhert, C.; Salvador, S.; Commandré, J.-M. *Fuel* **2009**, *88*, 2286−2290.

(61) Park, J.; Meng, J.; Lim, K. H.; Rojas, O. J.; Park, S. *J. Anal. Appl. Pyrolysis* **2013**, *100*, 199−206.

(62) Chaiwat, W.; Hasegawa, I.; Kori, J.; Mae, K. *Ind. Eng. Chem. Res.* **2008**, *47*, 5948−5956.

(63) Zheng, A.; Zhao, Z.; Chang, S.; Huang, Z.; Wang, X.; He, F.; Li, H. *Bioresour. Technol.* **2013**, *128*, 370−377.

(64) Jr, P. W.; Matsumoto, S.; Hanzawa, T. *Fuel* **1983**, *62*, 140−149.

(65) Kapteijn, F.; Moulijn, J. *Fuel* **1983**, *62*, 221−225.

(66) Wu, H.; Li, X.; Hayashi, J.; Chiba, T.; Li, C.-Z. *Fuel* **2005**, *84*, 1221−1228.

(67) Li, C.-Z. *Fuel* **2013**, *112*, 609−623.

(68) Elliott, D. C.; Beckman, D.; Bridgwater, A. V.; Diebold, J. P.; Gevert, S. B.; Solantausta, Y. *Energy Fuels* **1991**, *5*, 399−410.

Paper III

Eulerian−Lagrangian Simulation of Biomass Gasification Behavior in a High-Temperature Entrained-Flow Reactor

Xiaoke Ku, Tian Li, Terese Løvås

Energy & Fuels, 28, 5184−5196, 2014

energy&fuels

Article

pubs.acs.org/EF

Eulerian–Lagrangian Simulation of Biomass Gasification Behavior in a High-Temperature Entrained-Flow Reactor

Xiaoke Ku,* Tian Li, and Terese Løvås

Department of Energy and Process Engineering, Norwegian University of Science and Technology (NTNU), 7491 Trondheim, Norway

ABSTRACT: In this paper, a multiscale Eulerian–Lagrangian CFD model based on OpenFOAM has been constructed, which takes into account heat and mass transfer, pyrolysis, homogeneous and heterogeneous reactions, radiation, as well as the interactions between the continuous gas phase and discrete particles. The proposed model is validated and applied to a laboratory-scale biomass entrained-flow reactor. The operating temperatures are high (1000–1400 °C) and influences of five operating parameters (reactor temperature, steam/carbon molar ratio, excess air ratio, biomass type, and particle size) on the gasification behavior are explored. Results show that an increase in the reactor temperature has a positive effect on both the H_2 and CO productions; increasing the steam/carbon ratio increases the H_2 production but decreases the CO production; increasing the excess air ratio decreases both the H_2 and CO productions; the variations in the gas product for the four biomasses studied are not so significant, because of similar biomass nature and, hence, one type can be replaced by another without any major consequences in the gasification performance; and both the CO and H_2 productions and carbon conversion decrease with an increase in particle size. Moreover, the predicted results follow the same trend as the experimental data available in the literature. Quantitative comparisons are also made, and the agreement is good.

1. INTRODUCTION

Biomass is the world's fourth largest energy resource, after coal, oil, and natural gas. There are several methods of utilizing biomass to generate energy among which gasification appears to be more attractive, bceause of its nonoxidation conditions and low pollutant emissions. Biomass gasification is a complex thermochemical process in which biomass is converted to synthetic gas (syngas) under substoichiometric conditions. The syngas could be then used as a fuel in internal combustion engines, gas turbines, or fuel cells for the production of heat, mechanical energy, or power, or as a feedstock for the synthesis of liquid fuels and chemicals. As far as gasification is concerned, the gasifiers can be broadly catalogued into fixed bed,[1] fluidized bed,[2−5] and entrained-flow reactors.[6−8] By virtue of higher syngas yield and low-tar product gas, entrained flow reactors have been widely utilized for coal gasification. However, only a few experimental investigations are published on entrained-flow biomass gasification. For example, Hernández et al.[6] experimentally studied the effect of the addition of steam to air as gasifying agent in biomass entrained-flow gasification and they found that the addition of steam proved positive for the process performance. Qin et al.[8] has experimentally investigated the gasification of two types of biomass, wood, and straw, in a laboratory-scale atmospheric-pressure entrained-flow reactor at low oxygen concentration, and they found that the biomass was completely converted and the syngas contained almost no tar at the highest applied reaction temperature of 1350 °C. Besides the few experimental studies, reported works on computational fluid dynamics (CFD) modeling of biomass gasification in the entrained-flow reactor are not available, to our knowledge.

CFD models are powerful predictive tools in multiphase reacting flow research. Generally, all the CFD models developed can be broadly categorized into Eulerian–Eulerian and Eulerian–Lagrangian approaches. For Eulerian–Eulerian approach, both fluid and particle phases are treated as interpenetrating continua. However, in addition to the difficulty of providing closure models for interphase interaction within its continuum framework, the Eulerian–Eulerian approach does not recognize the discrete character of the particle phase and, thus, has trouble in modeling flows with a distribution of particle types and sizes. These difficulties can be naturally overcome by a Eulerian–Lagrangian approach in which the gas is treated as continuous and the particle is treated as a discrete phase. Each particle is tracked in space and time by directly integrating the equations of motion while accounting for interactions with the continuous phase. An Eulerian–Lagrangian approach has been widely used to simulate coal combustion or gasification in the past decade.[9−17] However, an Eulerian–Lagrangian model of entrained-flow biomass gasification and its validation is not available to our knowledge. In addition, experimental data available for an actual entrained-flow biomass reactor are very limited, because of the challenge related to the required high grindability of the fuel and problems with slagging. Yet, recently, Qin et al.[7] performed such experiments in a high-temperature (1000–1400 °C) laboratory-scale entrained-flow reactor in which biomass particles were injected along with air jets from a central nozzle and steam was injected from the surrounding secondary nozzle hole. They obtained syngas composition measurements at the outlet of the reactor for different operating conditions. Taking into account the literature background, in this paper, we describe the construction of a multiscale Eulerian–Lagrangian CFD model for a high-temperature biomass entrained-flow reactor using the open source code, OpenFOAM

Received: May 9, 2014
Revised: July 8, 2014
Published: July 11, 2014

dx.doi.org/10.1021/ef5010557 | *Energy Fuels* 2014, 28, 5184−5196

(version 2.1.1).[18] All processes of heat and mass transfer, pyrolysis, homogeneous and heterogeneous reactions, radiation, and the interactions between the continuous gas phase and discrete particles have been implemented. Particular emphasis is placed on the effects of five operating parameters (reactor temperature, steam/carbon molar ratio, excess air ratio, biomass type, and particle size) on the gas product composition, syngas yield, particle residence time, and carbon conversion. The predictive capacity and accuracy of the proposed model is also demonstrated by validating the integrated model against a wide range of experimental data of Qin et al.[7]

2. MATHEMATICAL MODELING

The CFD model is formulated using the Eulerian−Lagrangian frame of reference, meaning that transport equations are solved for the continuous gas phase and trajectories of discrete particles are tracked through the calculated gas field. The interaction between the continuous phase and the discrete phase is taken into account by treating the exchange of mass, momentum, and energy between the two phases as source terms in the governing equations.

2.1. Discrete Particle Phase.

The behavior of particles is modeled in a Lagrangian manner. It is assumed that the fuel particles, which consist of a mixture of volatile matter, char, and ash, can be represented as spherical particles with a prescribed size distribution. The particles are also subjected to turbulent dispersion, which is modeled using a stochastic turbulent dispersion model. The governing mass, momentum, and energy equations for particles are as follows:[14,19]

Mass:

$$\frac{dm_i}{dt} = \frac{dm_{\text{vapor}}}{dt} + \frac{dm_{\text{devol}}}{dt} + \frac{dm_{\text{C-O}_2}}{dt} + \frac{dm_{\text{C-CO}_2}}{dt} + \frac{dm_{\text{C-H}_2\text{O}}}{dt} \quad (1)$$

Momentum:

$$\frac{d\mathbf{v}_i}{dt} = \mathbf{f}_{\text{D},i} + \mathbf{g}\left(1 - \frac{\rho_g}{\rho_i}\right) \quad (2)$$

$$\mathbf{f}_{\text{D},i} = \frac{3\mu_g C_D Re_p}{4\rho_i d_i^2}(\mathbf{u}_g - \mathbf{v}_i) \quad (3)$$

$$C_D = \begin{cases} \dfrac{24}{Re_p}\left(1 + \dfrac{1}{6}Re_p^{2/3}\right) & Re_p \le 1000 \\ 0.424 & Re_p > 1000 \end{cases} \quad (4)$$

$$Re_p = \frac{\rho_g d_i |\mathbf{u}_g - \mathbf{v}_i|}{\mu_g} \quad (5)$$

Energy:

$$m_i c_i \frac{dT_i}{dt} = h_i A_{pi}(T_g - T_i) + \frac{\varepsilon_i A_{pi}}{4}(G - 4\sigma T_i^4) - H_{\text{evap}}\, dm_{\text{vapor}} - H_{\text{O}_2/\text{CO}_2/\text{H}_2\text{O}}\, dm_{\text{C-O}_2/\text{CO}_2/\text{H}_2\text{O}} \quad (6)$$

where m_i, $\mathbf{v}_i$, ρ_i, d_i, c_i, T_i, A_{pi}, and ε_i are, respectively, the mass, velocity, density, diameter, specific heat, temperature, external surface area, and emissivity of particle i, and $\mathbf{g}$ is the gravitational acceleration. ρ_g, $\mathbf{u}_g$, μ_g, and T_g are the density, velocity, dynamic viscosity, and temperature of gas, respectively. $\mathbf{f}_{\text{D},i}$, C_D, and Re_p are the drag per unit mass, drag coefficient, and particle Reynolds number. The choice of drag force models has been discussed in an earlier publication.[20] h_i is the interphase thermal transfer coefficient, G is the incident radiation whose initial value is set to zero and its transport equation is solved by a P-1 radiation model. The P-1 model is the approximate of more general P−N model and has generally been chosen for pulverized fuel combustion and gasification for CFD applications.[17] σ is the Stefan−Boltzmann constant, and H is the heat of reaction to evaporate water (latent heat) or one of the three heterogeneous char reactions. dm_{vapor}, dm_{devol}, $dm_{\text{C−O}_2}$, $dm_{\text{C−CO}_2}$, and $dm_{\text{C−H}_2\text{O}}$ are the change in mass of particle i due to loss of water vapor, devolatilization, and char reactions, respectively. As shown in eq 6, the particle temperature is calculated taking into account the heat transfer due to convection, radiation, and source terms, which includes both the latent heat of vaporization of water from the particle to the gas phase and the heat generated by the heterogeneous char reactions.

2.2. Pyrolysis.

The particle phase accounts for fuel conversion via pyrolysis and char consumption. Since the entrained-flow reactor operates at high temperatures, the pyrolysis process occurs at a very fast rate. The pyrolysis compositions released from the fuel can be expressed by the following equilibrium equation and each product yield is solved with the help of the elemental conservation relationships.

$$\text{Biomass} \rightarrow \alpha_1\text{CO} + \alpha_2\text{H}_2\text{O} + \alpha_3\text{CO}_2 + \alpha_4\text{H}_2 + \alpha_5\text{CH}_4 + \alpha_6\text{char}(s) + \alpha_7\text{ash}(s) \qquad \sum_i \alpha_i = 1 \quad (7)$$

Note that, in the present model, CH_4 is the only hydrocarbon species taken into consideration. Although C_2H_2, C_2H_4, C_2H_6, and other higher hydrocarbons (tar) are produced in the pyrolysis process, they are treated as nonstable products and this mechanism has also been widely used by other researchers.[21,22] Soot is also an increasingly important topic in the field of biomass gasification research but the fundamental aspects of soot have been mainly studied by experiments using laboratory-scale reactors. Considering there is no simple soot model that can be easily coupled to a three-dimensional (3D) CFD model, no attempt is made to model soot here. The carbon contained in the fuel, which is not converted to CO, CO_2, and CH_4 in the pyrolysis process, will remain in the solid char, based on eq 7. The heterogeneous reactions, which will be described in more detail in the following subsection, are responsible for the char reactions in the presence of oxygen (O_2), carbon dioxide (CO_2), and steam (H_2O). However, soot will be addressed in the further development of the presented work.

Consistent with Abani and Ghoniem's[9] work, the devolatilization rate is modeled using a single-step first-order Arrhenius reaction:

$$\frac{dm_{\text{devol}}}{dt} = -A \exp\left(-\frac{E}{RT_p}\right) m_{\text{devol}} \quad (8)$$

where m_{devol} is the mass of the volatiles remaining in the particle, $A = 5.0 \times 10^6\ \text{s}^{-1}$, $E = 1.2 \times 10^8$ J/kmol,[23] and T_p is the particle temperature. The devolatilization process is assumed to be energetically neutral because the heat of devolatilization is generally negligible, compared to the heat of reactions due to char consumption and combustion reactions.[9]

2.3. Char Conversion Chemistry.

After devolatilization, the fuel particle is left with char and ash. The ash is assumed to be carried along with the particle, exiting the reactor without taking part in any reactions. Char will react in the presence of oxygen, carbon dioxide, and steam and gets converted to carbon monoxide (CO) and hydrogen (H_2). The following heterogeneous reactions are assumed and implemented in OpenFOAM.

$$\mathrm{C} + 0.5\mathrm{O_2} \rightarrow \mathrm{CO} \tag{R1}$$

$$\mathrm{C} + \mathrm{CO_2} \rightarrow 2\mathrm{CO} \tag{R2}$$

$$\mathrm{C} + \mathrm{H_2O} \rightarrow \mathrm{CO} + \mathrm{H_2} \tag{R3}$$

Reaction R1 is the partial oxidation reaction of char, which is exothermic. Reactions R2 and R3 are endothermic gasification reactions; R2 is known as the Boudouard reaction.

The char consumption rate, which includes the effects of both bulk diffusion and chemical reaction rates, is given as

$$\frac{\mathrm{d}m_{\mathrm{C}\text{-}i}}{\mathrm{d}t} = -A_p p_{i,\mathrm{g}} \frac{r_{\mathrm{diff},i} r_{\mathrm{kin},i}}{r_{\mathrm{diff},i} + r_{\mathrm{kin},i}} \tag{9}$$

$$r_{\mathrm{diff},i} = \frac{C_i[(T_\mathrm{p} + T_\mathrm{g})/2]^{0.75}}{d_\mathrm{p}} \tag{10}$$

$$r_{\mathrm{kin},i} = A_i \exp\left(-\frac{E_i}{RT_\mathrm{p}}\right) \tag{11}$$

where $m_{\mathrm{C}\text{-}i}$ is the mass of the char remaining in the particle when char reacts with gasifying species i (i = O_2, CO_2, or H_2O), A_p is the particle surface area, $p_{i,\mathrm{g}}$ is the partial pressure of the gasifying species in the gas surrounding the particle, and $r_{\mathrm{diff},i}$ and $r_{\mathrm{kin},i}$ are the diffusion rate and the kinetic rate, respectively. T_p and T_g are particle and gas temperatures, respectively, d_p is the particle diameter, and C_i is the mass diffusion rate constant. A_i and E_i are the parameters typical of the Arrhenius forms of kinetic rates. For wood biomass considered in the present study, the constants used for kinetic and diffusion rates are assembled in Table 1.[9,24,25]

Table 1. Heterogeneous Reaction Constants

parameter	value
A_{O_2} (s m^{-1})	2.51×10^{-3}
E_{O_2} (J kmol^{-1})	7.48×10^{7}
A_{H_2O} (s m^{-1})	2.0×10^{-3}
E_{H_2O} (J kmol^{-1})	1.96×10^{8}
A_{CO_2} (s m^{-1})	3.0×10^{-1}
E_{CO_2} (J kmol^{-1})	2.0×10^{8}
C_i (where i = O_2, H_2O, CO_2) (s K$^{-0.75}$)	5.0×10^{-12}

2.4. Continuous Gas Phase.

For continuum gas phase, the governing mass, momentum, energy, and species equations can be typically represented by the following equations:[14,26]

Mass:

$$\frac{\partial \rho_\mathrm{g}}{\partial t} + \nabla\cdot(\rho_\mathrm{g}\mathbf{u}_\mathrm{g}) = S_{\mathrm{p,m}} \tag{12}$$

Momentum:

$$\frac{\partial}{\partial t}(\rho_\mathrm{g}\mathbf{u}_\mathrm{g}) + \nabla\cdot(\rho_\mathrm{g}\mathbf{u}_\mathrm{g}\mathbf{u}_\mathrm{g}) = -\nabla p + \nabla\cdot(\boldsymbol{\tau}_{\mathrm{eff}}) + \rho_\mathrm{g}\mathbf{g} + S_{\mathrm{p,mom}} \tag{13}$$

Energy:

$$\frac{\partial}{\partial t}(\rho_\mathrm{g}E) + \nabla\cdot(\mathbf{u}_\mathrm{g}(\rho_\mathrm{g}E + p)) = \nabla\cdot\alpha_{\mathrm{eff}}\nabla h_\mathrm{s} + S_h + S_{\mathrm{p},h} + S_{\mathrm{rad}} \tag{14}$$

$$E = h_\mathrm{s} - \frac{p}{\rho_g} + \frac{{u_g}^2}{2} \tag{15}$$

Species:

$$\frac{\partial \rho_\mathrm{g} Y_i}{\partial t} + \nabla\cdot(\rho_\mathrm{g}\mathbf{u}_\mathrm{g}Y_i) = \nabla\cdot\rho_\mathrm{g}D_{i,\mathrm{eff}}\nabla Y + S_{\mathrm{p},Y_i} + S_{Y_i} \tag{16}$$

Here, ρ_g, $\mathbf{u}_\mathrm{g}$, p, and h_s are the density, velocity, pressure, and sensible enthalpy of the gas phase, respectively. Y_i is the mass fraction of the ith species in the gas mixture. $S_{\mathrm{p,m}}$, $S_{\mathrm{p,mom}}$, $S_{\mathrm{p},h}$, and S_{p,Y_i} are the source terms that describe interphase exchange terms for mass, momentum, enthalpy, and species. S_h and S_{Y_i} are the source terms due to the homogeneous gas-phase reactions. S_{rad} is the radiation source term. The effective stress tensor ($\boldsymbol{\tau}_{\mathrm{eff}}$) is the sum of the viscous and turbulent stresses and calculated as follows:

$$\boldsymbol{\tau}_{\mathrm{eff}} = -\frac{2}{3}\mu_{\mathrm{eff}}(\nabla\cdot\mathbf{u}_\mathrm{g})\mathbf{I} + \mu_{\mathrm{eff}}((\nabla\mathbf{u}_\mathrm{g}) + (\nabla\mathbf{u}_\mathrm{g})^\mathrm{T}) \tag{17}$$

where μ_{eff} is the effective dynamic viscosity ($\mu_{\mathrm{eff}} = \mu_\mathrm{g} + \mu_\mathrm{t}$). μ_g is the gas phase viscosity, and μ_t is the turbulent viscosity and will be described in more detail below. Similarly, the effective dynamic thermal diffusivity α_{eff} and mass diffusion coefficient for species D_{eff} also take both the viscous and turbulent contributions into account.

$$\alpha_{\mathrm{eff}} = \alpha_\mathrm{g} + \frac{\mu_\mathrm{t}}{Pr_\mathrm{t}} \tag{18}$$

$$D_{\mathrm{eff}} = D_\mathrm{g} + \frac{\mu_\mathrm{t}}{\rho_\mathrm{g} Sc_\mathrm{t}} \tag{19}$$

Here, α_g and D_g are the gas-phase thermal diffusivity and the mass diffusion coefficient for species in the mixture, respectively. As shown by eqs 18 and 19, the turbulent thermal diffusivity and turbulent mass diffusion coefficient are calculated using a turbulent Prandtl number (Pr_t) and a turbulent Schmidt number (Sc_t), respectively. In our model, we assume that $Pr_\mathrm{t} = 1.0$ and $Sc_\mathrm{t} = 1.0$, which are standard values used in OpenFOAM.

There are big variations in the gas velocity within the reactor, because of large temperature gradients and a large amount of gas products from biomass by devolatilization and gasification. Hence, the local Reynolds number (Re) can be very high and turbulence should be taken into account. In order to resolve the turbulence, the governing transport equations for k and ε are solved and it is the most frequently employed turbulence model in CFD studies of gasification.[14]

$$\frac{\partial}{\partial t}(\rho_\mathrm{g}k) + \nabla\cdot(\rho_\mathrm{g}\mathbf{u}_\mathrm{g}k) = \nabla\cdot\left(\left(\mu_\mathrm{g} + \frac{\mu_\mathrm{t}}{\sigma_k}\right)\nabla k\right) + G_k - \rho_\mathrm{g}\varepsilon \tag{20}$$

Table 2. Considered Chemical Reactions and Their Reaction Rates

reaction		reaction rate	refs
$CH_4 + 2O_2 \rightarrow CO_2 + 2H_2O$	(R4)	$k = 5.16 \times 10^{13} T^{-1}[CH_4][O_2] \exp\left(-\frac{1.30 \times 10^8}{RT}\right)$	27
$CH_4 + H_2O \rightarrow CO + 3H_2$	(R5)	$k = 7.0 \times 10^{6}[CH_4][H_2O] \exp\left(-\frac{1.26 \times 10^8}{RT}\right)$	28
$H_2 + 0.5O_2 \rightarrow H_2O$	(R6)	$k = 2.2 \times 10^{9}[H_2][O_2] \exp\left(-\frac{1.09 \times 10^8}{RT}\right)$	27
$CO + 0.5O_2 \rightarrow CO_2$	(R7)	$k = 1.0 \times 10^{10}[CO][O_2]^{0.5}[H_2O]^{0.5} \exp\left(-\frac{1.26 \times 10^8}{RT}\right)$	27
$CO + H_2O \leftrightarrow CO_2 + H_2$	(R8)	$k_f = 2.78 \times 10^{3}[CO][H_2O] \exp\left(-\frac{1.26 \times 10^7}{RT}\right)$ $k_b = 9.59 \times 10^{4}[CO_2][H_2] \exp\left(-\frac{4.66 \times 10^7}{RT}\right)$ $k_{eq} = 0.029 \exp\left(\frac{3.40 \times 10^7}{RT}\right)$	27

$$\frac{\partial}{\partial t}(\rho_g \varepsilon) + \nabla \cdot (\rho_g \mathbf{u}_g \varepsilon) = \nabla \cdot \left(\left(\mu_g + \frac{\mu_t}{\sigma_\varepsilon} \right) \nabla \varepsilon \right) + \frac{\varepsilon}{k}(C_{\varepsilon 1} G_k - C_{\varepsilon 2} \rho_g \varepsilon) \tag{21}$$

Here, k is the turbulent kinetic energy, ε is the dissipation rate of turbulent kinetic energy, and G_k represents the generation term for k. The parameters $C_{\varepsilon 1}$, $C_{\varepsilon 2}$, σ_k, and σ_ε are constants ($C_{\varepsilon 1}$ = 1.44, $C_{\varepsilon 2}$ = 1.92, σ_k = 1.0, and σ_ε = 1.3). μ_t is the gas-phase turbulent viscosity, which is computed as a function of k and ε:

$$\mu_t = \rho_g C_\mu \left(\frac{k^2}{\varepsilon} \right) \tag{22}$$

where C_μ is a constant, which is set as 0.09 as standard.

2.5. Gas-Phase Reactions. Simple global reactions are used to describe the gas-phase chemistry and the effect of turbulence on combustion and gasification is resolved by the partially stirred reactor (PaSR) model.[9] Chemical reaction equations and their kinetic constants, as well as adopted references, are shown in Table 2. Reactions R4 and R5 are the consumption of CH_4 through oxidation and steam reactions. Reactions R6 and R7 are H_2 and CO consumption reactions. Reaction R8 is known as the reversible water–gas shift reaction, and the forward reaction rate k_f and backward reaction rate k_b are related by the equilibrium constant $k_{eq} = k_f/k_b$.

2.6. Computational Methodology. Since the governing equations for particles and the gas phase are different, different solution schemes must be used. For discrete particles, a first-order Euler time integration scheme is used to solve the particle motions. Meanwhile, the drying, pyrolysis, and gasification submodels update particle properties such as temperature, composition, and heat capacity at each fluid time step. For continuous gas phase, time discretization of the transporting equations is based on an Euler scheme and spatial discretization uses a finite-volume technique. The coupling between the discrete particles and the gas phase is achieved by the interphase source terms ($S_{p,m}$, $S_{p,mom}$, $S_{p,h}$, S_{p,Y_i}), which are solved at every fluid time step. All mathematical models and schemes described above have been developed and implemented into an open source C++ toolbox OpenFOAM (OpenCFD, Ltd., 2012).

3. SIMULATION SETUP

The simulations are performed on the Technical University of Denmark (DTU) laboratory-scale entrained-flow reactor, which operates at atmospheric pressure, with a length of 202 cm and a diameter of 8 cm. A schematic of experimental setup is shown in Figure 1, and a more-detailed description of the experimental facility can be found in the literature.[7] Here, the reaction tube is constructed and meshed using OpenFOAM preprocessing utility. A three-dimensional structured grid consisting of 281 280 cells is employed to define the total volume and is depicted in Figure 2a. The mesh is locally refined in the center injection zone in order to enhance the prediction of the devolatilization and initial combustion steps of the fuel particles. Figure 2b shows the top view of the reactor inlet, which consists of a center inlet and a concentric ring inlet. Four common biomasses in Europe[2,7] are used as the fuel, and their properties, such as proximate and elemental analyses, are summarized in Table 3. The

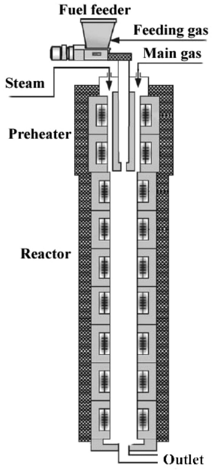

Figure 1. Schematic of experimental setup.[7]

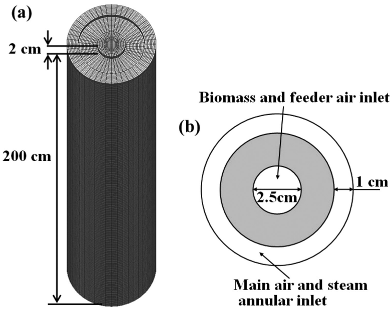

Figure 2. (a) Three-dimensional (3D) computational mesh for the DTU laboratory-scale entrained-flow reactor and (b) the top view of the reactor inlet.

Table 3. Biomass Properties

	beech	pine	holm oak	eucalyptus
	Proximate Analysis (wt %, as-received basis)			
moisture	9.04	12.0	9.5	10.6
ash	0.61	0.5	2.5	0.7
volatile	76.70	71.5	70.2	74.8
fixed carbon	13.65	16.0	17.8	13.9
	Elemental Analysis (wt %, daf basis)			
C	49.9	51.6	51.1	52.8
H	6.4	4.9	5.3	6.4
O	43.6	42.6	42.7	40.4
other	0.1	0.9	0.9	0.4

compositions of volatiles for the four biomasses, which are shown in Table 4, are determined by the equilibrium equation (eq 7) and the elemental conservation relationships. The volatiles are a mixture of H_2, CO, CO_2, and CH_4. Because of the high temperatures encountered in the entrained-flow reactor, the volatiles release at a very fast rate, which is calculated from eq 8. When the compositions of volatiles are released from the fuel particles, their combustion and gasification are naturally taken into account by the homogeneous reactions listed in Table 2.

Table 4. Composition of Volatile Matter for the Four Biomasses

	Mass Fraction (%)			
component	beech	pine	holm oak	eucalyptus
CH_4	18.2	17.8	14.8	24.6
H_2	2.9	1.5	3.0	1.5
CO_2	41.4	42.4	43.8	37.5
CO	37.5	38.3	38.4	36.4

The grid resolution employed here has been determined using a corresponding grid independence study. To seek a proper grid system, four different grid systems of 70 320 cells, 140 640 cells, 281 280 cells, and 351 600 cells are tested. In the test, only air (293 K) with the uniform inlet velocity (U_0) is injected into the reactor. Figure 3 displays the U_z velocity distribution in the midplane and at the bottom exit of the reactor. It can be seen that the velocity profiles in terms of the third and fourth grid systems coincide with the analytic solution. This implies that the third grid system of 281 280 cells can satisfy the requirement of grid independence. Note that for turbulent multiphase reacting flows, the choice of grid size is somewhat not straightforward. In 2012, Kumar and Ghoniem[14] concluded that it became increasingly difficult to determine a steady-state solution for a very finer mesh, because of the inherently transient problem of turbulent multiphase reacting flows in gasifiers and the stochastic nature of the particle turbulent dispersion model. Therefore, the grid system of 281 280 cells is a good choice that takes both the grid independence and steady-state solution into account.

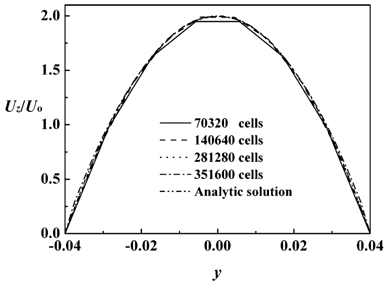

Figure 3. Velocity distribution (U_z) in the midplane and at the bottom exit of the reactor when only air with the uniform inlet velocity U_0 is sent into the reactor.

Biomass is fed into the reactor from the center inlet by the cold feeder air stream (10 NL/min). Both the biomass and feeder air temperatures are 300 K. The preheated air and steam, whose temperatures are equal to the operating temperature, are blown into the reactor from the outer ring inlet. The fuel particles are injected using a stochastic technique and at a rate of 50 000 particles per second. Four mean particle diameters ($\bar{d}_p$ = 200, 310, 500, 750 μm) are employed to study the effect of particle size and the initial particle size distributions follow the Rossin–Rammler distribution, which are shown in Figure 4. The particle size distributions are the same for all the biomasses studied. Initially, a pure nitrogen environment within the reactor is adopted, i.e., at the start of simulation ($t = 0$), there is only one species (N_2) in the reactor. The operation conditions are established using measurements made during the experimental runs[7] and the detailed test cases are listed in Table 5. As shown in Table 5, besides 27 gasification cases, we have also tested three pyrolysis cases.

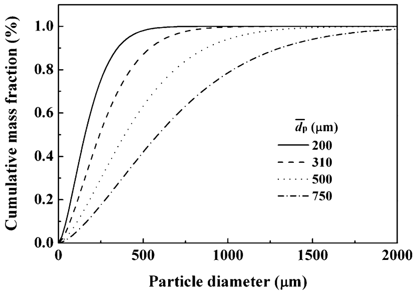

Figure 4. Biomass particle size distributions.

4. RESULTS AND DISCUSSION

In the following subsections, the productions of the main gas product components (H_2, CO, CO_2, and CH_4, expressed in Nm^3

Table 5. Test Cases

parameter	case	T_r (°C)	S/C	λ	fuel	$\bar{d}_p$ (μm)	fuel feeding rate (g/min)	particle residence time (s)	air/steam flow rates through outer ring inlet (g/min)
						Pyrolysis Cases			
steam/carbon molar ratio, S/C	P1	1400	0	0	beech	310	12.8	2.27	0/0
steam/carbon molar ratio, S/C	P2	1400	0.5	0	beech	310	12.8	1.82	0/4.3
steam/carbon molar ratio, S/C	P3	1400	1.0	0	beech	310	12.8	1.53	0/8.6
						Gasification Cases			
reactor temperature, T_r	G1	1000	0.5	0.3	beech	310	12.8	2.55	6.9/4.3
reactor temperature, T_r	G2	1100	0.5	0.3	beech	310	12.8	2.27	6.9/4.3
reactor temperature, T_r	G3	1200	0.5	0.3	beech	310	12.8	2.03	6.9/4.3
reactor temperature, T_r	G4	1300	0.5	0.3	beech	310	12.8	1.80	6.9/4.3
reactor temperature, T_r	G5	1400	0.5	0.3	beech	310	12.8	1.63	6.9/4.3
steam/carbon molar ratio, S/C	G6	1400	0	0.3	beech	310	12.8	1.94	6.9/0
steam/carbon molar ratio, S/C	G7[a]	1400	0.5	0.3	beech	310	12.8	1.63	6.9/4.3
steam/carbon molar ratio, S/C	G8	1400	1.0	0.3	beech	310	12.8	1.42	6.9/8.6
excess air ratio, λ	G9	1400	0.5	0.25	beech	310	15.3	1.48	6.9/5.2
excess air ratio, λ	G10[a]	1400	0.5	0.3	beech	310	12.8	1.63	6.9/4.3
excess air ratio, λ	G11	1400	0.5	0.35	beech	310	10.9	1.76	6.9/3.7
fuel	G12[a]	1400	0.5	0.3	beech	310	12.8	1.63	6.9/4.3
fuel	G13	1400	0.5	0.3	pine	310	12.8	1.82	7.1/4.4
fuel	G14	1400	0.5	0.3	holm oak	310	12.8	1.70	7.5/4.4
fuel	G15	1400	0.5	0.3	eucalyptus	310	12.8	1.59	7.9/4.5
mean particle size, $\bar{d}_p$	G16	1400	0.5	0.3	beech	200	12.8	1.67	6.9/4.3
mean particle size, $\bar{d}_p$	G17	1400	0.5	0.3	pine	200	12.8	1.98	7.1/4.4
mean particle size, $\bar{d}_p$	G18	1400	0.5	0.3	holm oak	200	12.8	1.76	7.5/4.4
mean particle size, $\bar{d}_p$	G19	1400	0.5	0.3	eucalyptus	200	12.8	1.64	7.9/4.5
mean particle size, $\bar{d}_p$	G20	1400	0.5	0.3	beech	500	12.8	1.58	6.9/4.3
mean particle size, $\bar{d}_p$	G21	1400	0.5	0.3	pine	500	12.8	1.72	7.1/4.4
mean particle size, $\bar{d}_p$	G22	1400	0.5	0.3	holm oak	500	12.8	1.65	7.5/4.4
mean particle size, $\bar{d}_p$	G23	1400	0.5	0.3	eucalyptus	500	12.8	1.56	7.9/4.5
mean particle size, $\bar{d}_p$	G24	1400	0.5	0.3	beech	750	12.8	1.56	6.9/4.3
mean particle size, $\bar{d}_p$	G25	1400	0.5	0.3	pine	750	12.8	1.68	7.1/4.4
mean particle size, $\bar{d}_p$	G26	1400	0.5	0.3	holm oak	750	12.8	1.61	7.5/4.4
mean particle size, $\bar{d}_p$	G27	1400	0.5	0.3	eucalyptus	750	12.8	1.54	7.9/4.5

[a] Cases G7, G10, and G12 are the same as case G5.

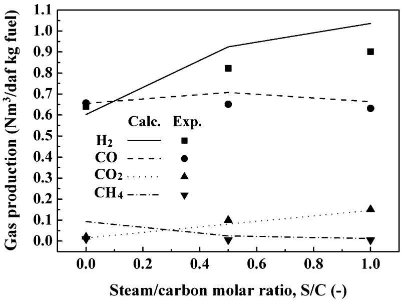

Figure 5. Species production in the product gas as a function of steam/carbon molar ratio (S/C) for pyrolysis cases (cases P1−P3 in Table 5).

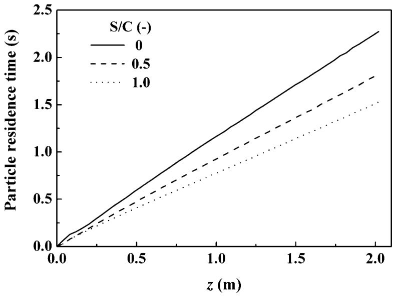

Figure 6. Average particle residence time along the reactor length at different steam/carbon molar ratio (S/C) for pyrolysis cases (cases P1−P3 in Table 5).

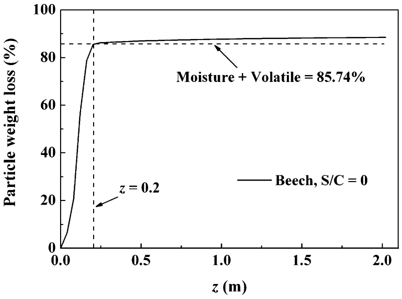

Figure 7. Average particle weight loss along the reactor length for the pyrolysis case (case P1 in Table 5).

of gas component produced per kg of dry and ash-free fuel) is used to explore the effects of different operating conditions on pyrolysis and gasification performances. The gas production can provide valuable information on the overall gasification process, since it takes into account both the gas quality and the fuel conversion.

4.1. Pyrolysis. Compared to coal, biomass typically has a much higher volatile matter content. For the four biomasses studied, the volatile content is more than 70% (see Table 3). Therefore, the pyrolysis process is more important for biomass than coal. In this subsection, we first validate our integrated CFD model by testing three pyrolysis cases. The corresponding experimental runs are conducted by Qin et al.[7] For pyrolysis cases, N_2 (at a flow rate of 10 NL/min) is employed as the feeder gas, which is different from the 10 NL/min air stream used for gasification cases.

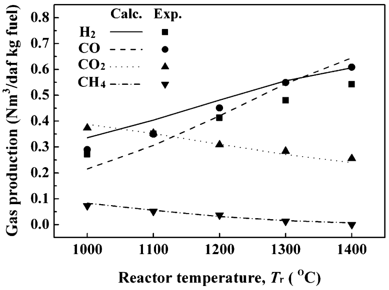

Figure 9. Species production as a function of reactor temperature T_r (cases G1−G5 in Table 5).

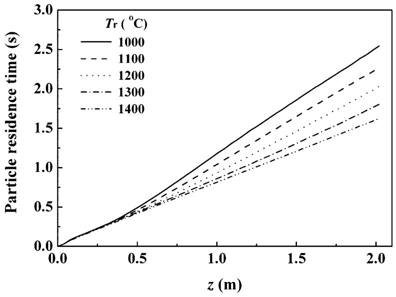

Figure 10. Average particle residence time along the reactor length at different reactor temperatures T_r (cases G1−G5 in Table 5).

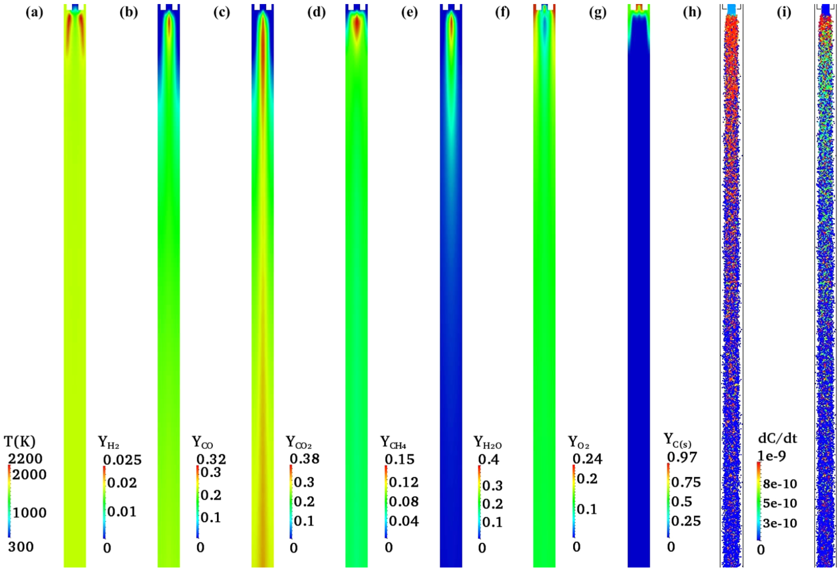

Figure 8. (a) Temperature distribution, (b-g) predictions of species mass fraction distribution in a plane passing through the axis of the reactor at $t = 10$ s, (h) beech wood particle distribution (colored based on the concentration of the mass fraction of char), and (i) char burnout rate (kg/s) (case G5 in Table 5).

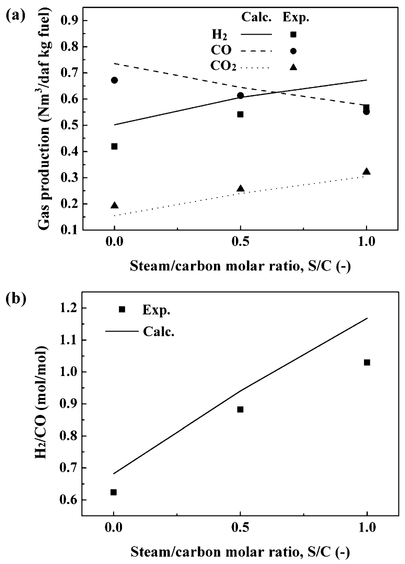

Figure 11. (a) Species production and (b) H_2/CO molar ratio in the product gas, each as a function of the steam/carbon molar ratio (S/C) (cases G6−G8 in Table 5).

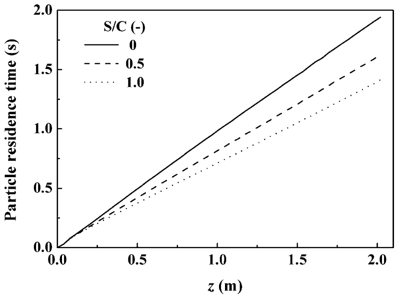

Figure 12. Average particle residence time along the reactor length for different steam/carbon molar ratio (S/C) (cases G6−G8 in Table 5).

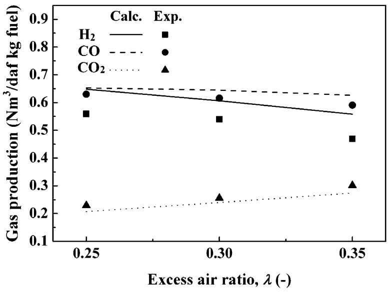

Figure 13. Species production as a function of excess air ratio λ (cases G9−G11 in Table 5).

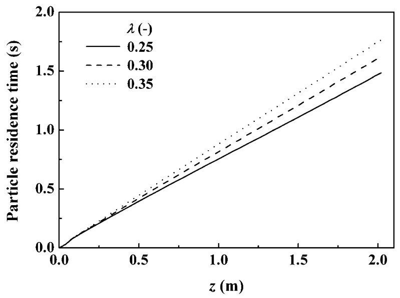

Figure 14. Average particle residence time along the reactor length for different excess air ratio (λ) values (cases G9−G11 in Table 5).

Figure 5 shows the species production in the product gas for the three pyrolysis cases (cases P1−P3 in Table 5), and the predicted results are compared with experimental data reported by Qin et al.[7] The lines represent the numerically calculated results, whereas the corresponding symbols represent the experimental data. Note that the hydrocarbon production in the experimental work of Qin et al.[7] are joined together as CH_4. It can be seen that the predictions of the model show good conformance to the experimental measurements. For H_2, the minimum relative error of calculation to experiment is ~5% and the maximum relative error is <15%. For CO, the minimum relative error is ~1% and the maximum relative error is <9%. For CO_2, the minimum relative error is ~3% and the maximum relative error is within 22%. The errors of CH_4 are somewhat large, which might be related to its small amounts which can easily cause big errors. However, considering the simple single-step first-order Arrhenius reaction equation (eq 8) used for modeling the pyrolysis process in our CFD model, the match between our predictions and experimental results of Qin et al.[7] can be considered to be encouraging.

Figure 6 shows the predicted average particle residence time along the reactor length for the three pyrolysis cases (cases P1−P3 in Table 5). It is observed that a higher S/C ratio results in a shorter particle residence time inside the reactor. This is reasonable since the steam flow rate increases as the S/C ratio increases, causing a decrease in the particle residence time. In addition, the particle residence times at the outlet of the reactor are summarized in Table 5.

Figure 7 depicts the average particle weight loss along the reactor length for case P1. It is easily seen that the volatiles release at a very fast rate and the devolatilization is finished just downstream from the inlet (z = 0.2). Moreover, from Figure 6, we can extract that, at z = 0.2, the predicted particle residence time for case P1 is 0.16 s.

The above subsection has shown the validity of the integrated CFD model by comparing our simulated results for pyrolysis cases with the experimental data obtained from the literature.[7] In the following, the proposed model is further validated by testing a wide range of gasification cases.

4.2. Gasification Phenomena.

Some qualitative results are first presented. Figure 8a shows the predicted temperature contours in the midplane of the reactor at T_r = 1400 °C, S/C = 0.5, and λ = 0.3 for beech wood (case G5 in Table 5). It is clearly observed that the peak temperature (~2200 K) exists away from the axis, in a region just following the fuel injection. The sharp temperature increase near the injector is due to the exothermic combustion of volatiles, because more than 75% of the beech wood injected is devolatilized and transported radially outward from the cold central jet, along with the conveyance air fed from

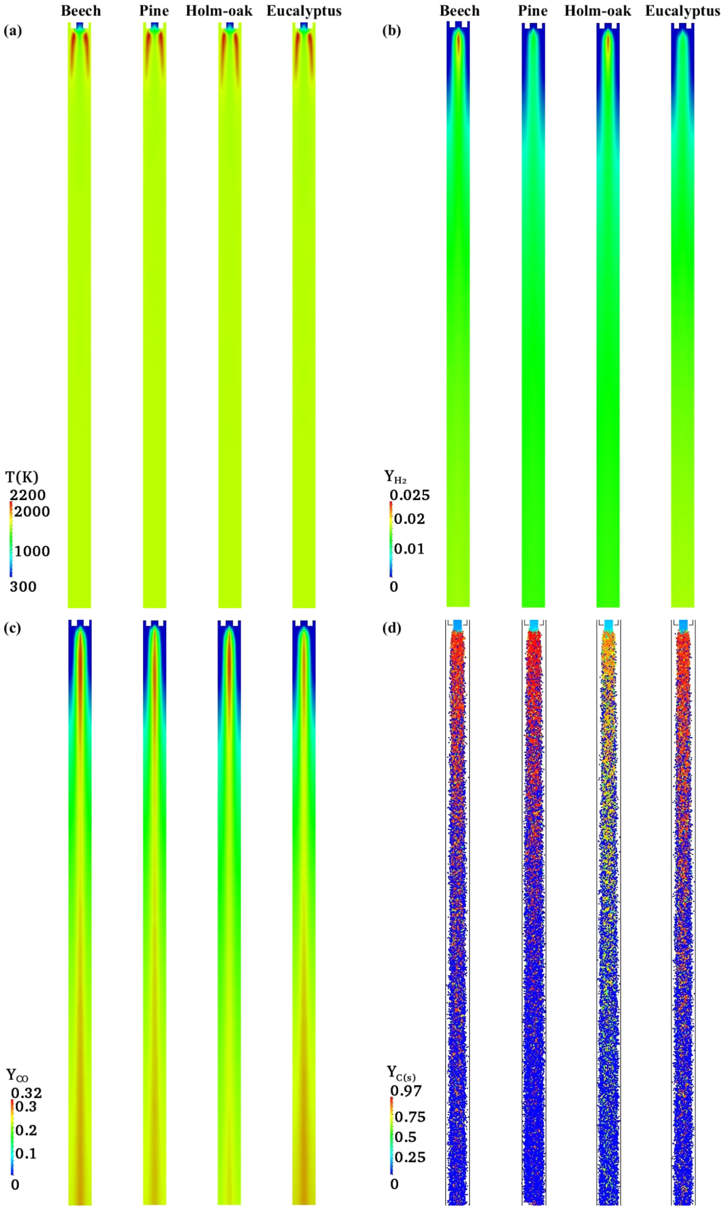

Figure 15. (a) Temperature distributions, mass fraction distributions of (b) H_2, (c) CO in a plane passing through the axis of the reactor, and (d) fuel particle distributions (colored based on the concentration of mass fraction of char) at t = 10 s for four biomasses (cases G12−G15 in Table 5).

the inlets. This is typical of jet diffusion flames.[9] Further downstream, the temperature distribution is almost homogeneous and gasification reactions are dominant. Figure 8b−g present the concentration (mass fraction) contours of gas phase species in a plane passing through the axis of the reactor. A higher concentration of H_2, CO, CO_2, and CH_4 in the upstream region can be explained by the volatile matter content of wood, which releases high amount of volatiles during devolatilization. Figure 8g demonstrates that the oxygen is quickly consumed during the combustion of volatiles. Downstream, CO and H_2 concentrations are higher and CO_2 and H_2O concentrations are lower, which are attributed to the char gasification reactions. Figure 8h shows the biomass particle distribution colored according to the char concentration (mass fraction) remaining in the particle. It

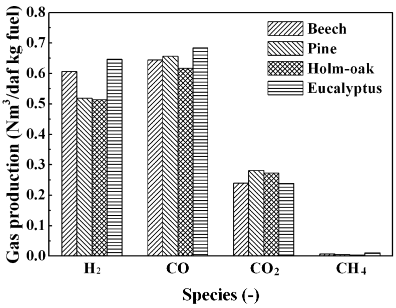

Figure 16. Species production at the reactor exit for different biomasses (cases G12−G15 in Table 5).

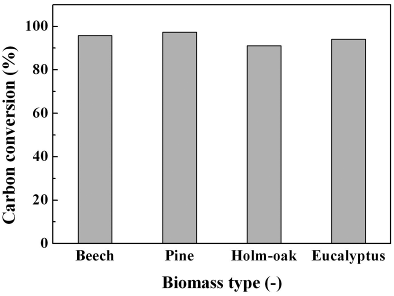

Figure 17. Carbon conversion at the reactor exit for different biomasses (cases G12−G15 in Table 5).

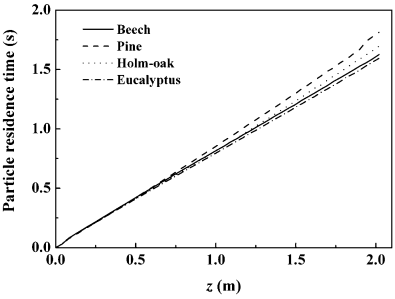

Figure 18. Average particle residence time along the reactor length for different biomasses (cases G12−G15 in Table 5).

can be seen that, just downstream from the inlet, the particle has some volatiles left and, hence, the mass fraction of char is low (blue color). After a fast devolatilization, the particles have higher char concentration (red color), because there are only char and ash left. Further downstream, the char gets consumed and most of the particles have a low concentration of char (blue color), because they are left with only ash. Figure 8i plots the corresponding char burnout rate of each particle. It can be observed that, just downstream from the inlet, the char burning rate is high, because of the existence of oxygen in this location. Further downstream, most of the particles are gone, with only ash remaining, as shown in Figure 8h; therefore, they have zero char burnout rate. The predicted char conversion from simulation for

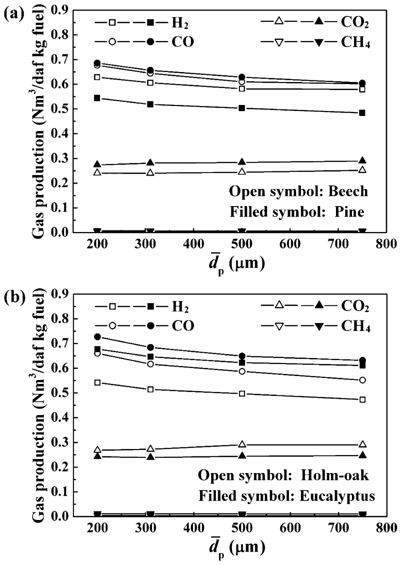

Figure 19. Species production as a function of mean particle diameter $\overline{d}_p$ (cases G12−G27 in Table 5): (a) beech and pine, and (b) holm oak and eucalyptus.

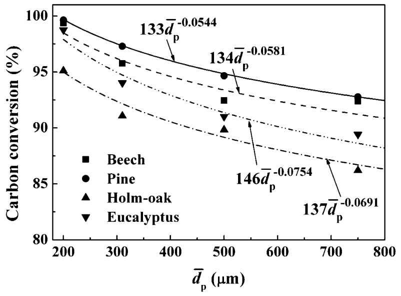

Figure 20. Carbon conversion as a function of mean particle diameter $\overline{d}_p$ (cases G12−G27 in Table 5).

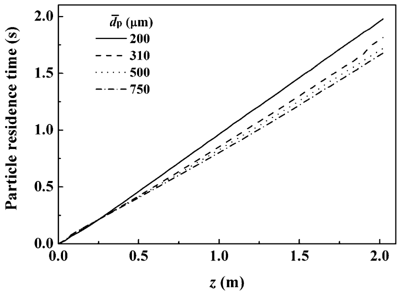

Figure 21. Average particle residence time along the reactor length at different mean particle diameter $\overline{d}_p$ for pine (cases G13, G17, G21, and G25 in Table 5).

this case is 95.8%, which is in good agreement with the measured value of ∼93% that has been reported by Qin et al.[7]

4.3. Effect of Reactor Temperature.

In this subsection the effect of the reactor temperature on the species production and particle residence time is studied. The reactor temperature (T_r, defined as the external temperature of the reactor tube) ranges from 1000 °C to 1400 °C with otherwise fixed operating parameters (cases G1−G5 in Table 5). Figure 9 compares the predicted results with experimental data reported by Qin et al.[7] Again, the predictions of the model show good conformance to the experimental measurements. For the two most important syngas species (H_2, CO), the minimum relative error of calculation to experiment is ∼1% and the maximum relative error is <25%. For CO_2, the minimum relative error is ∼0.5% and the maximum relative error is <6%. For CH_4, the maximum relative error is also within 19%. The overestimation of H_2 can probably be attributed to the neglect of tar and methanation reaction.

Figure 10 shows the predicted average particle residence time along the reactor length for different reactor temperatures. It is easily seen that an increase in T_r will decrease the particle residence time inside the reactor, and this trend is qualitatively consistent with the experimental findings of Qin et al.[7] However, here, we will not attempt to quantitatively compare our predicted particle residence times with those of Qin et al.[7] The particle residence times of our simulation are directly calculated from the residence time of each particle, whereas the particle residence times of Qin et al.[7] were approximately estimated by the gas mean residence time, assuming that there was no relative velocity between the solid phase and the gas phase. This, strictly speaking, is not necessarily the case and new advanced experimental techniques are needed in order to accurately measure the particle residence time, in comparison to the CFD.

Both the reactor temperature and the particle residence time have important roles for the reaction progress. Although the particle residence time is shorter at higher reactor temperatures, as shown in Figure 10, the reactor temperature has a more significant effect on the increase in the reaction rate. This means that, within the T_r range studied (1000−1400 °C), the increase in the reactor temperature is dominant for determining the gas composition. As shown in Figure 9, rising temperature leads to a substantial increase in the H_2 and CO productions, which are due to two reasons: (i) the production of H_2 and CO through the endothermic char gasification reactions (reactions R2 and R3), which are favorable at elevated temperatures, and (ii) the increase of H_2 and CO yield resulting from the steam reforming of CH_4 (reaction R5). Simultaneously, the CO_2 production monotonically decreases with increasing temperature, because of its consumption via Boudouard reaction (reaction R2, promoted at higher temperatures), and the CH_4 yield also declines steadily with the rise in temperature and nearly vanishes at 1400 °C due to the steam reforming reaction (reaction R5).

4.4. Effect of Steam/Carbon Molar Ratio.

In this subsection, the effect of the steam/carbon molar ratio (denoted as S/C) on species production and particle residence time is explored. Accordingly, three different cases (cases G6−G8 in Table 5) where the S/C ratio varies from 0 to 1.0, while the other operating parameters remain otherwise fixed, are tested. Figure 11a shows the production of the main components in the product gas as a function of S/C ratio. Note that the yield of CH_4 is fairly low, in contrast to the other species at $T = 1400$ °C (see Figure 9), so that it is not shown in this figure. Again, the calculated results show good agreement with the experimental measurements. For H_2 and CO, the minimum relative error of calculation to experiment is ∼4% and the maximum relative error is <19%. For CO_2, the minimum relative error is ∼5% and the maximum relative error is also within 19%. It can be also easily observed that the H_2 and CO_2 productions increase steadily while the CO yield decreases almost linearly by increasing the S/C value. These results can be explained mainly by the water−gas shift reaction (reaction R8), which transforms CO and steam to H_2 and CO_2. As the S/C ratio increases, the partial pressure of steam and the steam flow rate increases. This means that the rate of the water−gas shift reaction (reaction R8) increases. Figure 11b plots the H_2/CO molar ratio in the product gas as a function of S/C ratio. The increase in H_2/CO ratio, from ∼0.7 (S/C = 0) to ∼1.1 (S/C = 1) confirms the promotion of the water−gas shift reaction, because of the increase in the amount of steam available to get involved in the reaction.

Figure 12 shows the predicted average particle residence time along the reactor length for different S/C ratios. As expected, an increase in S/C will decrease the particle residence time inside the reactor since S/C is controlled by the steam flow rate, which increases with the S/C value. For the narrow S/C range studied (0−1.0), increasing the reaction rate of water−gas shift reaction (reaction R8) has a more significant effect than decreasing the particle residence time.

4.5. Effect of Excess Air Ratio.

The excess air ratio (λ) is the ratio of net air input in the reactor to the amount of stoichiometric air needed for complete combustion of the fuel. λ could be varied either by changing the fuel feeding flow rate while keeping the air flow constant or vice versa. In this subsection, the total inlet air rate is kept constant and the applied excess air ratio is increased from 0.25 to 0.35 by reducing the fuel feeding rate while keeping the other operating parameters otherwise fixed (cases G9−G11 in Table 5). Figure 13 presents the effect of λ on the species production. For H_2 and CO, the minimum relative error of calculation to experiment is ∼3% and the maximum relative error is <18%. For CO_2, the maximum relative error is within 9%. It is also found that increasing λ clearly decreases the H_2 and CO productions but increases the CO_2 production. These trends are most likely because of more oxidizing conditions at the higher excess air ratio, leading to oxidation of H_2 and CO (see reactions R6 and R7).

Figure 14 shows the predicted average particle residence time along the reactor length for different excess air ratios λ. It is observed that an increase in λ will increase the particle residence time inside the reactor, and this trend is also qualitatively consistent with the experimental findings of Qin et al.[7]

The above subsections have demonstrated the validity of the integrated CFD model by comparing our simulated results for both pyrolysis and gasification cases with the wide range of experimental data of Qin et al.[7] In the following, in order to further demonstrate the *predictive* capacity of the proposed model, the calculated results are used to explore the effects of biomass type and particle size on gasification performance for which we have not been able to find suitable experimental data.

4.6. Effect of Biomass Type.

Four common biomasses in Europe (beech, pine, holm oak, eucalyptus) are adopted to explore the effect of biomass type on gasification behavior (cases G12−G15 in Table 5). Beech, holm oak, and eucalyptus are hardwoods, while pine is a softwood. Figure 15 shows the predicted temperature contours, mass fraction distributions of H_2 and CO in the midplane of the reactor, and fuel particle distributions (colored according to the char concentration remaining in the particle) for the four biomasses. It is seen that, regardless of which biomass is consumed, the peak temperature (~2200 K) always exists away from the axis, in a region just following the fuel injection (Figure 15a). The sharp temperature increase near the injector is due to the exothermic combustion of volatiles. At the exit, the concentrations of H_2 from the gasification of beech and eucalyptus are relatively higher, whereas the concentration of CO from the gasification of holm oak is the lowest (Figures 15b and 15c). Figure 15 overally indicates that the gasification phenomenon is qualitatively similar for the four biomasses, and there is no significant difference in the contours, which can be attributed to their similar properties, as shown in Table 3 (high volatile matter, low ash, and high oxygen).

Figure 16 presents the species production at the reactor exit for the four biomasses. It is observed that, although the beech and eucalyptus exhibit higher H_2 production and the holm oak gets a lowest CO production, the four biomasses generally provide quite similar gasification performances, with little difference in the species productions. This finding is qualitatively consistent with the results of previous experimental studies.[2,7] Therefore, one biomass can be replaced by another without any major consequences in the process performance. This is advantageous, because the availability of biomass fuel is very seasonal.

Carbon conversion (CC) is another vital index that is used to evaluate the performance of gasification. It is defined as follows:[29]

$$\mathrm{CC}\ (\%) = \frac{\dot{m}_{\mathrm{out,CO}}\left(\frac{12}{28}\right) + \dot{m}_{\mathrm{out,CO_2}}\left(\frac{12}{44}\right) + \dot{m}_{\mathrm{out,CH_4}}\left(\frac{12}{16}\right)}{\dot{m}_{\mathrm{in,fuel}} Y_{\mathrm{C}}} \times 100 \tag{23}$$

where Y_C is the mass fraction of carbon in the feed fuel.

Figure 17 shows the predicted CC at the reactor exit for the four biomasses. Specifically, the values of CC for the beech, pine, holm oak, and eucalyptus are 95.8%, 97.3%, 91.1%, and 94.0%, respectively, revealing that over 90% of the carbon in these fuels is converted to CO, CO_2, and CH_4, because of high operating temperature (1400 °C). Figure 18 depicts the predicted average particle residence time along the reactor length for different biomasses. As expected, the pine (softwood) has the longest residence time, because of its lower density, compared to other biomasses (hardwood), which is probably why pine has the highest carbon conversion (97.3%).

4.7. Effect of Particle Size. Four mean particle diameters ($\bar{d}_p$ = 200, 310, 500, 750 μm) are employed to study the effect of particle size on the species production and carbon conversion (cases G12−G27 in Table 5). Figure 19 shows the effect of $\bar{d}_p$ on exit species production for the four biomasses. Overall, the predicted CO and H_2 productions decrease as $\bar{d}_p$ increases, so a smaller particle is conducive to the formation of CO and H_2. It is also found that increasing $\bar{d}_p$ leads to very little change in the production of CO_2.

The relationship between the carbon conversion and $\bar{d}_p$ is drawn in Figure 20. The symbols represent the 16 simulation cases (cases G12−G27 in Table 5), and the lines almost threading the symbols represent the corresponding fit curves. As indicated, CC decreases as $\bar{d}_p$ increases for all of the biomasses studied. In order to explore the possible reasons, Figure 21 depicts the predicted average particle residence time along the reactor length at different $\bar{d}_p$ for pine (cases G13, G17, G21, and G25 in Table 5). It is easily observed that smaller particles have a relatively longer residence time, compared to bigger particles, and this trend is same for all four biomasses. This is reasonable because bigger particles have larger inertia and tend to locate near the central fuel jet region. Meanwhile, smaller particles could be easily transported radially toward the walls, where the velocity of the carrier gas is lower, causing smaller particles to have a longer residence time.

In examining the fit curves shown in Figure 20, the carbon conversions for the beech, pine, holm oak, and eucalyptus decreases as the −0.0581, −0.0544, −0.0691, and −0.0754 power of increasing $\bar{d}_p$, respectively. Note that carbon conversion is accomplished by devolatilization and char heterogeneous reactions in the reactor. The devolatilization of biomass is assumed to be independent of particle diameter (see eq 8). The char heterogeneous reactions at high temperature are thought to be inversely proportional to particle diameter for bulk diffusion control.[11] The predicted particle diameter dependences (−0.0581, −0.0544, −0.0691, and −0.0754 powers) fall between the limits for diffusion-controlled heterogeneous reaction (−1 power) and devolatilization (0 power). They are larger than the reported value of −0.145 found by Chen et al.[11] for an entrained-flow coal gasifier, because of a much higher volatile matter content of biomass, compared to coal.

5. CONCLUSION

A multiscale Eulerian−Lagrangian computational fluid dynamics (CFD) model based on OpenFOAM has been constructed, validated, and applied to a laboratory-scale biomass entrained-flow reactor. The operating temperatures are high (1000−1400 °C) and effects of five operating parameters (reactor temperature, steam/carbon molar ratio, excess air ratio, biomass type, and particle size) on the species production, particle residence time and carbon conversion are particularly addressed. Results show that the reactor temperature has a positive effect on the quality of the product gas and rising temperature leads to a substantial increase in the H_2 and CO productions; increasing the steam/carbon ratio increases the H_2 production but decreases the CO production; increasing the excess air ratio decreases both the H_2 and CO productions; the biomass type appears to have influence on the gasification behavior to some extent, because it results in variations in species production and carbon conversion. However, the variations are not so significant, because of similar biomass nature; hence, one type can be replaced by another without any major consequences in the gasification performance. Both the CO and H_2 productions and carbon conversion decrease with an increase in particle size for all of the biomasses. Moreover, the predicted results follow the same trends as the wide range of experimental data for both pyrolysis and gasification experiments obtained from the literature.[7] Quantitative comparisons are also made and the agreement is good. Therefore, the established numerical models and chemical kinetics are suitable for simulating wood gasification in high-temperature entrained-flow reactor.

■ AUTHOR INFORMATION

Corresponding Author

*Tel.: +47 73593919. E-mail: xiaoke.ku@ntnu.no.

Notes

The authors declare no competing financial interest.

■ ACKNOWLEDGMENTS

The authors would like to thank partners in CenBio, the BioEnergy Innovation Centre, and GasBio for financial support.

■ REFERENCES

(1) Umeki, K.; Yamamoto, K.; Namioka, T.; Yoshikawa, K. *Appl. Energy* **2010**, *87*, 791−798.

(2) Franco, C.; Pinto, F.; Gulyurtlu, I.; Cabrita, I. *Fuel* **2003**, *82*, 835−842.

(3) Li, X. T.; Grace, J. R.; Lim, C. J.; Watkinson, A. P.; Chen, H. P.; Kim, J. R. *Biomass Bioenergy* **2004**, *26*, 171−193.

(4) Meng, X.; de Jong, W.; Fu, N.; Verkooijen, A. H. M. *Biomass Bioenergy* **2011**, *35*, 2910−2924.

(5) Song, T.; Wu, J.; Shen, L.; Xiao, J. *Biomass Bioenergy* **2012**, *36*, 258−267.

(6) Hernández, J. J.; Aranda, G.; Barba, J.; Mendoza, J. M. *Fuel Process. Technol.* **2012**, *99*, 43−55.

(7) Qin, K.; Jensen, P. A.; Lin, W.; Jensen, A. D. *Energy Fuels* **2012**, *26*, 5992−6002.

(8) Qin, K.; Lin, W.; Jensen, P. A.; Jensen, A. D. *Fuel* **2012**, *93*, 589−600.

(9) Abani, N.; Ghoniem, A. F. *Fuel* **2013**, *104*, 664−680.

(10) Backreedy, R. I.; Fletcher, L. M.; Ma, L.; Pourkashanian, M.; Williams, A. *Combust. Sci. Technol.* **2006**, *178*, 763−787.

(11) Chen, C.; Horio, M.; Kojima, T. *Chem. Eng. Sci.* **2000**, *55*, 3875−3883.

(12) Chen, C.; Hung, C.; Chen, W. *Appl. Energy* **2012**, *100*, 218−228.

(13) Kumar, M.; Ghoniem, A. F. *Energy Fuels* **2012**, *26*, 451−463.

(14) Kumar, M.; Ghoniem, A. F. *Energy Fuels* **2012**, *26*, 464−479.

(15) Silaen, A.; Wang, T. *Int. J. Heat Mass Transfer* **2010**, *53*, 2074−2091.

(16) Watanabe, H.; Otaka, M. *Fuel* **2006**, *85*, 1935−1943.

(17) Álvarez, L.; Gharebaghi, M.; Pourkashanian, M.; Williams, A.; Riaza, J.; Pevida, C.; et al. *Fuel Process. Technol.* **2011**, *92*, 1489−1497.

(18) OpenFOAM Documentation, 2012; Available via the Internet at http://www.openfoam.org/docs/.

(19) Liu, A. B.; Mather, D.; Reitz, R. D. *SAE Techn. Pap. Ser.* **1993**, No. 930072.

(20) Ku, X.; Li, T.; Løvås, T. *Chem. Eng. Sci.* **2013**, *95*, 94−106.

(21) Ergüdenler, A.; Ghaly, A. E.; Hamdullahpur, F.; Al-Taweel, A. M. *Energy Source* **1997**, *19*, 1065−1084.

(22) Gerber, S.; Behrendt, F.; Oevermann, M. *Fuel* **2010**, *89*, 2903−2917.

(23) Prakash, N.; Karunanithi, T. *J. Appl. Sci. Res.* **2008**, *4*, 1627−1636.

(24) Evans, D. D.; Emmons, H. W. *Fire Res.* **1977**, *1*, 57−66.

(25) Klose, W.; Wölki, M. *Fuel* **2005**, *84*, 885−892.

(26) Marzouk, O. A.; Huckaby, E. D. *Eng. Appl. Comput. Fluid Mech.* **2010**, *4*, 331−356.

(27) Gómez-Barea, A.; Leckner, B. *Prog. Energy Combust.* **2010**, *36*, 444−509.

(28) Jones, W. P.; Lindstedt, R. P. *Combust. Flame* **1988**, *73*, 233−249.

(29) Chen, W.; Chen, C.; Hung, C.; Shen, C.; Hsu, H. *Appl. Energy* **2013**, *112*, 421−430.

Paper IV

Influence of drag force correlations on periodic fluidization behavior in Eulerian–Lagrangian simulation of a bubbling fluidized bed

Xiaoke Ku, Tian Li, Terese Løvås

Chemical Engineering Science, 95, 94−106, 2013

Chemical Engineering Science 95 (2013) 94–106

Contents lists available at SciVerse ScienceDirect

Chemical Engineering Science

journal homepage: www.elsevier.com/locate/ces

Influence of drag force correlations on periodic fluidization behavior in Eulerian–Lagrangian simulation of a bubbling fluidized bed

Xiaoke Ku*, Tian Li, Terese Løvås

Department of Energy and Process Engineering, Norwegian University of Science and Technology (NTNU), 7491 Trondheim, Norway

HIGHLIGHTS

- We investigate the effects of three well-known inter-phase drag force correlations.
- Formation of bubbles and slugs is observed to occur for all the drag models.
- Gidaspow model is most energetic and it predicts a lowest fluctuation frequency.
- No bubbling and slugging occur at all for the ideal-collision case ($e=1$, $\mu=0$).
- Increasing spring stiffness will slightly decrease the fluctuation frequency.

ARTICLE INFO

Article history:
Received 21 September 2012
Received in revised form
8 March 2013
Accepted 15 March 2013
Available online 23 March 2013

Keywords:
Particle
Multiphase flow
Drag correlations
Fluidization
Simulation
Fluctuation frequency

ABSTRACT

In this paper, an Eulerian–Lagrangian approach, in which the gas flow is solved by the volume-averaged Navier–Stokes equation and the motion of individual particles is obtained by directly solving Newton's second law of motion, is developed within the OpenFOAM framework to investigate the effects of three well-known inter-phase drag force correlations (Gidaspow, 1994, Di Felice, 1994 and EHKL, 2006) on the fluidization behavior in a bubbling fluidized bed reactor. The inter-particle and particle–wall collisions are modeled by a soft-sphere model which expresses the contact forces with the use of a spring, dashpot and friction slider. The simulation results are analyzed in terms of particle flow pattern, bed expansion, bed pressure drop and fluctuation frequency. Qualitatively, formation of bubbles and slugs and the process of particle mixing are observed to occur for all the drag models, although the Gidaspow model is found to be most energetic and the Di Felice and EHKL models yield minor difference. The flow behavior also shows a strong dependency on the restitution coefficient e and the friction coefficient μ and no bubbling and slugging occur at all for the ideal-collision case ($e=1$, $\mu=0$). Quantitatively, the mean pressure drops predicted by the three models agree quite well with each other and the amplitudes of the fluctuations measured by the standard deviation are also comparable. However, a significant difference in fluctuation frequency is found and the Gidaspow model predicts a lowest fluctuation frequency whereas the Di Felice model gets a highest one. Finally, effects of the spring stiffness and the discontinuity in the Gidaspow model are studied. The results show that both mean bed pressure drop and fluctuation frequency slightly decrease as the spring stiffness increases for all the three drag models and no significant differences are observed in the mean bed pressure drop and fluctuation frequency between the Gidaspow model and the linear continuous model.

1. Introduction

Gas–solid fluidized bed reactors are widely used in many industrial operations, such as gasification, combustion, catalytic cracking and various other chemical and metallurgical processes. Some of the compelling advantageous features of fluidized bed reactors are good mixing properties, high particle heating rates, and high reaction rates between gas and solids due to large gas–particle contact area. A good understanding of the hydrodynamic behavior of this system is important for the design and scale up of the new efficient reactors. Thus, in the last two decades significant research efforts have been devoted to the development of numerical models to study the complex hydrodynamics of gas–solid flows in fluidized bed reactors (see, among many others, Esmaili and Mahinpey, 2011; Hoomans et al., 2000; Kafui et al., 2002; Loha et al., 2012; Tsuji et al., 1993).

Generally, all the modeling methods developed can be broadly categorized into Eulerian–Eulerian and Eulerian–Lagrangian approaches. For Eulerian–Eulerian approach, both particle and fluid phases are treated as interpenetrating continua with

---

* Corresponding author. Tel.: +47 73593919/45186692.
E-mail address: xiaoke.ku@ntnu.no (X. Ku).

0009-2509/$ - see front matter © 2013 Elsevier Ltd. All rights reserved.
http://dx.doi.org/10.1016/j.ces.2013.03.038

appropriate interaction terms representing the coupling between the phases. It can predict the macroscopic characteristics of a system with relatively low computational cost and has actually dominated the modeling of fluidization process for many years (Gerber et al., 2010; Taghipour et al., 2005). However, in addition to the difficulty of providing closure models for mass exchange or inter-phase interaction within its continuum framework, Eulerian–Eulerian approach is unable to model the flow characteristics of individual particles. On the other hand, for Eulerian–Lagrangian approach which is sometimes called Discrete Element Method (DEM) (Cundall and Strack, 1979), the gas is treated as continuous and particle as discrete phase. The trajectories of individual particles are tracked in space and time by directly integrating the equations of motion while accounting for interactions with other particles, walls and the continuous phase. For dense particle system with multiple contacts between particles the soft-sphere collision model is usually applied. Eulerian–Lagrangian/DEM approach can offer detailed microscopic information, such as trajectories of individual particles and transient forces acting on each particle, which is extremely difficult, even impossible to obtain by macroscopic models or experiments (Jung and Gidaspow, 2005). The use of DEM for fluidized bed modeling was pioneered by Tsuji et al. (1993) and since then, thanks to the dramatic increase in computational capacity, DEM has come more and more into the focus of engineers and researchers (Lin et al., 2003; Papadikis et al., 2009; Su et al., 2011; Zhou et al., 2008).

For both Eulerian–Eulerian and Eulerian–Lagrangian approaches, a key consideration is the coupling between the phases. From a physical point of view, the coupling currently comprises the effect of (a) volume displacement by the particles, and (b) fluid–solid interaction forces exerted on the particles. These non-linear fluid–solid interaction forces or called generalized drag forces are believed to play a very important role in the formation of heterogeneous flow structures in dense gas-fluidized beds (Li and Kuipers, 2003). There are various drag correlations available in the literature. The Gidaspow correlation (Gidaspow, 1994) is a combination of the Ergun equation (Ergun, 1952) for dense granular regime (porosity $\varepsilon_g<0.8$) and the Wen and Yu equation (Wen and Yu, 1966) for dilute granular regime ($\varepsilon_g>=0.8$). This model is often used in the literature, but the transition between the two regimes is discontinuous, which may lead to convergence problems (Kloss et al., 2009). Di Felice (1994), using an empirical fit to a wide range of fixed and suspended-particle systems covering the full practical range of flow regimes and porosities, proposed a continuous single-function correlation for the drag force. More recently, Hill et al. (2001a, 2001b) proposed a Hill–Koch–Ladd (HKL) correlation applicable to different ranges of Reynolds numbers and solids volume fractions based on data from Lattice–Boltzmann simulations. Later Benyahia et al. (2006) blended HKL correlation with known limiting forms of the gas–solids drag function and constructed a extended HKL drag correlation (EHKL) which is applicable to the full range of solids volume fractions and Reynolds numbers. Although some works have investigated the effects of different drag models within the Eulerian–Eulerian framework under very different conditions from ours (Du et al., 2006; Esmaili and Mahinpey, 2011; Loha et al., 2012), few are reported for Eulerian–Lagrangian approach (Li and Kuipers, 2003). In our earlier paper (Ku et al., 2012), we reported some preliminary results of the qualitative influence of various drag models on the fluidization behavior. In this paper, we detailedly present an Eulerian–Lagrangian approach with a soft-sphere collision model for the simulation of a bubbling fluidized bed. The three drag correlations (Gidaspow, 1994, Di Felice, 1994 and EHKL, 2006) as described above are implemented in our model. The simulation results are analyzed both qualitatively and quantitatively in terms of particle flow pattern, bed pressure drop, and fluctuation frequency with a focus on the detailed comparison between the different drag models.

The rest of this paper is organized as follows. In Section 2, the equations of motion describing evolution of the spherical particles and gas phase are firstly formulated. Then the three different drag models and the simulation setup are tabulated. In Section 3, the numerical results of motion of particles in a bubbling fluidized bed are presented. Here, we first verify our approach by predicting the minimum fluidization velocity and compare our results with data available in the literature. Then we investigate the fluidization behavior and the pressure drop across the bed where the differences between the drag models are highlighted. Finally effects of the restitution coefficient e, the friction coefficient μ, the spring stiffness k_n and the effect of the discontinuity in the Gidaspow model are also documented. A short summary and conclusions are given in Section 4.

2. Mathematical modeling

2.1. Discrete particle phase

A particle in a gas–solid system undergoes translational and rotational motions as described by Newton's second law of motion. The equation governing the translational motion of particle i, which reads in a quiescent frame and in dimensional form, is

$$m_i \frac{d\boldsymbol{v}_i}{dt} = \boldsymbol{f}_{g,i} + \boldsymbol{f}_{c,i} + m_i \boldsymbol{g} \tag{1}$$

where m_i and $\boldsymbol{v}_i$ are, respectively, the mass and velocity of particle i, and $\boldsymbol{g}$ is the gravitational acceleration. $\boldsymbol{f}_{g,i}$ is the total fluid–particle drag force on the particle i including viscous drag force and pressure gradient force in the current case (Hill et al. (2001a, 2001b); Kafui et al., 2002; van der Hoef et al., 2005), and $\boldsymbol{f}_{c,i}$ is the total force on the particle i due to inter-particle or particle–wall contacts. Note that in the above force balance the added mass effects, Saffman lift force and Basset history force have been neglected, because they play a minor role for the type of flows considered here (Hoomans et al., 1996), as well as the buoyancy force which is allowed because of the negligible density of the gas phase with respect to the density of the particles.

The equation governing the rotational motion of particle i is

$$I_i \frac{d\boldsymbol{\omega}_i}{dt} = \boldsymbol{T}_i \tag{2}$$

where $\boldsymbol{\omega}_i$ is the angular velocity, $\boldsymbol{T}_i$ is the torque arising from the tangential components of the contact forces, and I_i is the moment of inertia, given as $I_i = 2/5 m_i R_i^2$ for spherical particles with radius R_i.

Particle-to-particle collision models can be generally classified as hard-sphere or soft-sphere models. In the hard-sphere model, the particles are assumed to be rigid spheres, and collisions among particles are treated as binary, instantaneous and impulsive events. The collisions are processed one by one according to the order in which the events occur. One advantage of the hard-sphere model is that there is an analytical solution available for the collision model. Given the velocities of the particles prior to collision together with the particle properties the post-collision velocities can be calculated exactly. The hard-sphere model is more suitable for simulations of dilute or rapid granular flows since it considers two-body collisions only. However, at high particle number densities, the hard sphere model may break down with long inter-particle contact durations. For further details on the implementation of the hard-sphere model the interested reader is referred to the works of Hoomans et al. (1996, 1999, 2000) and Deen et al. (2007).

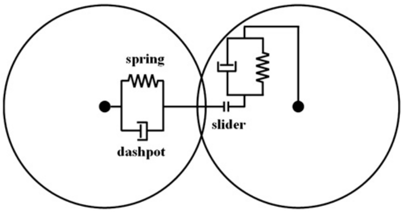

Fig. 1. The spring-slider-dashpot model.

Most of the commonly observed gas–solid flows are dense particle systems and exhibit multiple-particle and long-duration contacts. The soft sphere model, which is proposed by Cundall and Strack (1979), is the most applicable in such regimes and also adopted in this paper. In the soft-sphere model, the inter-particle contact forces, namely, the normal, sliding and damping forces, are computed using equivalent simple mechanical elements, such as spring, slider and dashpot (as shown in Fig. 1). The particles are allowed to overlap slightly. The normal force tending to repulse the particles can then be deduced from this spatial overlap and the normal relative velocity at the contact point. The spring stiffness k_n can be calculated by Hertzian contact theory when the physical properties such as Young's modulus and Poisson ratio are known. Particle–wall interactions are treated in the same way as particle–particle interactions except that the walls are assumed to be massive. Concerning the wall properties such as restitution and friction coefficients, the same values as the particle could apply. The net contact force $\boldsymbol{f}_{c,i}$ and torque $\boldsymbol{T}_i$ acting on each particle result from a vector summation of the forces and torques at each particle–particle or particle–wall contact. A characteristic feature of the soft particle models is that they are capable of handling multiple particle–particle contacts which is of importance when modeling dense particle systems. Moreover, non-contact force can also be incorporated into soft-sphere model easily. Detailed implementation issues of the soft-sphere model are available in the literature (e.g. Tsuji et al., 1992), which are not stated here for the sake of shortness.

2.2. Continuous gas phase

The continuum gas phase hydrodynamics are calculated from the continuity and volume-averaged Navier–Stokes equations which are coupled with those of the particle phase through the porosity and the inter-phase momentum exchange (Kafui et al., 2002).

The continuity equation is as follows:

$$\frac{\partial}{\partial t}\left(\varepsilon_g\rho_g\right)+\nabla\cdot\left(\varepsilon_g\rho_g\boldsymbol{u}_g\right)=0 \tag{3}$$

and the momentum equation is given by

$$\frac{\partial}{\partial t}\left(\varepsilon_g\rho_g\boldsymbol{u}_g\right)+\nabla\cdot\left(\varepsilon_g\rho_g\boldsymbol{u}_g\boldsymbol{u}_g\right)=-\nabla p+\nabla\cdot\left(\varepsilon_g\boldsymbol{\tau}_g\right)+\varepsilon_g\rho_g\boldsymbol{g}-\boldsymbol{S}_p \tag{4}$$

Here, ε_g is the porosity, and ρ_g, $\boldsymbol{u}_g$, $\boldsymbol{\tau}_g$ and p are the density, velocity, viscous stress tensor and pressure of the gas phase, respectively. $\boldsymbol{S}_p$ is a source term that describes the momentum exchange of the gas with the solid particles and will be discussed in more detail below. $\boldsymbol{\tau}_g$ is assumed to obey the general form for a Newtonian fluid (Bird et al., 1960),

$$\boldsymbol{\tau}_g=\lambda_g-\frac{2}{3}\mu_g\left(\nabla\cdot\boldsymbol{u}_g\right)\boldsymbol{I}+\mu_g\left(\left(\nabla\boldsymbol{u}_g\right)+\left(\nabla\boldsymbol{u}_g\right)^T\right) \tag{5}$$

where the bulk viscosity λ_g can be set to zero for gas, μ_g is the dynamic gas viscosity, and $\boldsymbol{I}$ is the identity tensor. The porosity ε_g, which denotes the fraction of a cell volume occupied by gas, is determined by

$$\varepsilon_g=1-\frac{\sum_{i=1}^{k_c}V_i}{\Delta V_{cell}} \tag{6}$$

where V_i is the volume of particle i and k_c is the number of particles in the computational cell with volume ΔV_{cell}.

As the fluid drag force acting on each particle $\boldsymbol{f}_{g,i}$ is known (see Section 2.1), according to Newton's third law of motion, the volumetric fluid–particle interaction force, $\boldsymbol{S}_p$, in a computational cell can be obtained by summing up the fluid forces $\boldsymbol{f}_{g,i}$ acting on all the particles in a fluid cell and dividing by the volume of the fluid cell ΔV_{cell}, thus

$$\boldsymbol{S}_p=\frac{1}{\Delta V_{cell}}\sum_{\forall i\in cell}\boldsymbol{f}_{g,i} \tag{7}$$

2.3. Drag models

The fluid drag force acting on particle i, $\boldsymbol{f}_{g,i}$, can be conventionally expressed as follows,

$$\boldsymbol{f}_{g,i}=\frac{V_i\beta}{\varepsilon_p}\left(\boldsymbol{u}_g-\boldsymbol{v}_i\right) \tag{8}$$

where $\boldsymbol{u}_g$ is the instantaneous gas velocity at the particle position, $\varepsilon_p=1-\varepsilon_g$, and β is the inter-phase momentum transfer coefficient. Three correlations for calculating β are summarized in Table 1.

As shown in Table 1, the Gidaspow model combines the Ergun (1952) and Wen and Yu (1966) correlations for the dilute and dense granular regime where a porosity ε_g of 0.8 is adopted as the boundary between these two regimes. This model is very common, but the step change inherent in the calculated drag forces at a porosity of 0.8 may be not good from a numerical point of view (Kafui et al., 2002). Di Felice (1994), using an empirical fit to a wide

Table 1
Three drag correlations proposed for particulate flows.

1. Gidaspow model (1994)

$$\beta=\left\{150\frac{\varepsilon_p^2\mu_g}{\varepsilon_g^2d_p^2}+1.75\frac{\varepsilon_p\rho_g}{\varepsilon_gd_p}\left|\boldsymbol{u}_g-\boldsymbol{v}_p\right|\varepsilon_g<0.8\,\frac{3}{4}C_d\frac{\varepsilon_p\rho_g}{d_p}\left|\boldsymbol{u}_g-\boldsymbol{v}_p\right|\varepsilon_g^{-2.65}\varepsilon_g\geq0.8\right.$$

$$C_d=\begin{cases}\frac{24}{Re_p}\left(1+0.15Re_p^{0.687}\right) & Re_p<1000\\ 0.44 & Re_p\geq1000\end{cases}$$

$$Re_p=\varepsilon_g\rho_gd_p|\boldsymbol{u}_g\text{-}\boldsymbol{v}_p|/\mu_g$$

2. Di Felice model (1994)

$$\beta=\frac{3}{4}C_d\frac{\varepsilon_p\varepsilon_g\rho_g}{d_p}\left|\boldsymbol{u}_g-\boldsymbol{v}_p\right|\varepsilon_g^{-\chi}$$

$$C_d=\left(0.63+4.8\frac{}{\sqrt{Re_p}}\right)^2.\ \chi=3.7-0.65\exp\left[-\frac{(1.5\text{-}\log_{10}(Re_p))^2}{2}\right]$$

$$Re_p=\varepsilon_g\rho_gd_p|\boldsymbol{u}_g\text{-}\boldsymbol{v}_p|/\mu_g$$

3. EHKL model (2006)

$$\beta=\frac{18\mu_g\varepsilon_g\varepsilon_p}{d_p^2}F$$

$$\begin{cases}F=1+3/8Re_p, & \varepsilon_p\leq0.01\text{ and }Re_p\leq(F_2-1)/(3/8-F_3)\\ F=F_0+F_1Re_p^2, & \varepsilon_p>0.01\text{ and }Re_p\leq(F_3+\sqrt{F_3^2-4F_1(F_0-F_2)})/(2F_1)\\ F=F_2+F_3Re_p, & \text{otherwise}\end{cases}$$

$$F_0=\begin{cases}(1-w)\frac{1+3\sqrt{\varepsilon_p/2}+(135/64)\varepsilon_p\ln(\varepsilon_p)+17.14\varepsilon_p}{1+0.681\varepsilon_p-8.48\varepsilon_p^2+8.16\varepsilon_p^3}+w\frac{10\varepsilon_p}{\varepsilon_g^3} & 0.01<\varepsilon_p<0.4\\ 10\varepsilon_p/\varepsilon_g^3 & \varepsilon_p\geq0.4\end{cases}$$

$$F_1=\begin{cases}\sqrt{2/\varepsilon_p}/40 & 0.01<\varepsilon_p\leq0.1\\ 0.11+0.00051e^{11.6\varepsilon_p} & \varepsilon_p>0.1\end{cases}$$

$$F_2=\begin{cases}(1-w)\frac{1+3\sqrt{\varepsilon_p/2}+(135/64)\varepsilon_p\ln(\varepsilon_p)+17.89\varepsilon_p}{1+0.681\varepsilon_p\text{-}11.03\varepsilon_p^2+15.41\varepsilon_p^3}+w\frac{10\varepsilon_p}{\varepsilon_g^3} & \varepsilon_p<0.4\\ 10\varepsilon_p/\varepsilon_g^3 & \varepsilon_p\geq0.4\end{cases}$$

$$F_3=\begin{cases}0.9351\varepsilon_p+0.03667 & \varepsilon_p<0.0953\\ 0.0673+0.212\varepsilon_p+0.0232/\varepsilon_g^5 & \varepsilon_p\geq0.0953\end{cases}$$

$$Re_p=\varepsilon_g\rho_gd_p|\boldsymbol{u}_g-\boldsymbol{v}_p|/2\mu_g.\ w=e^{\text{-}(10(0.4\text{-}\varepsilon_p)/\varepsilon_p)}$$

range of fixed and suspended-particle systems covering the full practical range of particle Reynolds number Re_p and ε_g, proposed a continuous single-function correlation for the drag force on a particle in a multi-particle system (Di Felice Model). Hill et al. (2001a, 2001b) proposed a set of drag correlations applicable to different ranges of Re_p and solids volume fractions ε_p, based on data from Lattice–Boltzmann simulations. These correlations do not cover the full range of Re_p and ε_p encountered in fluidized bed simulations. Later Benyahia et al. (2006) blended the Hill–Koch–Ladd (HKL) drag correlations with known limiting forms of the gas–solids drag function such that the blended function (EHKL model) is continuous with respect to Re_p and ε_p. Note that, in EHKL model, Re_p is based on particle radius, rather than particle diameter.

2.4. Computational methodology

Since the governing equations for the gas phase and the particle phase are different, different solution schemes have to be used. For discrete particle simulations, a first-order Euler time integration scheme is used to solve the translational and rotational motions of particles. For continuous gas phase, the governing equations are discretized in finite volume form and solved with a standard pressure based PISO (pressure implicit splitting of operators) solver for variable density flow. The coupling between the discrete particles and the gas phase is numerically achieved as follows. At each time step, the discrete particle equations of motion are first solved yielding the positions $\boldsymbol{r_i}$ and velocities $\boldsymbol{v_i}$ of individual particles. This enables the porosity ε_g and volumetric fluid–particle interaction force $\boldsymbol{S}_p$ of each computational cell to be calculated. Using the known values of ε_g and $\boldsymbol{S}_p$ at the current time, the gas-phase hydrodynamic equations are next solved to give the gas velocity and pressure fields from which the fluid drag forces $\boldsymbol{f}_{g,i}$ and torque $\boldsymbol{T}_i$ acting on individual particles are calculated. Using the $\boldsymbol{f}_{g,i}$ and $\boldsymbol{T}_i$ will produce information about the motion of individual particles for the next time step. All the above schemes have been developed and implemented into an open source C++ toolbox OpenFOAM (OpenCFD Ltd, 2011). Within the OpenFOAM framework, one can customize solvers or extend the numerical libraries to their own needs relatively easily which is a major advantage over commercial software. The codes are used in a variety of scientific applications, and there are an increasing number of researchers who are using OpenFOAM as their developing platform in their work on topics related to the present work (Oevermann et al., 2009; Su et al., 2011).

2.5. Simulation setup

The simulated fluidized bed geometry as shown schematically in Fig. 2 is similar to those of Tsuji et al. (1993) and Xu and Yu (1997). It consists of a rectangular container of dimension 0.15 m (width) × 0.9 m (height) × 0.004 m (thickness) with a jet orifice of 0.01 m in width at the center of the bottom wall. The left, right, bottom walls, the bottom orifice and the top exit consist of the whole calculation domain boundaries. The fluidization solid particles are a group of 2400 spherical particles with a diameter of 4 mm which are also taken from Tsuji et al. (1993) and Xu and Yu (1997). Note that the thickness of the bed is set equal to the particle diameter; that is, the bed contains one layer of particles. Air at a temperature of 293 K and standard atmospheric pressure is used as the fluidizing agent and introduced from the bottom orifice with a uniform velocity. This particle–fluid combination corresponds to a Geldart group D type (Geldart, 1973). Table 2 shows the parameter settings used in the simulation and the boundary conditions for the gas phase are listed in Table 3. Unless stated otherwise, all results of the following sections are based on the settings of Table 2.

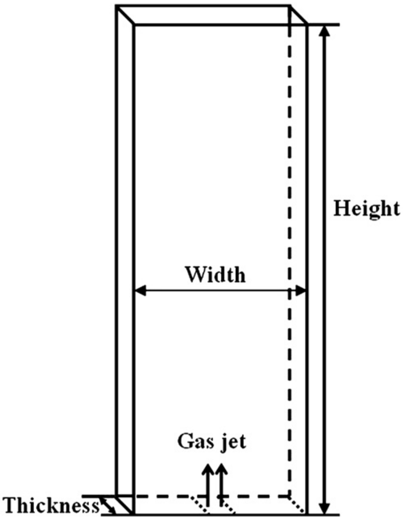

Fig. 2. Geometry of the fluidized bed reactor.

The grid resolution employed here is arrived at by a corresponding grid independence study. To seek a proper grid system, four different grid systems of (Δx, Δy)=(25 mm, 45 mm), (15 mm, 30 mm), (10 mm, 20 mm) and (5 mm, 10 mm) are tested. In the test, only air (293 K) with the uniform inlet velocity 0.01 m/s covering the whole bottom section is sent into the reactor. Fig. 3 displays the velocity distribution at the top exit of the reactor. It can be seen that the velocity profiles in terms of the third and fourth grid systems coincide with the analytic solution. This implies that the third grid system, i.e. (Δx, Δy)=(10 mm, 20 mm), can satisfy the requirement of grid independence. Moreover, for dense gas–solid flows, the choice of grid size is a little more complex. As is well-known, the grid size should be larger than the particle size for DEM simulations. Wang et al. (2009) concluded that in order to obtain correct bed expansion characteristics, the grid size should be of the order of three particle diameters. Considering the particle diameter is 4 mm in our study, (Δx, Δy)=(10 mm, 20 mm) is a good choice which takes both the grid independence and particle size into account. For the grid system of (Δx, Δy)=(10 mm, 20 mm), three small time steps, 1.0×10^{-4}, 1.0×10^{-5}, and 1.0×10^{-6} s which are consistent with the CFL criterion, are also tested to study the time step independence. No difference in the velocity profiles at the top exit is observed upon switching a time step 1.0×10^{-5} s to a smaller value of 1.0×10^{-6} s. So 1.0×10^{-5} s is chosen for all the simulation cases.

3. Results and discussions

3.1. Bed preparation

The first step of the fluidization simulation is to obtain an initial bed configuration which is generated as follows. The container is uniformly divided into a set of small rectangular lattices throughout the calculation domain. Then 2400 particles with zero velocity are positioned at the centers of these lattices and allowed to fall down under the influence of gravity in the absence of inlet jet gas. As shown in Fig. 4, pluvial deposition of the particles finally results in a static bed of height about 0.23 m and porosity around 0.42.

Table 2
Parameter settings for the simulations.

Particles		Gas phase		Bed	
Shape	Spherical	Viscosity, μ_g	1.8×10^{-5} Pa.s	Width	0.15 m
Diameter, d_p	4 mm	Density, ρ_g	[a]	Height	0.9 m
Density, ρ_p	2700 kg/m^3	Temperature, T	293 K	Thickness	4 mm
Number, N_p	2400	Fluid time step, Δt	1×10^{-5} s	Cell width, Δx	10 mm
Restitution coefficient, e	0.9	Inlet jet velocity	48 m/s	Cell height, Δy	20 mm
Friction coefficient, μ	0.3			Orifice width	10 mm

[a] ρ_g is determined using the ideal gas law.

Table 3
Boundary conditions for gas phase in the simulation.

Boundaries	Velocity	Pressure	Porosity
Left and right walls	No slip	Zero gradient	Zero gradient
Bottom wall	No slip	Zero gradient	Zero gradient
Inlet orifice (bottom)	Fixed value	Zero gradient	Fixed value
Outlet (top)	Zero gradient	Fixed value	Zero gradient

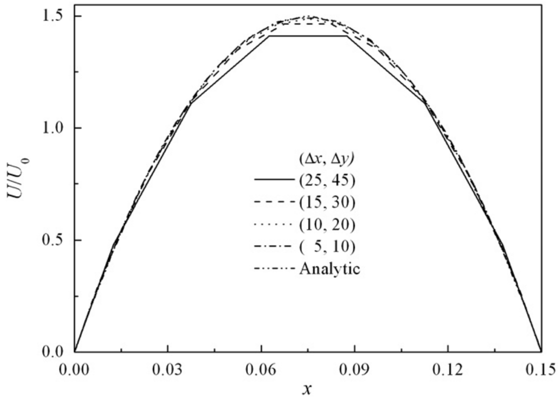

Fig. 3. Velocity distribution at the top exit when only air with the uniform inlet velocity U_0 = 0.01 m/s covering the whole bottom section is sent into the reactor.

This deposited bed is then used as the initial input data for the fluidization simulation. As pointed out by Xu and Yu (1997), the initial input data for fluidization include not only the particle coordinates but also the forces and torques which come with the deposition of particles in the packing process.

3.2. Minimum fluidization velocity

To test the validity of our approach, defluidization simulations, which allow the minimum fluidization velocity $\boldsymbol{u}_{mf}$ to be determined, are performed using each of the three drag correlations formulated in Table 1. As shown in Fig. 5, the defluidization curves are given by the mean pressure drop through the bed, $\Delta\overline{p}$ vs superficial gas velocity $\boldsymbol{u}_s$. The superficial gas velocity $\boldsymbol{u}_s$, here as an alternative to the gas jet velocity, is defined as the total volumetric gas flow rate divided by the entire bed cross-sectional area. Totally, 20 runs of simulation are carried out for each drag model, corresponding to the cases with a decreasing $\boldsymbol{u}_s$. The case for the maximum $\boldsymbol{u}_s$ of 3.2 m/s is simulated under the same boundary and initial conditions outlined in Section 3.1. Then the cases corresponding to the decreasing $\boldsymbol{u}_s$ are simulated by successively decreasing $\boldsymbol{u}_s$, with the final results at a higher velocity as the initial input data for the simulation at next lower velocity. All the cases are run for 10 s real time for statistical

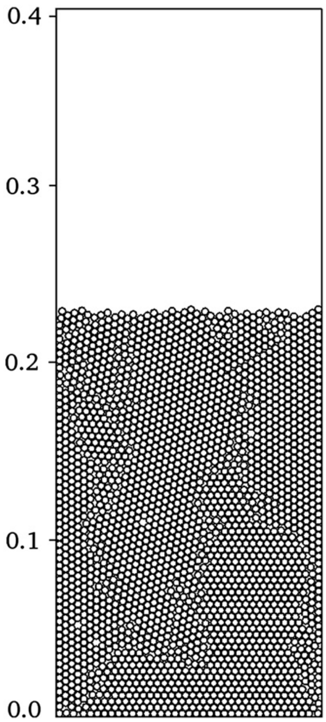

Fig. 4. Particle configurations after a simulated packing process.

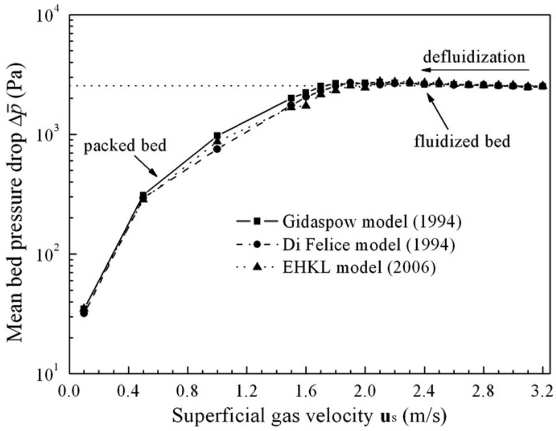

Fig. 5. Defluidization curves for the three drag models.

purpose. Two regimes are indentified from the defluidization curves: fluidized bed regime and packed bed regime. As will be delineated in the following section, at the fully fluidized bed regime, bubbles and slugs are generated continuously during the gas flow and particles move vigorously inside the bed. This regime is characterized by an almost constant mean bed pressure drop $\Delta\bar{p}$. It can be observed that all three drag models predict a complete fluidization at the same level of $\Delta\bar{p}$. The $\Delta\bar{p}$ keeps almost constant with decreasing $\boldsymbol{u}_s$ until a critical point (minimum fluidization velocity $\boldsymbol{u}_{mf}$) is reached. After $\boldsymbol{u}_{mf}$ $\Delta\bar{p}$ starts to continuously decrease with decreasing $\boldsymbol{u}_s$ and a packed bed regime where no bubbles exist is generated. The dotted horizontal line in Fig. 5 indicates the constant mean pressure drop at fluidized bed regime and it intersects the defluidization curves at point $\boldsymbol{u}_{mf}$. Table 4 shows the comparison of predicted values of minimum fluidization velocity $\boldsymbol{u}_{mf}$ by the three drag models with the numerical data reported by other investigators (Boyalakuntla, 2003; Hoomans et al., 1996; Xu and Yu, 1997). It can be seen that good agreement is obtained. Fig. 6 depicts the predicted porosity distributions at minimum fluidization velocity $\boldsymbol{u}_{mf}$ for the three drag models. It is observed that only a small bubble forms at the jet region and the porosity distribution is relatively homogeneous through the bed which indicates that the gas could pass through the bed without resulting in a rigorous particle flow. There are no significant differences in porosity distribution among the three drag models except for the upper surface of the bed.

The $\boldsymbol{u}_{mf}$ is a key quantity for fluidized bed and the successful prediction of this quantity thereby provides an important example to verify the proposed approach. It should be noted that, although the deviation is not large, Gidaspow model predicts a smallest $\boldsymbol{u}_{mf}$ while EHKL model gives a largest one.

Table 4
Comparison of predicted values of minimum fluidization velocity $\boldsymbol{u}_{mf}$ by the three drag models with the data reported by other investigators.

Drag model used	Minimum fluidization velocity $\boldsymbol{u}_{mf}$ (m/s)			
	This work	Hoomans et al. (1996)	Xu and Yu (1997)	Boyalakuntla (2003)
Gidaspow (1994)	1.7	1.77	–	1.85[a]
Di Felice (1994)	1.8	–	1.8	–
EHKL (2006)	1.9	–	–	

[a] The drag model used by Boyalakuntla (2003) is not explicitly specified in his work.

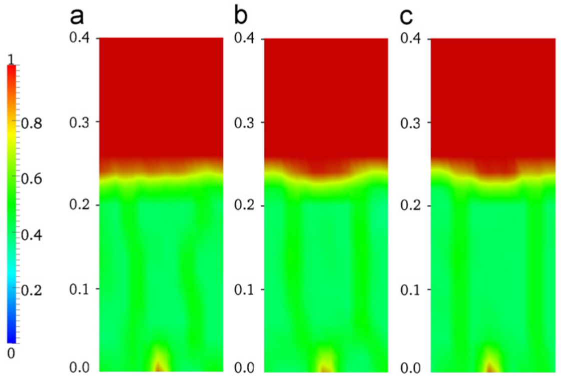

Fig. 6. Simulated porosity distributions at minimum fluidization velocity for the three drag models. (a) Gidaspow model; (b) Di Felice model; (c) EHKL model.

3.3. Fluidization behavior

Using the particle configurations as shown in Fig. 4 as the initial input, a single central jet of air with velocity of 48 m/s is injected from the bottom orifice to investigate the fluidization behavior. From detailed examinations of the video sequences of the simulations (available on demand), two ranges are identified: the start-up stage and the fluidization stage. The start-up time range 0.00–0.40 s can be roughly recognized from the first fluctuation of Fig. 11 which depicts the bed pressure drop Δp against time t in the following section. Fig. 7 illustrates the comparison of simulated particle flow patterns using different drag models at the start-up stage. As an initial response of the bed to the introduction of fluidizing gas, a significant upward flow of particles is caused due to the instantaneous breakup of the inter-particle locking. For all models, it is readily observed that a bubble with an oval shape is formed at the jet region, which forces particles in its front to rise and then fall down along the walls. This bubble grows as gas flows upward and eventually collapses. Besides the bubble formation, the existence of “slug” structure at the upper part of the bed is also clearly predicted by all the models. The term “slug” is used here to describe a dilute region of particles which occupies the whole width of the bed and a similar definition is also given by other investigators (Hoomans et al., 1996; Kafui et al., 2002). The formation of bubbles and slugs in a spouting bed of Geldart group D type powder is also reported in the literature both numerically (Boyalakuntla, 2003; Hoomans et al., 1996; Xu and Yu, 1997) and experimentally (Tsuji et al., 1993). Although the bubble shape and slug structure are accurately predicted by all the three models, the size of them as well as the height of bed expansion is different. It is easily seen that the Gidaspow model predicts the biggest bubble and slug structure. At $t = 0.20$ s, a bed expansion estimated at 70% of the initial bed height is observed for the Gidaspow model compared to 50% for the Di Felice model and 40% for the EHKL model.

After the start-up stage, a dynamically stable fluidization stage is reached in which a periodic generation of bubbles and slugs is observed. Fig. 8 shows the typical particle flow patterns at this stage for the three drag models. Because the total simulation time is 20 s, a time range which is close to 10 s (half of the total simulation time) is chosen to act as a general representative period for all the models. For each model, five snapshots of the particle patterns show the rise and fall of a bubble which roughly represents a period, which shows that the bubbling period is longest for Gidaspow model and almost same for Di Felice and EHKL models. Similar to the start-up stage, the particle flow patterns predicted by the three models featured by a gas cavity at the jet region above which a bubble is formed and continuously grows and rises until converts to a slug. However, the bubble and slug patterns can differ significantly among the drag models and their intensity is strongest for Gidaspow model and much weaker for Di Felice and EHKL models. These observed differences suggest that the performance characteristics obtainable from the different drag models differ, perhaps significantly, depending on the particular application.

As indicated in Eq. (1), the motion of a particle is governed by the gravitational, fluid drag and inter-particle forces. The fluid drag is closely related to the particle configuration (porosity), gas–solid slip velocity and properties of the gas and the particles. Fig. 9 presents plot of the drag forces acting on a single particle for the three drag models as a function of porosity ε_g at three gas–solid slip velocities $|\boldsymbol{u}_g - \boldsymbol{v}_p|$. In the plot the step change inherent in the calculated drag forces from the Gidaspow model at a porosity ε_g of

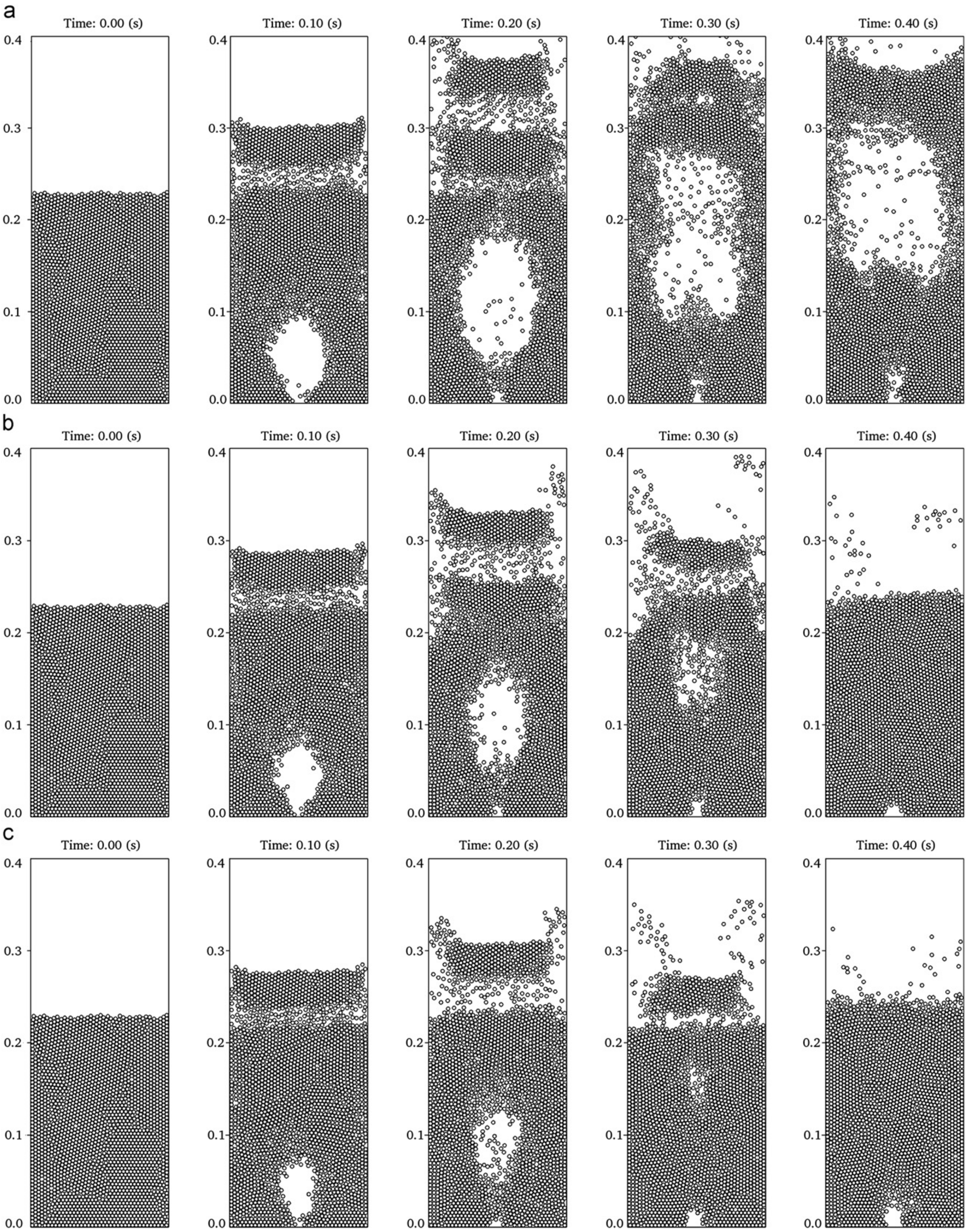

Fig. 7. Particle flow patterns at the start-up stage. (a) Gidaspow model; (b) Di Felice model; (c) EHKL model.

0.8 is clearly observed. Three scenarios exist for constant $|\boldsymbol{u}_g - \boldsymbol{v}_p|$. First, for $\varepsilon_g < 0.4$, Di Felice and EHKL models predict drag forces close to each other which are larger than the one produced by Gidaspow model. Second, for ε_g between 0.4 and 0.8, Gidaspow model gives much larger drag force than Di Felice and EHKL models. Finally, for $\varepsilon_g > 0.8$, Gidaspow model has a step change and produces a smallest drag force. These trends for the three slip velocities are similar, but the intersections of the curves shift to lower porosities when $|\boldsymbol{u}_g - \boldsymbol{v}_p|$ increases. Considering ε_g ranges from about 0.42 (packed bed as shown in Fig. 4) to 0.96 (only one particle in a fluid cell) for our simulation cases, it is reasonable that Gidaspow model is found to be most energetic as shown in

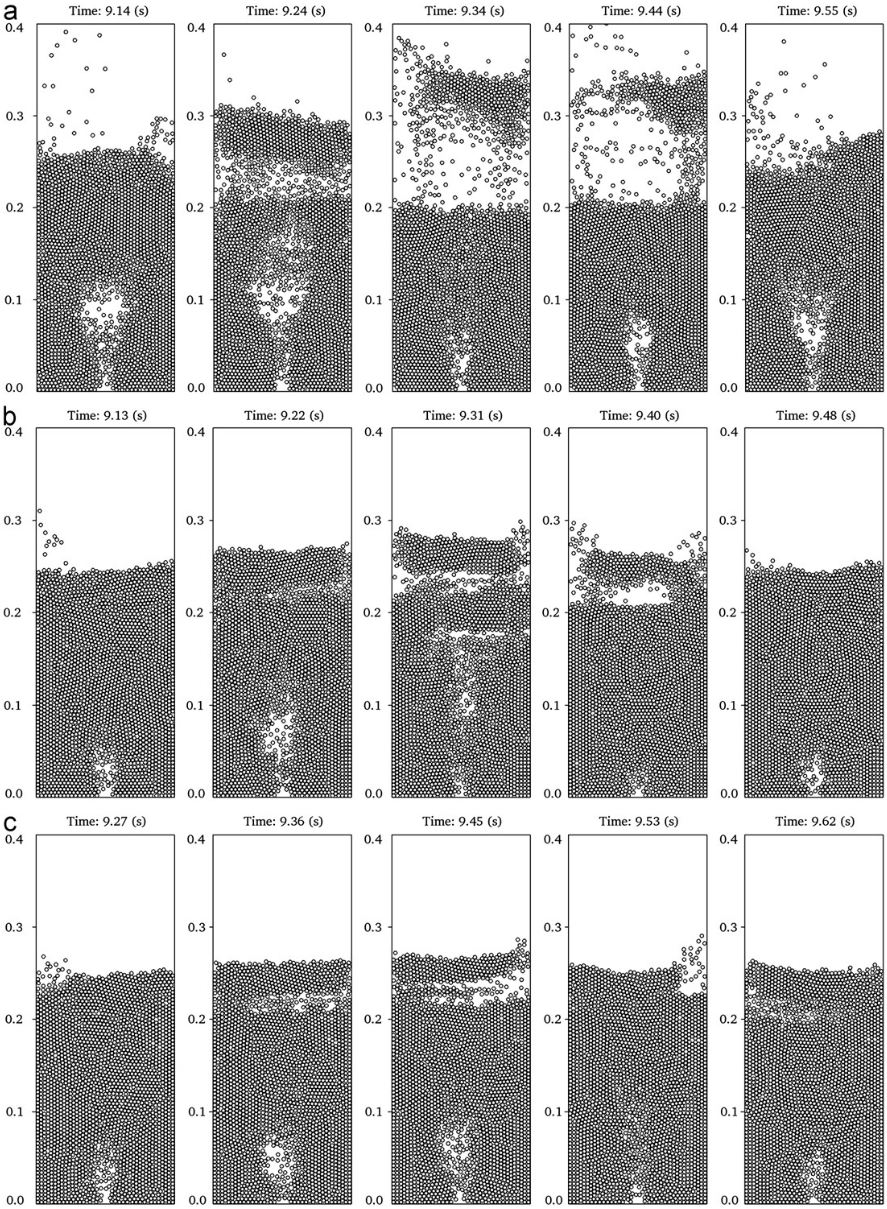

Fig. 8. Typical particle flow patterns at the fluidization stage. (a) Gidaspow model; (b) Di Felice model; (c) EHKL model.

Figs. 7 and 8. Moreover, EHKL and Di Felice models intersect at a point around $\varepsilon_g = 0.6$ and produce a same level drag force for $\varepsilon_g < 0.8$ which is a possible explanation to the similar fluidization behaviors observed for these two models.

From the fluidization behavior shown in Figs. 7 and 8, we know that most of the particle mixing occurs in two fast particle flow regions: one is away from the bottom orifice due to the gas dragging in the main stream (bubble) and the other at the upper part of the bed due to the falling of the particles to fill in the vacant space (slug). There is a big vortex developed corresponding to these two fast flow regions, which promotes particle mixing considerably. However, near the bottom corners the particles become consolidated and mix slowly. If the particles are initially colored in layers gradually changed from blue at bottom to red at top, the degree of mixing at the end of simulation ($t = 20$ s) for different models are shown in Fig. 10. It is evident that the mixing is best for the Gidaspow model and the particle distribution appears to be uniform throughout the bed. Whereas for Di Felice and EHKL models there is still local accumulation of red particles along the right wall and the degree of mixing is comparable for the two models.

3.4. Bed pressure drop

In the previous section, most comparisons between the different drag models are qualitative. In order to quantify the differences, the pressure drop across the bed Δp, which is obtained as the difference between the average gas pressure in the bottom and top rows of the computational cells, is recorded over a sufficiently long time (20 s) to permit the calculation of a time-averaged value. Fig. 11 shows a comparison between all drag models in prediction of Δp against time. It is easily seen that Δp fluctuates with time and a similar fluctuating pattern is observed for the three drag models. At the start-up stage the bed pressure drop is much higher than that at the stable fluidization stage because of the need to overcome the inter-particle locking. The mean pressure drops of 2.51 kPa, 2.54 kPa and 2.53 kPa for the Gidaspow, Di Felice and EHKL models, respectively, agree quite well with each other and the amplitudes of the fluctuations measured by the standard deviation (sd), are also comparable. However, a significant difference is still evident from Fig. 11 in that Gidaspow model predicts the lowest fluctuation frequency (2.45 Hz), about 85% of what is predicted by the two other models. The frequencies predicted by Di Felice and EHKL models are close to each other, although a slightly higher (~4%) frequency is obtained with Di Felice model.

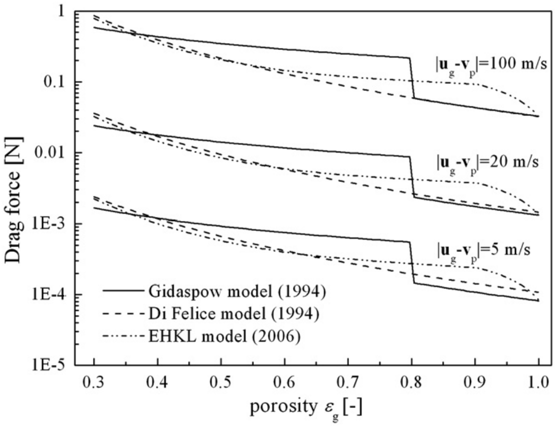

Fig. 9. Comparison of drag forces acting on a 4 mm diameter particle as predicted using the Gidaspow model, Di Felice model, and EHKL model for a range of porosities at three superficial slip velocities.

The bed pressure drop fluctuations in a bubbling fluidized bed are considered to be caused by bubbles and slugs that form and collapse at regular intervals (Boyalakuntla, 2003). From a close inspection of Figs. 8 and 11, we see that the pressure fluctuation frequency is in accordance with the bubbling frequency thus supporting the idea that bubbles and slugs are a major cause for the pressure fluctuations. Based on the work of Tho-Ching and Walawender (1983), bigger bubble or slug structure has higher rise velocity. Since Gidaspow model produces bigger bubble and slug than Di Felice and EHKL models, the bubble rise velocity of Gidaspow model is highest which is in contradiction to the lowest pressure fluctuation frequency predicted by Gidaspow model as shown in Fig. 11 at first glance. Keep in mind that Gidaspow model also gives the largest bed expansion and the fluctuation period is related to the ratio of the expanded bed height to the rise velocity. The lowest fluctuation frequency (i.e. longest period) predicted by Gidaspow model implies that the traveling distance of the bubble dominates its rise velocity for our simulation cases.

3.5. Effect of collision parameters e and μ

In order to study the effect of the two key collision parameters: the restitution coefficient e, and the friction coefficient μ, on the fluidization behavior, an ideal-collision case ($e=1$, $\mu=0$) is also simulated. Fig. 12 shows the snapshots of particle flow patterns for the ideal-collision case at $t=15$ s for the three drag models. Moreover, in the animation of the results it can be observed that, except for the start-up stage ($t<1$ s), no bubbling and slugging occur at all and after a vigorous expansion the bed remains rather homogeneously fluidized, which is completely different from the case with non-ideal, more realistic particles ($e=$ 0.9, $\mu=0.3$) as

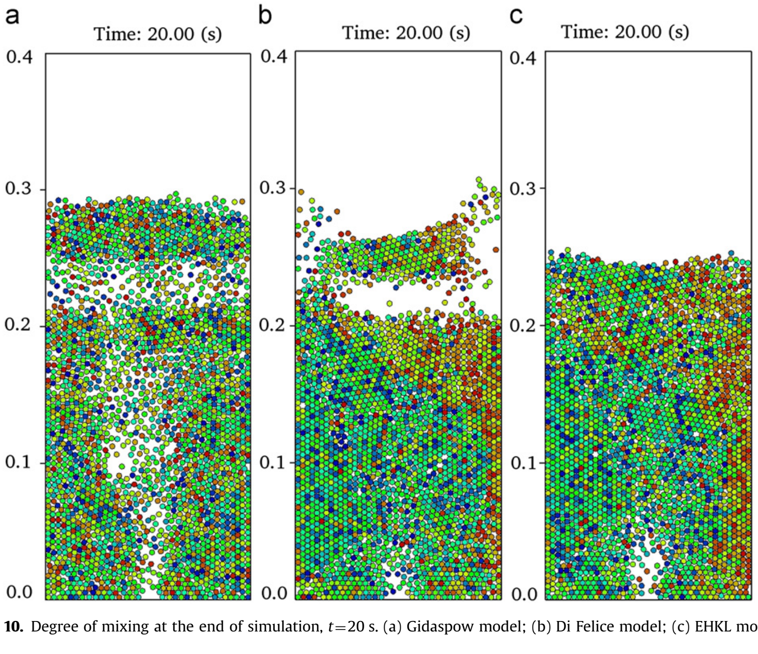

Fig. 10. Degree of mixing at the end of simulation, $t=20$ s. (a) Gidaspow model; (b) Di Felice model; (c) EHKL model.

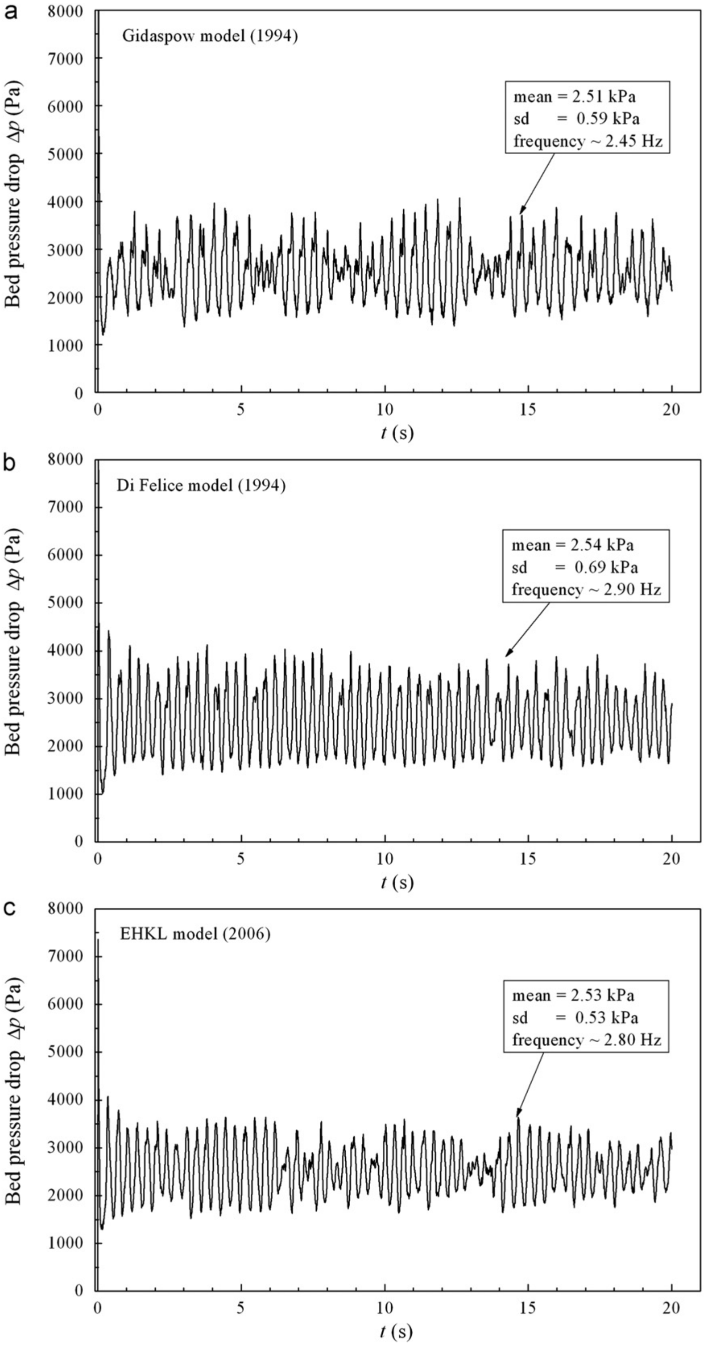

Fig. 11. Bed pressure drop Δp against time t. (a) Gidaspow model; (b) Di Felice model; (c) EHKL model.

shown in Fig. 8 where a bubble experiences its generation, growth and collapse process periodically. A possible explanation for this phenomenon is depicted in Fig. 13. As shown in Fig. 13, the bed pressure drop Δp is almost constant with time in the ideal-collision case, which results in a nearly homogeneous flow structure (constant bed expansion). However, the pressure fluctuation in the non-ideal case is much larger than that in the ideal case, implying that it produces a more heterogeneous flow structure (periodic bubbling). This phenomenonal difference indicates that material properties, as reflected by collision parameters (e and μ) have a strong influence on the particle pattern formation. Therefore, real parameters should be chosen in order to obtain

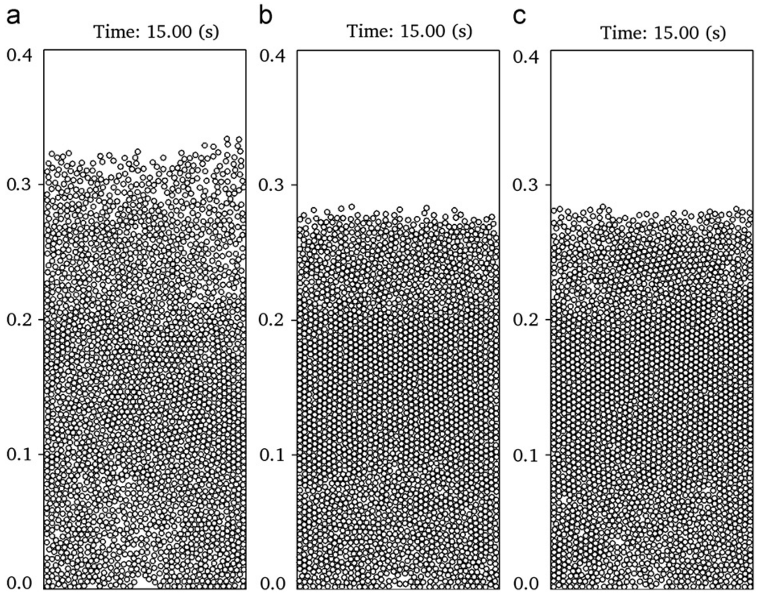

Fig. 12. Snapshots of particle flow patterns at $t = 15$ s for ideal-collision case ($e = 1$, $\mu = 0$). (a) Gidaspow model; (b) Di Felice model; (c) EHKL model.

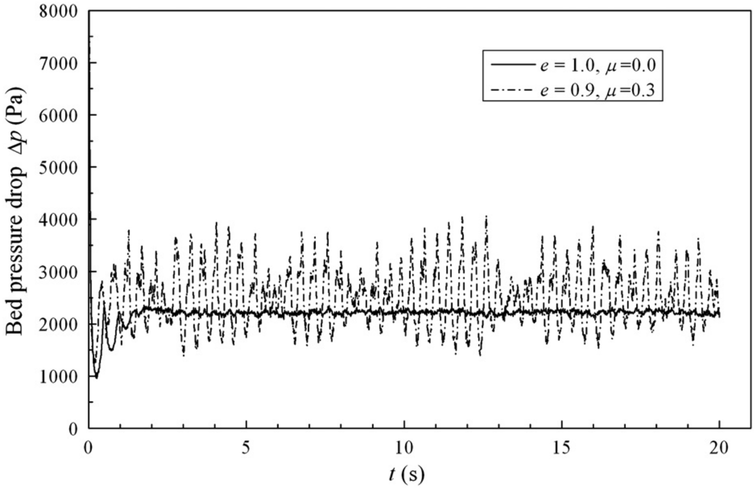

Fig. 13. The comparison of bed pressure drop Δp between the ideal-collision case ($e = 1$, $\mu = 0$) and the non-ideal collision case ($e = 0.9$, $\mu = 0.3$) for Gidaspow model.

realistic fluidization behavior. As also shown in Fig. 12, although all the three drag models predict no bubble and slug formation for the ideal case, the height of the expanded bed is different and Gidaspow model has the largest bed expansion, this feature is consistent with the previous findings in Section 3.3. It is worth to mention that Hoomans et al. (1996) who adopted a hard-sphere collision model in contrast to our soft-sphere model also reported the same phenomenon as ours for the ideal-collision case, which qualitatively verifies the capacity of our approach.

Li and Kuipers (2003) explored the effect of non-linearity of the gas drag by altering values of the exponent of the porosity ε_g in drag correlations. They found that, when increasing the exponent of ε_g, the flow structure displays many modes, ranging from perfectly homogeneous particulate flow with small bed expansion to heterogeneous flow with high bed expansion for ideal-collision case. From Table 1, it is easily observed that the increase of porosity exponent provides a stronger drag force acting on the particles and it will make the bed height increase dramatically. They also reported that the heterogeneous flow structure for ideal-collision case features with looser packing, which differs significantly from the heterogeneous flow structure in non-ideal case (clear bubble or slug formation). The loose packing of particles in the ideal system is attributed to the fact that no energy is dissipated during the frequent particle–particle collisions. This loose-packing feature is in agreement with the phenomenon presented in Fig. 12. Since the conventional values of porosity exponent are kept for each drag model in our work, enhancing exponent of the porosity to produce more heterogeneous flow structure for idea-collision case like Li and Kuipers (2003) did is beyond the scope of this work.

3.6. Effect of spring stiffness

The spring stiffness is also a parameter needed to be predetermined for the soft-sphere collision model adopted in this work. As discussed in Section 2.1, using the Hertzian contact theory, the spring stiffness can be calculated from the physical properties such as Young's modulus and Poisson ratio (Tsuji et al., 1992). The previous researchers (Hoomans, 1999; Xu and Yu, 1997; Tsuji et al., 1993) usually assumed that the effect of spring stiffness on particle motion was negligible and a small value (10^2–10^4) was arbitrarily chosen to save computation time. To test the influence of the spring stiffness, totally three runs of simulation are carried out for each drag model, corresponding to the cases with an increasing spring stiffness of one order of magnitude. Table 5 lists the predicted mean pressure drops and fluctuation frequencies. It can be observed that both bed pressure drop and fluctuation frequency decrease as the spring stiffness increases for all the drag models although the variation is small. Therefore if experimental data are available and one aims to improve the agreement between the simulated result and the experimental one, the spring stiffness is also an issue needed to be taken into account. After detailed examinations of the video sequences of the simulations, the effect of the spring stiffness on the fluctuation frequency can be explained as follows. As discussed in Section 3.4, the fluctuation frequency is in accordance with the bubbling frequency. With an increase in the spring stiffness, the particles become more rigid and the overlap allowed between them becomes smaller which leads to a particle configuration where the particles are less closely spaced which results in a higher expanded bed. Consequently it will take a rising bubble a little longer time (a lower frequency) to travel through a higher bed.

Table 5
Simulation results of various stiffnesses for the three drag models.

Model	Spring stiffness k_n, (N/m)	Mean bed pressure drop, $\Delta\bar{p}$ (kPa)	Frequency f, (Hz)
Gidaspow (1994)	1.28×10^5	2.51	~2.45
	1.28×10^6	2.50	~2.30
	1.28×10^7	2.49	~2.20
Di Felice (1994)	1.28×10^5	2.54	~2.90
	1.28×10^6	2.51	~2.70
	1.28×10^7	2.49	~2.65
EHKL (2006)	1.28×10^5	2.53	~2.80
	1.28×10^6	2.52	~2.70
	1.28×10^7	2.51	~2.55

3.7. Effect of the discontinuity in the Gidaspow model

As mentioned above, the Gidaspow drag model has a discontinuous transition between the Ergun (1952) and Wen and Yu (1966) correlations at a gas volume fraction ε_g of 0.8. Physically, the drag force is a continuous function of both particle Reynolds number Re_p and ε_g and therefore drag models should be continuous functions. In order to remove the discontinuity in the Gidaspow model, here, a similar approach to the one used by Leboreiro et al. (2008a) is implemented, namely a linear interpolation over a transition region. The Ergun (1952) expression (denoted by β_E) for the inter-phase momentum transfer coefficient, is used when ε_g is below 0.7. If ε_g is above 0.8, then the Wen and Yu (1966) correlation (denoted by β_{WY}) is employed. If ε_g lies in the transition region between 0.7 and 0.8, the following linear interpolation is adopted:

$$\beta_{TG}=\beta_E\frac{0.8-\varepsilon_g}{0.1}+\beta_{WY}\frac{\varepsilon_g-0.7}{0.1} \tag{9}$$

where β_{TG} is the inter-phase momentum transfer coefficient in the linear transition region for the Gidaspow model. Fig. 14 presents the bed pressure drop Δp against time t for the original Gidaspow model and the linear continuous one described above. No significant differences are observed in the mean pressure drop and fluctuation frequency between the original Gidaspow model and the continuous one, which is consistent with the findings by Leboreiro (2008b).

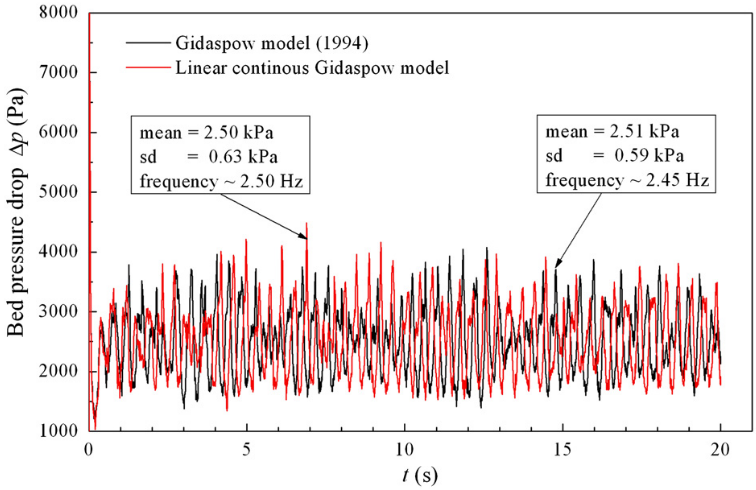

Fig. 14. Bed pressure drop Δp against time t for Gidaspow model and the linear continuous Gidaspow model.

4. Conclusions

Numerical simulations of a bubbling gas–solid fluidized bed reactor have been performed in a pseudo-3D domain using the Eulerian–Lagrangian approach to investigate the effects of three widely used drag correlations on the hydrodynamic behaviors. A soft-sphere model is adopted to resolve the inter-particle and particle–wall collision dynamics. The results have been analyzed in terms of particle flow pattern, bed expansion height, bed pressure drop, and fluctuation frequency. Qualitatively, formation of bubbles and slugs and the process of particle mixing are observed to occur for all the drag models, although the Gidaspow model is found to be most energetic and the Di Felice and EHKL models yield minor difference. Quantitatively, the mean pressure drops predicted by the three models agree quite well with each other and the amplitudes of the fluctuations measured by the standard deviation are also comparable. However, a significant difference in the frequency of pressure fluctuations is found that the Gidaspow model predicts a lowest fluctuation frequency whereas the Di Felice gets a highest one. Considering that there are more than 10 drag correlations available in the literature (Esmaili and Mahinpey, 2011; Loha et al., 2012), care must be taken to make a suitable choice for one's particular application.

The effects of restitution coefficient e, friction coefficient μ, and spring stiffness k_n on the fluidization behavior are also investigated in this study. It is found that no bubbling and slugging occur at all for the ideal-collision case ($e=1$, $\mu=0$) and that both mean bed pressure drop and fluctuation frequency slightly decrease as the spring stiffness increases for all the three drag models. Finally, the discontinuity in the Gidaspow model is removed by a linear interpolation scheme and no significant differences are observed in the mean bed pressure drop and fluctuation frequency between the original Gidaspow model and the linear continuous model. However, fluidized bed is a huge and very complicated multiphase-flow system, and is affected by many related issues such as container geometry, operational conditions, particle size distribution and material properties. Further modeling efforts are required to study the influence of all these parameters. Moreover, new experimental studies should be carried out using recent advancements in instrumentation engineering in order to compare with our modeling results.

Acknowledgments

The authors would like to thank partners in CenBio, the BioEnergy Innovation Center, and GasBio for financial support.

References

Benyahia, S., Syamlal, M., O'Brien, T.J., 2006. Extension of Hill-Koch-Ladd drag correlation over all ranges of Reynolds number and solids volume fraction. Powder Technol. 162, 166–174.

Bird, R.B., Stewart, W.E., Lightfoot, E.N., 1960. Transport Phenomena. John Wiley and Sons, New York.

Boyalakuntla, D.S., 2003. Simulation of Granular and Gas-Solid Flows Using Discrete Element Method. Ph.D. Thesis, Carnegie Mellon University, Pittsburgh, Pennsylvania.

Cundall, P.A., Strack, O.D.L., 1979. A discrete numerical model for granular assemblies. Geotechnique 29, 47–65.

Deen, N.G., van Sint Annaland, M., van der Hoef, M.A., Kuipers, J.A.M., 2007. Review of discrete particle modeling of fluidized beds. Chem. Eng. Sci. 62, 28–44.

Di Felice, R., 1994. The voidage function for fluid-particle interaction systems. Int. J. Multiphase Flow 20, 153–159.

Du, W., Bao, X., Xu, J., Wei, W., 2006. Computational fluid dynamics (CFD) modeling of spouted bed: Assessment of drag coefficient correlations. Chem. Eng. Sci. 61, 1401–1420.

Ergun, S., 1952. Fluid flow through packed columns. Chem. Eng. Prog. 48, 89–94.

Esmaili, E., Mahinpey, N., 2011. Adjustment of drag coefficient correlations in three dimensional CFD simulation of gas-solid bubbling fluidized bed. Adv. Eng. Software 42, 375–386.

Gerber, S., Behrendt, F., Oevermann, M., 2010. An Eulerian modeling approach of wood gasification in a bubbling fluidized bed reactor using char as bed material. Fuel 89, 2903–2917.

Gidaspow, D., 1994. Multiphase Flow and Fluidization. Academic Press, San Diego, USA.

Hill, R.J., Koch, D.L., Ladd, A.J.C., 2001a. The first effects of fluid inertia on flows in ordered and random arrays of spheres. J. Fluid Mech. 448, 213–241.

Hill, R.J., Koch, D.L., Ladd, A.J.C., 2001b. Moderate-Reynolds-number flows in ordered and random arrays of spheres. J. Fluid Mech. 448, 243–278.

Hoomans, B.P.B., 1999. Granular Dynamics of Gas-Solid Two-Phase Flows. Ph.D. Thesis, University of Twente, Enschede, The Netherlands.

Hoomans, B.P.B., Kuipers, J.A.M, Briels, W.J., van Swaaij, W.P.M., 1996. Discrete particle simulation of bubble and slug formation in a two-dimensional gas fluidised bed: A hard-sphere approach. Chem. Eng. Sci. 51, 99–118.

Hoomans, B.P.B., Kuipers, J.A.M., van Swaaij, W.P.M., 2000. Granular dynamics simulation of segregation phenomena in bubbling gas-fluidised beds. Powder Technol. 109, 41–48.

Jung, J., Gidaspow, D., 2005. Measurement of two kinds of granular temperatures, stresses, and dispersion in bubbling beds. Ind. Eng. Chem. Res. 44, 1329–1341.

Kafui, K.D., Thornton, C., Adams, M.J., 2002. Discrete particle-continuum fluid modelling of gas-solid fluidised beds. Chem. Eng. Sci. 57, 2395–2410.

Kloss, C., Goniva, C., Aichinger, G., Pirker, S., 2009. Comprehensive DEM-DPM-CFD simulations model synthesis, experimental validation and scalability. In: Seventh International Conference on CFD in the Minerals and Process Industries CSIRO, Melbourne, Australia.

Ku, X., Li, T., Løvås, T., 2012. Eulerian–Lagrangian simulation of a bubbling fluidized bed reactor: Assessment of drag force correlations. Thermal Sci. 16, 1442–1445.

Leboreiro, J., et al., 2008a. The influence of binary drag laws on simulations of species segregation in gas-fluidized beds. Powder Technol. 184, 275–290.

Leboreiro, J., 2008b. Influence of Drag Laws on Segregation and Bubbling Behavior in Gas-Fluidized Beds. Ph.D. Thesis, University of Colorado, Boulder, USA.

Li, J., Kuipers, J.A.M., 2003. Gas-particle interactions in dense gas-fluidized beds. Chem. Eng. Sci. 58, 711–718.

Lin, J., Shi, X., Yu, Z., 2003. The motion of fibers in an evolving mixing layer. Int. J. Multiphase Flow 29, 1355–1372.

Loha, C., Chattopadhyay, H., Chatterjee, P.K., 2012. Assessment of drag models in simulating bubbling fluidized bed hydrodynamics. Chem. Eng. Sci. 75, 400–407.

Oevermann, M., Gerber, S., Behrendt, F., 2009. Euler–Lagrange/DEM simulation of wood gasification in a bubbling fluidized bed reactor. Particuology 7, 307–316.

OpenCFD Ltd, 2011. OpenFOAM – The Open Source CFD Toolbox-User Guide (Version 2.1.0) ⟨http://www.openfoam.org/docs⟩/.

Papadikis, K., Gu, S., Bridgwater, A.V., Gerhauser, H., 2009. Application of CFD to model fast pyrolysis of biomass. Fuel Process. Technol. 90, 504–512.

Su, J., Gu, Z., Xu, X.Y., 2011. Discrete element simulation of particle flow in arbitrarily complex geometries. Chem. Eng. Sci. 66, 6069–6088.

Taghipour, F., Ellis, N., Wong, C., 2005. Experimental and computational study of gas-solid fluidized bed hydrodynamics. Chem. Eng. Sci. 60, 6857–6867.

Tho-Ching Ho, L.T.F., Walawender, W.P., 1983. Measurements of the rise velocities of bubbles, slugs and pressure waves in a gas-solid fluidized bed using pressure fluctuation signals. AIChE J. 29, 33–39.

Tsuji, Y., Tanaka, T., Ishida, T., 1992. Lagrangian numerical simulation of plug flow of cohesionless particles in a horizontal pipe. Powder Technol. 71, 239–250.

Tsuji, Y., Kawaguchi, T., Tanaka, T., 1993. Discrete particle simulation of two-dimensional fluidized bed. Powder Technol. 77, 79–87.

Van der Hoef, M.A., Beetstra, R., Kuipers, J.A.M., 2005. Lattice-Boltzmann simulations of low-Reynolds-number flow past mono- and bidisperse arrays of spheres: results for the permeability and drag force. J. Fluid Mech. 528, 233–254.

Wang, J., van der Hoef, M.A., Kuipers, J.A.M., 2009. Why the two-fluid model fails to predict the bed expansion characteristics of Geldart A particles in gas-fluidized beds: a tentative answer. Chem. Eng. Sci. 64, 622–625.

Wen, C.Y., Yu, Y.H., 1966. Mechanics of fluidization. Chem. Eng. Prog. Symp. Ser. 62, 100–111.

Xu, B.H., Yu, A.B., 1997. Numerical simulation of the gas-solid flow in a fluidized bed by combining discrete particle method with computational fluid dynamics. Chem. Eng. Sci. 52, 2785–2809.

Zhou, Z.Y., Zhu, H.P., Yu, A.B., Wright, B., Zulli, P., 2008. Discrete particle simulation of gas-solid flow in a blast furnace. Comput. Chem. Eng. 32, 1760–1772.

Paper V

CFD–DEM simulation of biomass gasification with steam in a fluidized bed reactor

Xiaoke Ku, Tian Li, Terese Løvås

Chemical Engineering Science, 122, 270−283, 2015

Chemical Engineering Science 122 (2015) 270–283

Contents lists available at ScienceDirect

Chemical Engineering Science

journal homepage: www.elsevier.com/locate/ces

CFD–DEM simulation of biomass gasification with steam in a fluidized bed reactor

Xiaoke Ku*, Tian Li, Terese Løvås

Department of Energy and Process Engineering, Norwegian University of Science and Technology (NTNU), 7491 Trondheim, Norway

HIGHLIGHTS

- A CFD–DEM model is developed to simulate the biomass gasification in a FB reactor.
- Higher temperatures are favorable for the products in endothermic reactions.
- H_2 and CO_2 concentrations increase with the increase of steam/biomass mass ratio.
- Carbon conversion decreases as the height of fuel injection point increases.
- The calculated results compare well with the experimental data.

ARTICLE INFO

Article history:
Received 4 June 2014
Received in revised form
18 August 2014
Accepted 20 August 2014
Available online 27 August 2014

Keywords:
CFD–DEM
Biomass gasification
Steam
Fluidized bed reactor
Syngas
Carbon conversion

ABSTRACT

A comprehensive CFD–DEM numerical model has been developed to simulate the biomass gasification process in a fluidized bed reactor. The methodology is based on an Eulerian–Lagrangian concept, which uses an Eulerian method for gas phase and a discrete element method (DEM) for particle phase. Each particle is individually tracked and associated with multiple physical (size, density, composition, and temperature) and thermo-chemical (reactive or inert) properties. Particle collisions, hydrodynamics of dense gas-particle flow in fluidized beds, turbulence, heat and mass transfer, radiation, particle shrinkage, pyrolysis, and homogeneous and heterogeneous chemical reactions are all considered during biomass gasification with steam. A sensitivity analysis is performed to test the integrated model's response to variations in three different operating parameters (reactor temperature, steam/biomass mass ratio, and biomass injection position). Simulation results are analyzed both qualitatively and quantitatively in terms of particle flow pattern, particle mixing and entrainment, bed pressure drop, product gas composition, and carbon conversion. Results show that higher temperatures are favorable for the products in endothermic reactions (e.g. H_2 and CO). With the increase of steam/biomass mass ratio, H_2 and CO_2 concentrations increase while CO concentration decreases. The carbon conversion decreases as the height of injection point increases owing to both an increase of solid entrainment and a decrease of particle residence time and particle temperature. Meanwhile, the calculated results compare well with the experimental data available in the literature. This indicates that the proposed CFD–DEM model and simulations are successful and it can play an important role in the multi-scale modeling of biomass gasification or combustion in fluidized bed reactor.

1. Introduction

Due to the limited supply of conventional fossil fuels and global environmental problems, more and more attention has been paid to the renewable and clean energy technologies, among which biomass gasification is one of the most promising technologies for the efficient utilization of biomass. Biomass gasification is a complex thermo-chemical process in which biomass is converted into synthetic gas (syngas), a combination of hydrogen, carbon monoxide, and methane. The syngas could be then used as a fuel in internal combustion engines, gas turbines, or fuel cells for the production of heat, mechanical energy, or power, or as a feedstock for the synthesis of liquid fuels and chemicals. The fundamental aspects of biomass gasification have been mainly studied by experiments using lab-scale reactors (Gil et al., 1999; Qin et al., 2012; Warnecke, 2000). Among the various gasification reactors, the fluidized bed (FB) reactor presents good prospects due to its high rates of heat and mass transfer, good temperature control, and its excellent mixing properties (Kern et al., 2013; Li et al., 2004; Shen et al., 2008). In a typical FB reactor, fuel feed, together with

---

* Corresponding author. Tel.: +47 73593919.
E-mail address: xiaoke.ku@ntnu.no (X. Ku).

http://dx.doi.org/10.1016/j.ces.2014.08.045
0009-2509/© 2014 Elsevier Ltd. All rights reserved.

inert bed material (e.g. sand) which acts as heat capacitance for the fuel, are fluidized by the gasifying agents, such as air (Kim et al., 2013), steam (Song et al., 2012), pure oxygen or their combination (Meng et al., 2011). There are many physico-chemical processes within a real biomass FB reactor, such as mixing, segregation, collision, particle heat-up, drying, pyrolysis, volatile matter combustion, and char reaction with O_2/steam/CO_2. Moreover their scales are greatly separated, which results in detailed study of the entire gasification process being a challenging task.

Computational fluid dynamic (CFD) models have become more and more popular in recognizing the dense gas–solid flow dynamics (Lathouwers and Bellan, 2001; Papadikis et al., 2010; Ku et al., 2013) and chemical reactions (Ergüdenler et al., 1997; Nikoo and Mahinpey, 2008; Sadaka et al., 2002) in FB reactors. Generally, all the CFD models developed can be broadly categorized into Eulerian–Eulerian and Eulerian–Lagrangian approaches. For Eulerian–Eulerian approach, both particle and fluid phases are treated as interpenetrating continua. It can predict the macroscopic characteristics of a system with relatively low computational cost and has actually dominated the modeling of fluidization process for many years (Gerber et al., 2010; Taghipour et al., 2005; Wang et al., 2009). However, in addition to the difficulty of providing closure models for interaction terms between phases within its continuum framework, Eulerian–Eulerian approach does not recognize the discrete character of the particle phase and thus has trouble in modeling flows with a distribution of particle types and sizes. These difficulties can be naturally overcome by Eulerian–Lagrangian approach (Snider et al., 2011; Xie et al., 2013) in which the gas is treated as continuous and particle as discrete phase. When the particle phase is solved by discrete element method (DEM), the Eulerian–Lagrangian approach is also called CFD–DEM model. For CFD–DEM model, each particle is individually tracked and can be composed of multiple physical (size, density, composition, and temperature) and thermo-chemical (reactive or inert) properties. It can also offer detailed microscopic information at the particle level, such as particle trajectory, particle–particle and particle–fluid interaction, and transient forces acting on each particle, which is extremely difficult, even impossible to obtain by Eulerian–Eulerian approach. A crucial point when using CFD–DEM is the CPU load for particle collision monitoring as the number of particles increases. Thus, CFD–DEM simulations are often performed on the order of 10^4 particles and are mostly restricted to 2D or quasi-3D (domain width is one particle diameter) solutions. If chemical reactions are added, computation is more and more complicated and expensive. To date most of the CFD–DEM studies performed have been focused on the hydrodynamics of the isothermal fluidized bed and there have been few works on the simulation of dense gas–solid flow coupling with chemical reactions. Liu et al. (2011) used a CFD–DEM model to study char and propane combustion in a fluidized bed although their simulation conditions were strongly simplified, e.g., only 300 char particles were added at the start of simulation and there was no more fuel injection at later times. Bruchmüller et al. (2012) carried out a biomass fast pyrolysis simulation in a bubbling fluidized bed but did not take turbulence and chemical reactions into account. Gerber and Oevermann (2014) used a 2D CFD–DEM model to simulate wood gasification in a fluidized bed reactor but they used only charcoal as the bed material without any inert bed material such as sand used in ordinary experimental beds.

The aim of this study is to develop a comprehensive CFD–DEM model capable of describing dense, thermal, and *reactive* multiphase flows like biomass gasification in a fluidized bed reactor. The model described here is an extension of our previous hydrodynamic CFD–DEM model. In our earlier paper (Ku et al., 2013), an isothermal and *non-reactive* CFD–DEM model was developed and applied to a series of test cases in order to quantify its predictive capabilities. These included (i) prediction of the characteristic fluidization behaviors (bubbles or slugs) of a typical bubbling fluidized bed, (ii) comparison of the minimum fluidization velocities predicted by different researchers, and (iii) comparison of the bed pressure drops generated by various drag correlations. The above comparisons performed have validated the hydrodynamic aspect of our CFD–DEM model. As a continuation, the hydrodynamic CFD–DEM model is enlarged here to account for the dense and reacting flows including models for turbulence, heat and mass transfer, radiation, particle shrinkage, pyrolysis, and heterogeneous and homogeneous reactions. The noteworthy novelties of the present CFD–DEM model include (i) a systematic presentation of the particle governing equations and gas transport equations within the Eulerian–Lagrangian concept, (ii) modeling of multiple homogeneous and heterogeneous reactions, (iii) resolving of turbulence by a k–ε model, (iv) 4×10^4 sand particles used as inert bed material and inter-particle and particle–wall collisions being resolved by a soft-sphere collision model, and (v) continuous biomass injection throughout the total simulation time. The integrated model is then applied to biomass gasification with steam in a lab-scale fluidized bed reactor. Simulation results are analyzed both qualitatively and quantitatively in terms of particle flow pattern, particle mixing and entrainment, bed pressure drop, composition distributions of product gas and other important characteristics in a fluidized bed reactor at different operating conditions (e.g. reactor temperature, steam/biomass mass ratio, biomass injection position). Besides, comparisons between calculated results and experimental data available in the literature are also carried out in order to verify the model.

This paper is organized as follows: In Section 2, the governing equations describing evolution of the particles and gas phase are firstly formulated. Herein, the sub-models of pyrolysis, char gasification, particle shrinkage, and gas phase reactions are also presented. In Section 3, the simulation setup is tabulated. In Section 4, the numerical results of biomass gasification with steam in a fluidized bed reactor are presented. Here, we first investigate the fluidization behavior, particle entrainment, and bed pressure drop. Then effects of different operating conditions, such as reactor temperature, steam/biomass mass ratio and biomass injection position, on the composition distributions of product gas and carbon conversion are documented where the CFD–DEM model is verified by comparing the calculated results with experimental data. Finally, a short summary and conclusions are given in Section 5. In addition, the symbols and subscripts used in the equations and abbreviations are described in the nomenclature at the end of the paper.

2. Mathematical modeling

The CFD–DEM model is formulated based on an unsteady-state Eulerian–Lagrangian multiphase model meaning transport equations are solved for the continuous gas phase and each of discrete particles is tracked through the calculated gas field. The interaction between the continuous phase and the discrete phase is taken into account by treating the exchange of mass, momentum and energy between the two systems as source terms in the governing equations. Specifically, the mechanisms of mass and energy exchange are adopted from the work of Kumar and Ghoniem (2012) with certain modifications as will be outlined below. Furthermore, for momentum exchange, detailed implementation issues are available in our earlier publication (Ku et al., 2013).

2.1. Discrete particle phase

The discrete particle phase consists of sand and biomass particles which are modeled in a Lagrangian manner. Sand plays only the role of heat carrier in biomass gasification without taking part in any reactions, whereas biomass undergoes successive physical and chemical processes such as heat-up, drying, pyrolysis, and gasification and its behavior is strongly related to operating conditions.

2.1.1. Particle motion

The governing mass, momentum, and energy equations for each particle are as follows,

Mass:

$$\frac{dm_{\mathrm{p}}}{dt}=\frac{dm_{\mathrm{vapor}}}{dt}+\frac{dm_{\mathrm{devol}}}{dt}+\frac{dm_{\mathrm{C-CO_2}}}{dt}+\frac{dm_{\mathrm{C-H_2O}}}{dt} \tag{1}$$

Momentum:

$$m_{\mathrm{p}}\frac{d\mathbf{v}_{\mathrm{p}}}{dt}=\mathbf{f}_{\mathrm{g}}+\mathbf{f}_{\mathrm{c}}+m_{\mathrm{p}}\mathbf{g} \tag{2}$$

$$I_{\mathrm{p}}\frac{d\boldsymbol{\omega}_{\mathrm{p}}}{dt}=\mathbf{T}_{\mathrm{p}} \tag{3}$$

$$\mathbf{f}_{\mathrm{g}}=\frac{V_{\mathrm{p}}\beta}{\varepsilon_{\mathrm{p}}}(\mathbf{u}_{\mathrm{g}}-\mathbf{v}_{\mathrm{p}}) \tag{4}$$

$$\beta=\begin{cases}150\frac{\varepsilon_p^2\mu_g}{\varepsilon_g^2 d_p^2}+1.75\frac{\varepsilon_p\rho_g}{\varepsilon_g d_p}|\mathbf{u}_g-\mathbf{v}_p| & \varepsilon_{\mathrm{g}}<0.8\\ \frac{3}{4}C_d\frac{\varepsilon_p\rho_g}{d_p}|\mathbf{u}_g-\mathbf{v}_p|\varepsilon_g^{-2.65} & \varepsilon_{\mathrm{g}}\geq 0.8\end{cases} \tag{5}$$

$$C_{\mathrm{d}}=\begin{cases}\frac{24}{Re_{\mathrm{p}}}(1+0.15Re_{\mathrm{p}}^{0.687}) & Re_{\mathrm{p}}<1000\\ 0.44 & Re_{\mathrm{p}}\geq 1000\end{cases} \tag{6}$$

$$Re_{\mathrm{p}}=\varepsilon_{\mathrm{g}}\rho_{\mathrm{g}}d_{\mathrm{p}}|\mathbf{u}_{\mathrm{g}}-\mathbf{v}_{\mathrm{p}}|/\mu_{\mathrm{g}} \tag{7}$$

Energy:

$$m_{\mathrm{p}}c_{\mathrm{p}}\frac{dT_{\mathrm{p}}}{dt}=hA_{\mathrm{p}}(T_{\mathrm{g}}-T_{\mathrm{p}})+\frac{e_{\mathrm{p}}A_{\mathrm{p}}}{4}(G-4\sigma T_{\mathrm{p}}^4)+Q_{\mathrm{p}} \tag{8}$$

As shown in Eq. (2), $\mathbf{f}_{\mathrm{c}}$, i.e. the total contact force acting on particle due to inter-particle or particle–wall collisions, is taken into account and it is necessary for dense gas-particle flows. This is different from the model of Kumar and Ghoniem (2012) which does not consider the contact forces and thus their model is only applicable to dilute multiphase systems.

Here, the inter-phase momentum exchange coefficient β is modeled via the well-known Gidaspow drag correlation (Gidaspow, 1994). As shown in Eq. (5), the Gidaspow model combines Ergun (1952) and Wen and Yu (1966) correlations for the dilute and dense granular regime where a porosity ε_{g} of 0.8 is adopted as the boundary between these two regimes. This model is often used in the literature and effects of using different drag models were discussed in earlier publication (Ku et al., 2013).

As shown in Eq. (8), the particle temperature is calculated taking into account the heat transfer due to convection, radiation, and source term Q_{p} including both the latent heat of vaporization of water from the particle to the gas phase and the heat generated by the heterogeneous char reactions.

The inter-particle or particle–wall collisions are resolved by a soft-sphere discrete element method which was firstly proposed by Cundall and Strack (1979). In this method, the inter-particle contact forces are calculated using equivalent simple mechanical elements, such as spring, slider and dashpot (see Fig. 1). Particles are allowed to overlap slightly. The normal force tending to repulse the particles can then be deduced from this spatial overlap and the normal relative velocity at the contact point. The spring stiffness can be calculated by Hertzian contact theory when the physical properties such as Young's modulus and the Poisson ratio are known. A characteristic feature of the soft-sphere model is that it is capable of handling multiple particle–particle contacts which is of much importance when modeling dense particle systems like fluidized bed. Detailed implementation issues of the soft-sphere model are available in the literature (e.g. Tsuji et al., 1992), which are not stated here for the sake of shortness. In this study, the following physical properties are adopted for the collision model: Young's modulus is 5×10^6 Pa; Poisson ratio is 0.3; coefficient of restitution and friction coefficient are 0.9 and 0.3, respectively. All values are equally valid for walls and particles (Bruchmüller et al., 2012; Ku et al., 2013).

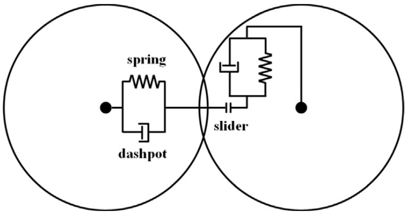

Fig. 1. The spring–slider–dashpot collision model.

2.1.2. Pyrolysis

As soon as fresh biomass is fed into the bottom of the hot sand bed, it is immediately heated up, and thereby the devolatilization and pyrolysis of biomass as well as char gasification occurs. The pyrolysis compositions released from biomass can be expressed by the following equilibrium equation and each product yield is solved with the help of the elemental conservation analysis.

$$\mathrm{Biomass}\rightarrow\alpha_1\mathrm{CO}+\alpha_2\mathrm{H_2O}+\alpha_3\mathrm{CO_2}+\alpha_4\mathrm{H_2}+\alpha_5\mathrm{CH_4}+\alpha_6\mathrm{char(s)}+\alpha_7\mathrm{ash(s)},\ \sum_i\alpha_i=1 \tag{9}$$

Note that, in the present model, reactions with sulfur and nitrogen are not taken into account due to their little amount (see Table 3), and they are considered passing directly to ash. CH_4 is the only hydrocarbon species taken into consideration. Although C_2H_2, C_2H_4, C_2H_6, and other higher hydrocarbons (tar) are produced in the pyrolysis process, they are treated as non-stable products and this mechanism has also been widely used by other researchers (Ergüdenler et al., 1997; Gerber et al., 2010).

Consistent with Abani and Ghoniem's work (Abani and Ghoniem, 2013), the devolatilization rate is modeled using a single step first-order Arrhenius reaction.

$$\frac{dm_{\mathrm{devol}}}{dt}=-A\exp\left(-\frac{E}{RT_{\mathrm{p}}}\right)m_{\mathrm{devol}} \tag{10}$$

where m_{devol} is the mass of the volatiles remaining in the particle, $A=5.0\times10^6\ \mathrm{s}^{-1}$, and $E=1.2\times10^8$ J/kmol (Prakash and Karunanithi, 2008). The devolatilization process is assumed to be energetically neutral because the heat of devolatilization is generally negligible as compared to heat of reactions due to char consumption reactions (Abani and Ghoniem, 2013).

2.1.3. Char conversion chemistry

After devolatilization, the biomass particle is left with char and ash. Ash is assumed to be carried along with the particle without taking part in any reactions. Char will react in the presence of carbon dioxide and steam and gets converted into carbon monoxide and hydrogen. The following heterogeneous reactions are assumed and implemented in OpenFOAM.

$$\mathrm{C}+\mathrm{CO_2}\rightarrow2\mathrm{CO} \tag{R1}$$

$$\mathrm{C}+\mathrm{H_2O}\rightarrow\mathrm{CO}+\mathrm{H_2} \tag{R2}$$

Reactions R1 and R2 are endothermic gasification reactions and R1 is known as the Boudouard reaction.

The char consumption rate which includes the effects of both diffusion and kinetic rates is given as

$$\frac{dm_{C-i}}{dt} = -A_p p_i \frac{r_{\text{diff},i} r_{\text{kin},i}}{r_{\text{diff},i} + r_{\text{kin},i}} \tag{11}$$

$$r_{\text{diff},i} = C_i \frac{[(T_p + T_g)/2]^{0.75}}{d_p} \tag{12}$$

$$r_{\text{kin},i} = A_i T_p \exp\left(\frac{-E_i}{RT_p}\right) \tag{13}$$

where m_{C-i} is the mass of the char remaining in the particle when char reacts with gasifying species i ($=CO_2$, or H_2O), p_i is the partial pressure of the gasifying species, $r_{\text{diff},i}$ and $r_{\text{kin},i}$ are the diffusion rate and the kinetic rate, respectively. C_i is the mass diffusion rate constant. A_i and E_i are the parameters typical of the Arrhenius forms of kinetic rates. For wood biomass considered in the present study, the constants used for kinetic and diffusion rates are assembled below in Table 1 (Abani and Ghoniem, 2013).

Table 1
Heterogeneous reaction constants.

Parameters	Values
A_{H_2O} (s/(m K))	45.6
E_{H_2O} (J/kmol)	4.37×10^7
A_{CO_2} (s/(m K))	8.3
E_{CO_2} (J/kmol)	4.37×10^7
C_i (i=H_2O, CO_2) (s/$K^{0.75}$)	5.0×10^{-12}

2.1.4. Particle shrinkage

The char–gas chemistry consumes the solids and biomass particles shrink as they react with the gas phase. Particle shrinkage not only has an effect on gasification but also strongly affects particle trajectory on its way out of the reactor. Without particle shrinkage char entrainment will be highly over-predicted. Here we assume that particle density (ρ_p) stays constant throughout the gasification process and a mass-proportional shrinkage is adopted for each biomass particle. Thus the diameter of biomass particle shrinks as follows (Bruchmüller et al., 2012),

$$d_p = \left(\frac{6m_p}{\pi\rho_p}\right)^{1/3} \tag{14}$$

2.2. Continuous gas phase

The gas phase is modeled as a continuum, known as an Eulerian type model.

2.2.1. Gas phase motion

For continuum gas phase, the governing mass, momentum, energy, and species transport equations can be typically represented by the following equations.

Mass:

$$\frac{\partial}{\partial t}(\varepsilon_g \rho_g) + \nabla\cdot(\varepsilon_g \rho_g \mathbf{u}_g) = S_{p,m} \tag{15}$$

Momentum:

$$\frac{\partial}{\partial t}(\varepsilon_g \rho_g \mathbf{u}_g) + \nabla\cdot(\varepsilon_g \rho_g \mathbf{u}_g \mathbf{u}_g) = -\nabla p + \nabla\cdot(\varepsilon_g \boldsymbol{\tau}_{\text{eff}}) + \varepsilon_g \rho_g \mathbf{g} + S_{p,\,\text{mom}} \tag{16}$$

Energy:

$$\frac{\partial}{\partial t}(\varepsilon_g \rho_g E) + \nabla\cdot(\varepsilon_g \mathbf{u}_g(\rho_g E + p)) = \nabla\cdot(\varepsilon_g \alpha_{\text{eff}} \nabla h_s) + S_h + S_{p,h} + S_{\text{rad}} \tag{17}$$

$$E = h_s - \frac{p}{\rho_g} + \frac{u_g^2}{2} \tag{18}$$

Species:

$$\frac{\partial}{\partial t}(\varepsilon_g \rho_g Y_i) + \nabla\cdot(\varepsilon_g \rho_g \mathbf{u}_g Y_i) = \nabla\cdot(\varepsilon_g \rho_g D_{\text{eff}} \nabla Y_i) + S_{p,Y_i} + S_{Y_i} \tag{19}$$

Note that the above transport equations have taken the volume fraction of gas ε_g into account and are applicable to the dense and reactive gas–particle flow in fluidized beds studied in this paper. They are different from the ones of Kumar and Ghoniem (2012) which do not consider ε_g and are only suitable for very dilute gas–particle flows.

Here, the effective stress tensor, $\boldsymbol{\tau}_{\text{eff}}$, is the sum of the viscous and turbulent stresses. Similarly the effective dynamic thermal diffusivity α_{eff} and mass diffusion coefficient for species D_{eff} take both the viscous and turbulent contributions into account. P-1 radiation model is adopted to solve the radiation source term S_{rad} as it has generally been chosen in CFD simulations of pulverized fuel gasification with radiation scattering (Backreedy et al., 2006).

As shown by Eq. (19), a transport equation is solved for each gas species, and the total gas phase properties are calculated from the mass fractions of the gas species making up the gas mixture. The mass, momentum, and enthalpy Eqs. (15), (16) and (17), respectively, are solved at each time step for the gas mixture. The flow is compressible, and the gas phase pressure, volume, temperature, and density are related through equations of state.

In order to solve turbulence, the governing transport equations for k and ε, which take into account the volume fraction of gas ε_g and are suitable for our dense gas–particle simulation system, are as follows (Kumar and Ghoniem, 2012, Wang et al., 2009),

$$\frac{\partial}{\partial t}(\varepsilon_g \rho_g k) + \nabla\cdot(\varepsilon_g \rho_g \mathbf{u}_g k) = \nabla\cdot\left(\varepsilon_g\left(\mu_g + \frac{\mu_t}{\sigma_k}\right)\nabla k\right) + \varepsilon_g G_k - \varepsilon_g \rho_g \varepsilon \tag{20}$$

$$\frac{\partial}{\partial t}(\varepsilon_g \rho_g \varepsilon) + \nabla\cdot(\varepsilon_g \rho_g \mathbf{u}_g \varepsilon) = \nabla\cdot\left(\varepsilon_g\left(\mu_g + \frac{\mu_t}{\sigma_\varepsilon}\right)\nabla \varepsilon\right) + \varepsilon_g \frac{\varepsilon}{k}(C_{\varepsilon 1} G_k - C_{\varepsilon 2} \rho_g \varepsilon) \tag{21}$$

The constants $C_{\varepsilon 1}=1.44$, $C_{\varepsilon 2}=1.92$, $\sigma_k=1.0$, and $\sigma_\varepsilon=1.3$. The turbulent viscosity μ_t is computed as a function of k and ε,

$$\mu_t = \rho_g C_\mu \frac{k^2}{\varepsilon} \tag{22}$$

where C_μ is a constant which is set as 0.09.

2.2.2. Gas phase reactions

There are hundreds of gas phase chemical reactions in a gasification reactor. Even if all the elemental reactions and their rates of reaction could be identified, it is not possible to calculate so large number of coupled reactions. For the sake of simplification, a reduced set of 2 global reactions (3 reactions considering reverse reaction) is used to describe the major conversion rates in the reactor and effect of turbulence on reactions is resolved by the partially stirred reactor (PaSR) model (Abani and Ghoniem, 2013). Chemical reaction equations and their reaction rates as well as adopted references are listed in Table 2. The reaction rate is in kmol/(m^3 s), and [·] implies mole concentration (kmol/m^3) of the gas species enclosed in the brackets. Reactions R3 is the consumption of CH_4 through steam reforming. Reaction R4 is known as the reversible water–gas shift reaction. Both forward reaction rate k_f

Table 2
Considered homogeneous chemical reactions and their reaction rates.

Reactions		Reaction rate	Refs.
$CH_4+H_2O \rightarrow CO+3H_2$	(R3)	$k=3.0\times10^8[CH_4][H_2O]\exp(-1.26\times10^8/RT)$	Jones and Lindstedt (1988)
$CO+H_2O \leftrightarrow CO_2+H_2$	(R4)	$k_f=2.78\times10^3[CO][H_2O]\exp(-1.26\times10^7/RT)$	Gómez-Barea and Leckner (2010)
		$k_b=9.59\times10^4[CO_2][H_2]\exp(-4.66\times10^7/RT)$	
		$k_{eq}=0.029\exp(3.40\times10^7/RT)$	

and reverse reaction rate k_b of R4 are calculated in lieu of a combined forward–reverse rate and k_f and k_b are related by the equilibrium constant $k_{eq}=k_f/k_b$.

2.3. *Computational methodology*

Since the governing equations for particles and the gas phase are different, different solution schemes have to be used. For discrete particles, a first-order Euler time integration scheme is used to solve the translational and rotational motions of particles. Inter-particle and particle–wall collisions are modeled by soft-sphere collision method (see Fig. 1), where the solution scheme is well documented in the literature (e.g. Tsuji et al., 1992). Meanwhile, the drying, pyrolysis, and gasification submodels update particle properties like temperature, diameter, composition, and heat capacity at each fluid time step. For continuous gas phase, time discretization of the transporting equations is based on an Euler scheme and spatial discretization uses a finite-volume technique. The coupling between the discrete particles and the gas phase is achieved by the inter-phase source terms ($S_{p,m}$, $S_{p,mom}$, $S_{p,h}$, $S_{p,Yi}$), which are solved at every fluid time step. All mathematical models and schemes described above have been developed and implemented into an open source C++ toolbox OpenFOAM (OpenCFD Ltd, 2012). The codes are made parallel and each case shown in the following sections takes about 14 days running time on a 16-core Intel node to accomplish the 20 s real time of simulation.

3. Simulation setup

All calculations are performed on a lab-scale biomass fluidized bed reactor which is taken from the experimental study of Song et al. (2012). Fig. 2 shows a sketch of the simulated geometry. It consists of a rectangular container of dimensions 0.23 m (width) × 1.5 m (height) × 0.0015 m (thickness) with a orifice of 0.01 m in width at the center of the bottom wall. The left, right, bottom walls, the bottom orifice and the top outlet compose the whole calculation domain boundaries. Initially, the reactor is filled completely with N_2 and a packed sand bed which is composed of 40,000 spherical sand particles with a diameter of 1.5 mm. The initial temperature of the sand and the gas in the domain is set equal to the operating reactor temperature (T_r). Hence, although the sand bed is initially stationary, it is assumed that it has been preheated. At the bottom inlet, mass flow rates for gas and biomass are specified, respectively. At the walls, no-slip conditions are applied for the gas phase and the wall temperature is specified according to the operating reactor temperature. At the top outlet, the atmospheric pressure boundary condition is adopted and particles are allowed to exit the computational domain during the simulation, modeling a fine solids entrainment phenomenon.

In the simulations, biomass is fed through the bottom orifice, together with a mixture of steam and nitrogen which is used as the gasifying agent as well as the fluidizing gas. The initial diameter of biomass particle is 1.5 mm which is taken from the experiment. Pine wood is used as the biomass fuel and its initial properties, such as proximate and elemental analyses, are given in Table 3. The operating conditions such as reactor temperatures (T_r), biomass feed rate, and steam/biomass mass ratio (S/B), are in accordance with Song et al.'s (2012) experiment data. Table 4 summarizes the parameter settings used in the simulation and the boundary conditions for the gas phase are listed in Table 5. Note that all simulation cases are performed with a bottom biomass injection (see Fig. 2) except in Subsection 4.6. "Effect of biomass

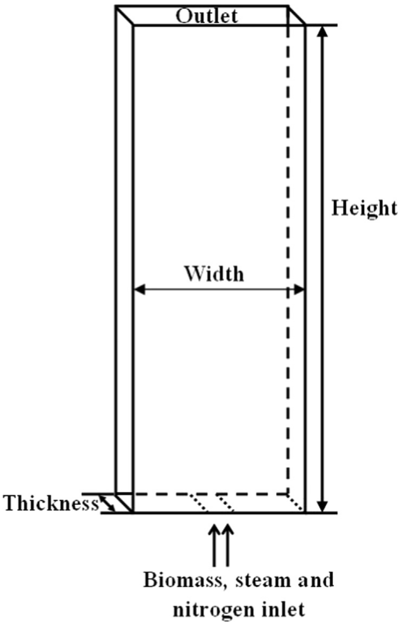

Fig. 2. Geometry of the fluidized bed reactor.

Table 3
Pine wood properties (Song et al., 2012).

Proximate analysis (wt%, *on the as-received basis*)		Elemental analysis (wt%, *on the daf basis*)	
Moisture	11.89	C	46.29
Ash	1.56	H	6.48
Volatile	71.78	O	46.08
Fixed carbon	14.77	N&S	1.15

Table 4
Parameter settings for the simulation system.

Property	Value	Property	Value
Bed size, (m)	0.23 × 1.5 × 0.0015	Sand density, (kg/m^3)	2600
Reactor temperature, (°C)	820, 870, 920	Sand specific heat, (J/(kg K))	860
CFD cell size, (m)	0.01 × 0.02 × 0.0015	Sand number, (dimensionless)	40,000
Fluid time step, (s)	1.0×10^{-5}	Biomass type, (dimensionless)	pine
Total simulation time, (s)	20	Initial biomass diameter, (mm)	1.5
Particle shape, (dimensionless)	Spherical	Biomass density, (kg/m^3)	470
Collision restitution coefficient, (dimensionless)	0.9	Biomass specific heat, (J/(kg K))	1500
Particle friction coefficient, (dimensionless)	0.3	Biomass feed rate, (g/s)	0.03125
Solid emissivity, (dimensionless)	0.9	Gas density, ρ_g	*
Sand diameter, (mm)	1.5	Inlet gas flow rate, (g/s)	0.18935

* ρ_g is determined based on the gas equation of state.

Table 5
Boundary conditions for gas phase in the simulation.

Boundaries	Velocity	Pressure	Temperature	Porosity
Left and right walls	No slip	Zero gradient	Fixed value	Zero gradient
Bottom wall	No slip	Zero gradient	Zero gradient	Zero gradient
Inlet orifice (bottom)	Fixed flow rate	Zero gradient	Fixed value	Fixed value
Outlet (top)	Zero gradient	Fixed value	Zero gradient	Zero gradient

injection position" where the particle behaviors are compared among three different injection positions.

4. Results and discussions

4.1. Initial bed preparation

As described in Section 3, an initial packed sand bed is needed to start the fluidized bed simulation and it is generated as follows. The container is uniformly divided into a set of small rectangular lattices throughout the calculation domain. Then 40,000 sand particles with zero velocity are positioned at the centers of these lattices and allowed to fall down under the influence of gravity in the absence of inlet jet gas. As shown in Fig. 3, pluvial deposition of the particles finally results in a static bed of height about 0.35 m and porosity around 0.42. This deposited bed is then used as the initial packed bed for the fluidized bed gasification simulation. As pointed out by Xu and Yu (1997), the initial input data for this deposited bed include not only the particle coordinates but also the forces and torques which come with the deposition of particles in the packing process.

4.2. Fluidization behavior

To investigate the fluidization behavior of the bed, the formation and development of bubbles with time are firstly illustrated. Fig. 4 shows the simulated particle flow patterns with the time increment being 0.1 s at the beginning of simulation, representative for the base case (T_r=820 °C, S/B=1.2). Particles are colored by solid type. Brown color indicates sand particle and black color denotes biomass. Overally, the conditions in the reactor are almost symmetrical at the beginning of simulation. As an initial response of the bed to the introduction of fluidizing gas, a significant upward flow of particles is caused due to the instantaneous breakup of the inter-particle locking. It is readily observed that a big bubble (void structure) with an oval shape is firstly formed at the jet region (t=0.1 s), which forces particles in its front to rise. This bubble grows as gas flows upward and eventually collapses (t=0.2 s, 0.3 s). At later times, new bubbles continue to form at the bottom of bed and then they undergo the same procedure. Besides the bubble formation, the existence of "slug" structure at the upper part of the bed is also clearly predicted (t=0.4 s). The term "slug" is used here to describe a dilute region of particles which occupies the whole width of the bed and a similar definition is also given by other investigators (Hoomans et al., 1996; Kafui et al., 2002). The formation of bubbles and slugs in a typical fluidized bed reactor was also reported in the literature both numerically (Boyalakuntla, 2003; Hoomans et al., 1996; Xu and Yu, 1997) and experimentally (Tsuji et al., 1993). At t=0.40 s, a bed expansion estimated at 120% of the initial bed height is observed. Fig. 4 also shows the biomass particles (in black color), which start to enter into the reactor at t=0 through the bottom orifice, move up inside the dense sand bed.

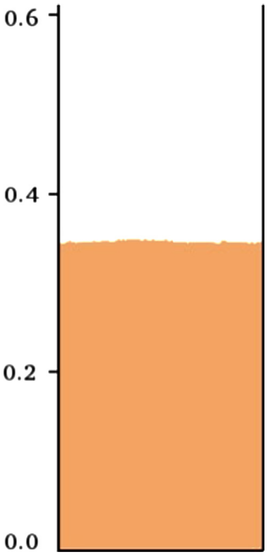

Fig. 3. Particle configurations after a simulated packing process.

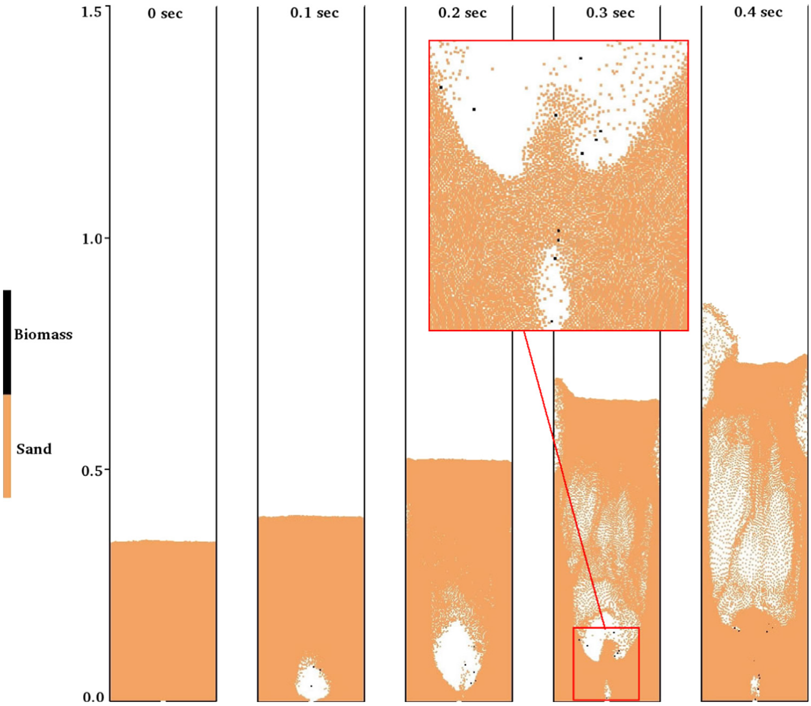

Fig. 4. Particle flow patterns with the time increment being 0.1 s at the beginning of simulation. T_r=820 °C, S/B=1.2. (For interpretation of the references to color in this figure the reader is referred to the web version of this article.)

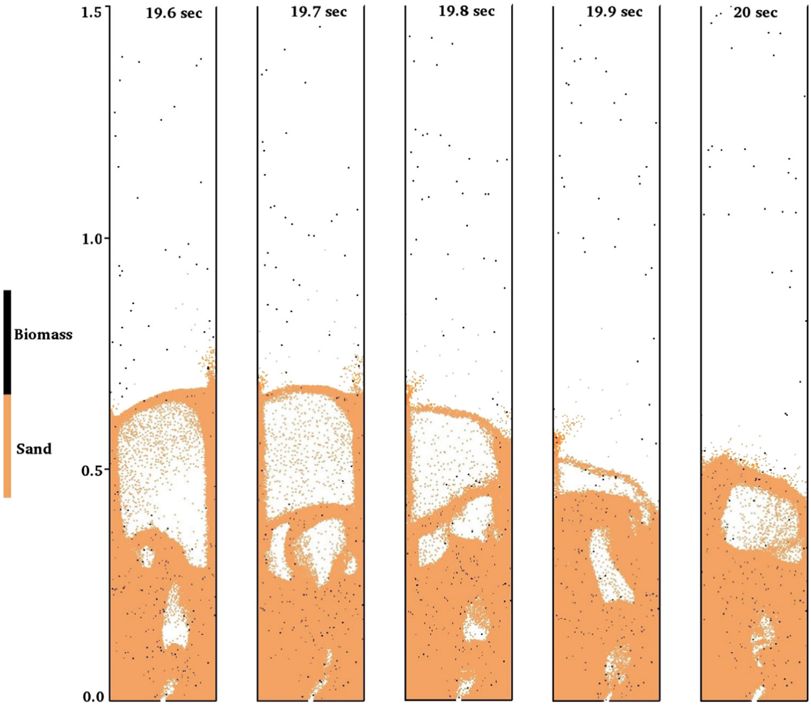

Fig. 5. Particle flow patterns with the time increment being 0.1 s at the end of simulation. T_r=820 °C, S/B=1.2.

Fig. 5 depicts the particle flow patterns with the time increment being 0.1 s at the end of simulation. Generally, due to the gas productions from biomass by pyrolysis and gasification, the conditions in the reactor are not symmetrical and the bed is in a churned-turbulent state. It is observed that the inlet jet degenerate into bubbles, which rise through the bed and grow by coalescence with other bubbles to form slugs. When bubbles and slugs burst at the bed surface, particles tend to be pushed towards the wall and then fall down along the wall. This provokes a quite vigorous fluidization and strong mixing takes place. It is easily seen that biomass particles are relatively evenly distributed throughout the dense sand bed, illustrating the effectiveness for particle mixing which is regarded as a special characteristic of fluidized beds. Good mixing favors the direct contact between virgin cold biomass and hot sand and in turn allows a good heat transfer.

Fig. 6 depicts the snapshot of particle temperatures at the end of simulation. It is easily observed that the sand particles play the role of heat carrier and they have a temperature which is very close to the operating temperature (T_r=820 °C). At the same time, the strong mixing demonstrated in Fig. 5 favors the direct contact between virgin cold biomass and hot sand and results in a quick increase in the biomass temperature, whereas most of the biomass particles still have a relatively lower temperature compared to sand particles as shown in Fig. 6.

To show the transient behavior due to the fluidization of the bed, the pressure drop across the bed Δp is plotted in Fig. 7 as a function of time t. Δp is obtained as the difference between the average gas pressure in the bottom and top rows of the computational cells. It is easily observed that Δp fluctuates with time. The bed pressure drop fluctuations in a bubbling fluidized bed are considered to be caused by bubbles and slugs that form and collapse at regular intervals (Boyalakuntla, 2003) and effects of different drag models on the bed pressure drop has been discussed in our earlier paper (Ku et al., 2013).

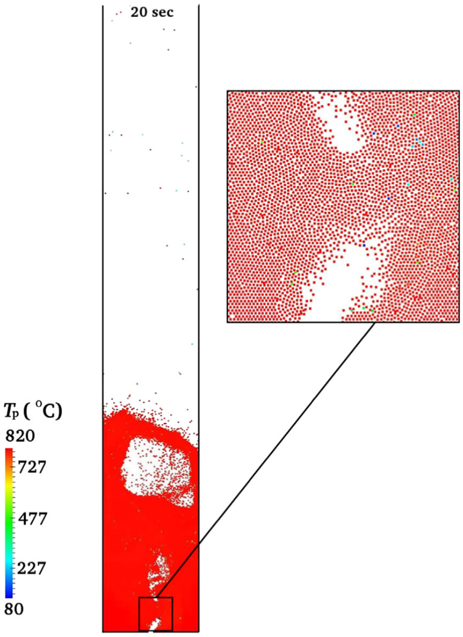

Fig. 6. Snapshot of particle temperatures at the end of simulation. T_r=820 °C, S/B=1.2.

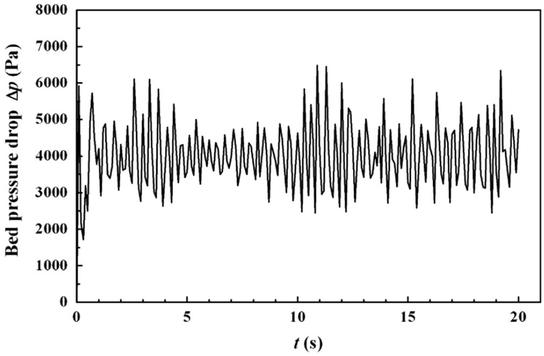

Fig. 7. Bed pressure drop Δp against time t. T_r=820 °C, S/B=1.2.

As shown in Figs. 4 and 5, the vigorous fluidization is characterized by the formation of large bubbles and slugs whose intensive eruptions can make light particles have high velocities and then reach the top outlet where they are eventually entrained out of the reactor (substantiated by snapshots at different times in Fig. 5). Fig. 8 shows the moving trajectory for a selected biomass particle before it is entrained. It is seen that, before entrainment occurs, the particle changes its moving direction and falls back (preferably near the wall) into the bed many times due to gas–particle interactions, particle–particle collisions and boundary effects near the bed top. This mechanism makes biomass particles have a long residence time in the reactor and a high carbon conversion ratio, which favors the syngas production from char gasification.

4.3. Product gas composition

For biomass gasification, H_2 and CO are the two most important product gas species. Figs. 9 and 10 illustrate the H_2 and CO mass fraction distributions in the reactor under base conditions (T_r=820 °C, S/B=1.2), respectively. It can be observed that, at the lower part of the reactor, the concentrations of H_2 and CO are high at similar locations representing regions where the biomass temperature has increased enough to produce large quantities of gas products due to devolatilization and gasification reactions. Moreover, the conditions in the reactor are not symmetrical which is also caused by the gas products from biomass by pyrolysis and gasification. From the analysis in the previous section, we know that, in a vigorous fluidized bed reactor, particles tend to migrate outwards toward the wall, driven by gas–particle interactions, particle–particle collisions and boundary effects, and then descend along the wall. As a result, there is a higher concentration of particles in the wall region where H_2 and CO concentrations are augmented as shown in Figs. 9 and 10. At the upper part of the reactor, the almost homogeneities in the mass fractions of H_2 and CO are a result of both the lower particle concentration and the gas transport process in the reactor.

Fig. 11 shows the volume fractions of the product gas compositions at the reactor outlet as a function of time t for the base case (T_r=820 °C, S/B=1.2). Note that the calculated results are based on the dry and N_2 free gas, which is consistent with the experimental study of Song et al. (2012). It is observed that there is only a strong dependence of product gas compositions on t in the initial period of simulation ($t < 5$ s). After the initial period ($t > 5$ s), each composition reaches a quasi-steady state. Thus in the following

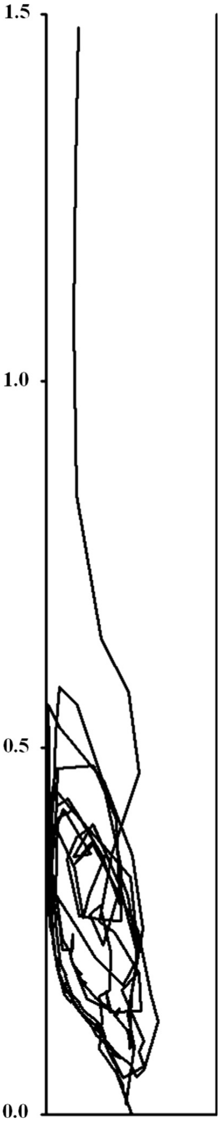

Fig. 8. Moving trajectory for a selected biomass particle before it is entrained out of the reactor. T_r=820 °C, S/B=1.2.

sections, all the quantitative results are on a time-average basis from t=5 s to 20 s.

4.4. *Effect of reactor temperature*

Operating rector temperature (T_r) plays an important role in biomass gasification. Fig. 12 shows comparisons of the calculated results with the experimental data of Song et al. (2012) for product gas composition versus reactor temperature in the range of 820–920 °C. The steam/biomass mass ratio (S/B) is fixed at 1.2. It can be observed that, the predictions of the model show good conformance to the experimental measurements. For the two most important syngas species (H_2, CO), the minimum relative error of calculation to experiment is about 1% and the maximum relative error is less than 25%. For CO_2, the maximum relative error is also within 30%. The underestimation of CH_4 can be attributed to the simplification of pyrolysis model and the neglect of tar and methanation reaction. Considering there exist no complete and unified set of gasifier chemistry equations and reaction rates in the open literature, errors cannot be avoided. This implies that the present CFD–DEM simulations are reasonable and the validity of the integrated model is verified.

The product gas composition is the result of the combination of a series of complex and competing reactions, as given in reactions (R1–R4). Generally speaking, higher temperature favors the products in endothermic reactions. Those endothermic reactions include the Boudouard (R1), the (R2) and the methane-steam reforming reaction (R3). Thus reactions (R1)–(R3) are strengthened with an increase in the reactor temperature, which result in an increase of CO and a decrease of CO_2 and CH_4 in the product gas. For H_2, on the one hand, high temperature is in favor of H_2 formation owing to endothermic reactions (R2) and (R3). On the other hand, the temperature increase impels the exothermic water–gas shift reaction (R4) toward the negative direction at the expense of H_2. Therefore, the trend of H_2 content with increasing temperature is governed by the competing reactions (R2)–(R4). As shown in Fig. 12, H_2 content slightly decreases with an increase in the reactor temperature for the experiment, while it is not very sensitive to the temperature change for the simulation.

4.5. *Effect of steam/biomass mass ratio*

The effect of steam/biomass mass ratio (S/B) on the product gas composition at the reactor temperature of 820 °C is shown in Fig. 13. Again, the calculated exit gas compositions are in a good agreement with the experiment. With the increase of S/B, H_2 and CO_2 concentrations increase while CO concentration decreases. This can be mainly explained by water–gas shift reaction (R4) and high S/B boosts the forward reaction of (R4). Furthermore, due to methane-steam reforming reaction (R3), slightly decreasing trend of CH_4 composition with S/B is observed.

4.6. *Effect of biomass injection position*

Biomass injection position is another important parameter for design purposes. Fig. 14 shows the effect of three different injection points on the biomass particle distributions. For clarity purpose, the sand particles are excluded in the figure. As shown in Fig. 14, besides the default bottom feed point (Feed1), two other feed points, Feed2 and Feed3, are created at the left side wall and located at 0.2 m and 0.6 m above the bottom of the reactor, respectively. Feed2 denotes a point at the lower part of the sand bed and Feed3 represents a point just above or near the top of the sand bed. Therefore, the three feeding points adopted covers both bottom and top feeding of fuel which are commonly used in practical applications.

Fig. 14 shows that, for Feed1 and Feed2, no significant difference related to biomass particle distributions is observed except for a small local accumulation of biomass close to Feed2 position. However, for Feed3 where biomass is injected near the sand bed surface, the relatively low density of biomass precludes its good mixing with the sand bed and more biomass particles tend to be in the freeboard and then have a higher probability of being entrained out of the reactor.

Fig. 15 depicts the average biomass particle temperature for the three different injection points. Specifically, the values of particle temperature for the Feed1, Feed2, and Feed3 are 692.3 °C, 686.9 °C, and 661.3 °C, respectively. As expected, Feed1 has the highest biomass particle temperature due to its best mixing performance.

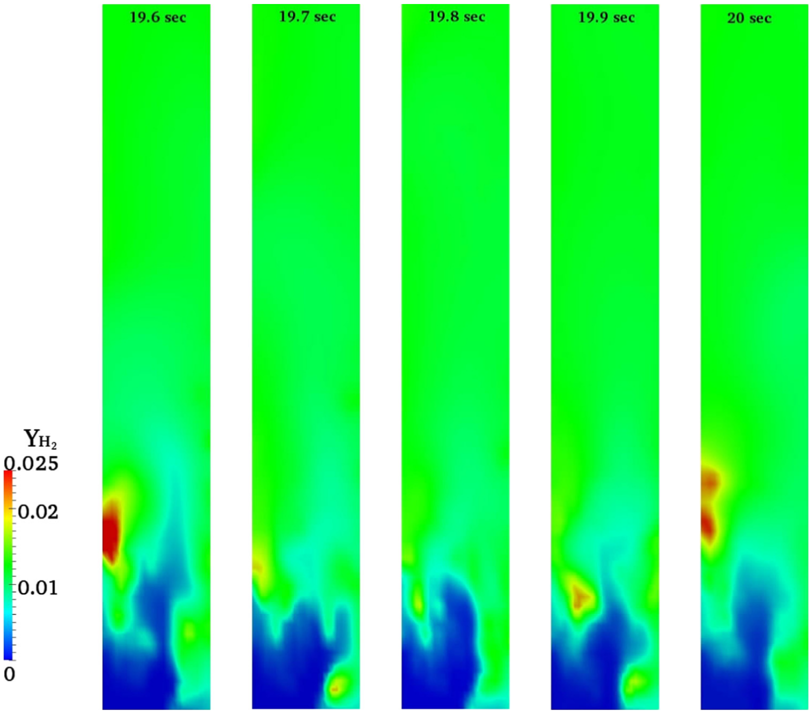

Fig. 9. Snapshots of H_2 mass fractions with the time increment being 0.1 s at the end of simulation. T_r=820 °C, S/B=1.2.

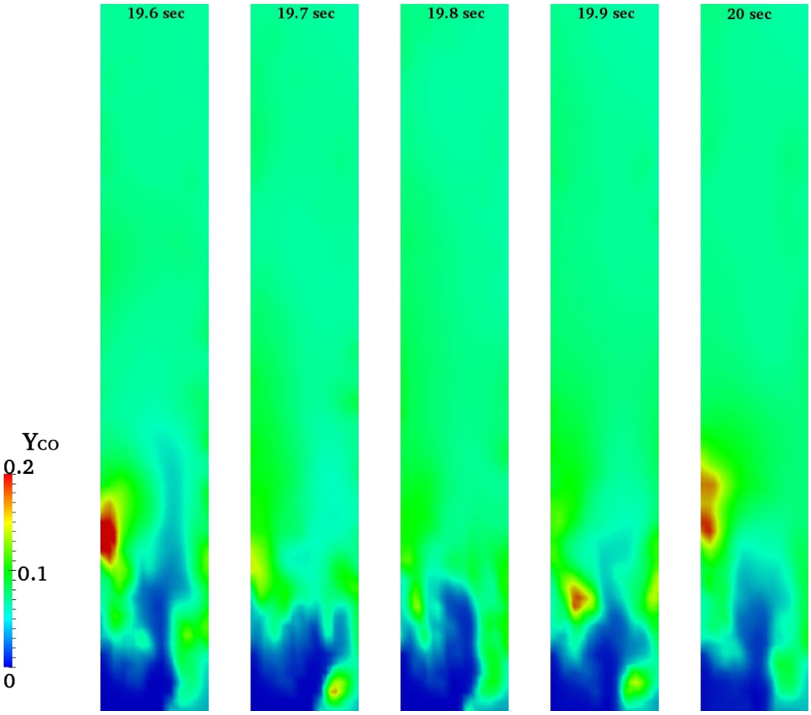

Fig. 10. Snapshots of CO mass fractions with the time increment being 0.1 s at the end of simulation. T_r=820 °C, S/B=1.2.

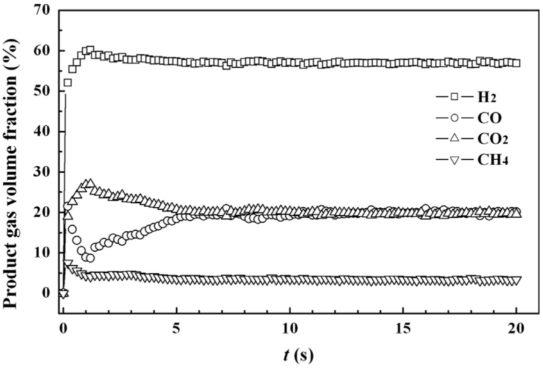

Fig. 11. Temporal evolution of product gas volume fractions at the reactor outlet. T_r=820 °C, S/B=1.2.

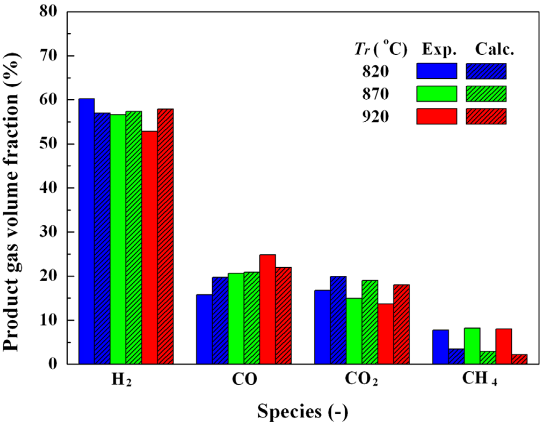

Fig. 12. Effect of reactor temperature on product gas composition at the reactor outlet. S/B=1.2.

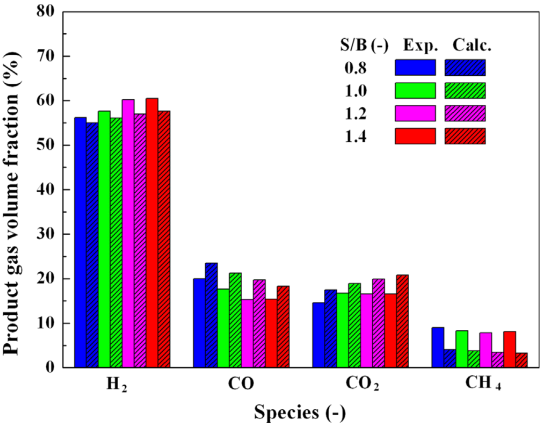

Fig. 13. Effect of steam/biomass mass ratio on product gas composition at the reactor outlet. T_r=820 °C.

Fig. 16 shows the average moisture content of biomass particles for the three different injection points. It can be seen that the moisture content is very low for all three injection positions because the vaporization process occurs at a very fast rate due to the high operating temperature (T_r=820 °C). Specifically, the values of moisture content for the Feed1, Feed2, and Feed3 are 0.07%, 0.10%, and 0.20%, respectively. Again, as expected, Feed3 has the highest moisture content due to its worst mixing performance which in turn results in a lowest biomass particle temperature as shown in Fig. 15.

Carbon conversion (CC) is a vital index used for evaluating the performance of gasification. It is defined as follows (Chen et al., 2013),

$$CC\ (\%) = \frac{\dot{m}_{out,CO} 12/28 + \dot{m}_{out,CO_2} 12/44 + \dot{m}_{out,CH_4} 12/16}{\dot{m}_{in,fuel} Y_c} \times 100 \tag{23}$$

where Y_c is the mass fraction of carbon in the feed fuel (biomass).

Fig. 17 shows the CC at the reactor outlet for the three injection points. Specifically, the values of CC for the Feed1, Feed2, and Feed3 are 95.3%, 94.9%, and 86.7%, respectively. The CC decreases as the height of injection point increases owing to both an increase of solid entrainment and a decrease of particle residence time and particle temperature (see Figs. 14 and 15).

5. Conclusions

A comprehensive CFD–DEM numerical model has been developed to simulate the biomass gasification process in a fluidized bed reactor. The gasifying agent is steam. The methodology is based on an Eulerian–Lagrangian concept, which uses an Eulerian method for gas phase and a discrete element method for particle phase. Each particle is individually tracked and associated with a range of physical and thermo-chemical properties, making it possible to look at accurate and detailed multi-scale information (i.e., any desired particle property, trajectory, and particle interaction) over the entire particle life time. The integrated model further considers particle collisions, hydrodynamics of dense gas–particle flow in fluidized beds, turbulence, heat and mass transfer, radiation, particle shrinkage, pyrolysis, as well as homogeneous and heterogeneous chemical reactions. The interaction between the continuous gas phase and the discrete particle phase is also considered by treating the exchange of mass, momentum and energy between the two systems as source terms in the governing equations.

Effects of different operating conditions, such as reactor temperature, steam/biomass mass ratio, and biomass injection position, on the gasification performance are analyzed. Simulation results are analyzed both qualitatively and quantitatively in terms of particle flow pattern, particle mixing and entrainment, bed pressure drop, product gas composition, and carbon conversion. Results show that higher temperatures are favorable for the products in endothermic reactions (e.g. H_2 and CO). With the increase of steam/biomass mass ratio, H_2 and CO_2 concentrations increase while CO concentration decreases. The carbon conversion decreases as the height of injection point increases owing to both an increase of solid entrainment and a decrease of particle residence time and particle temperature. Meanwhile, the integrated model has also been validated by comparing the calculated results with the experimental data. This indicates that the proposed CFD–DEM model can provide not only the macro structures at fluidized bed scale (bubble or slug) but also detailed microscopic information at the particle level (such as particle trajectory, particle–particle interaction, particle entrainment, and particle reaction, see Figs. 5, 8 and 14) which is impossible to obtain by an Eulerian–Eulerian approach. So our proposed model can be a powerful tool to gain an insight into the complex dense gas–particle flow behaviors and chemical reaction characteristics

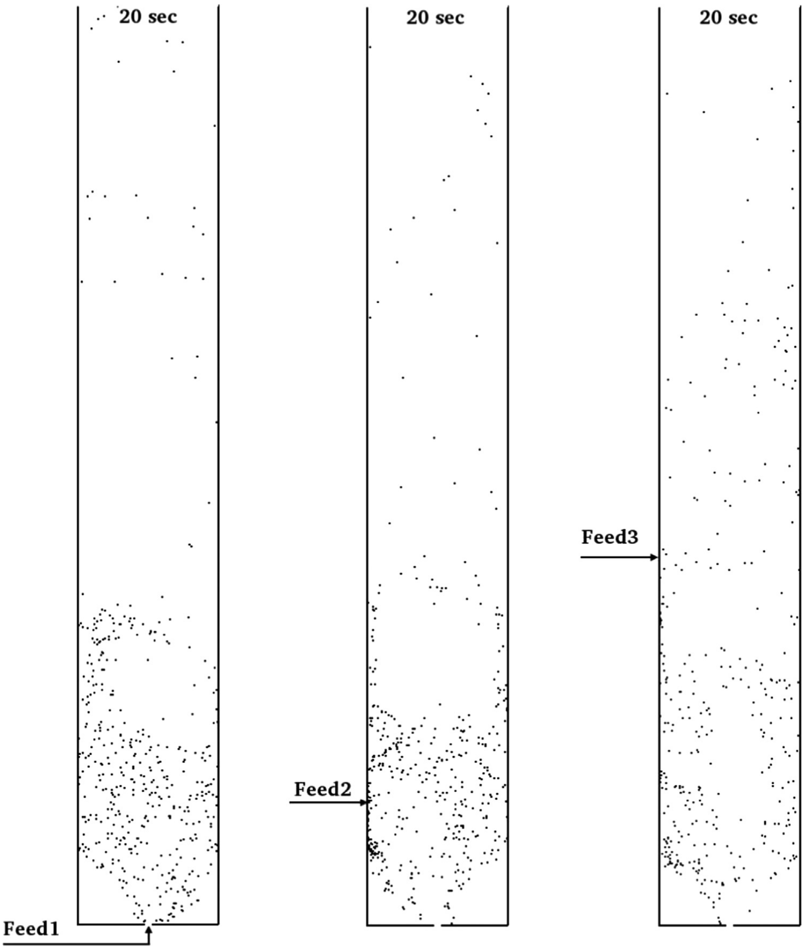

Fig. 14. Biomass particle distributions at the end of simulation for three different injection positions. Note that sand particles are excluded for clarity purpose. T_r=820 °C, S/B=1.2.

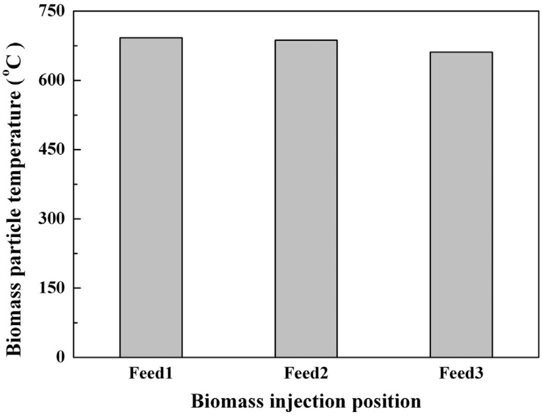

Fig. 15. Average biomass particle temperature for the three different injection positions. T_r=820 °C, S/B=1.2.

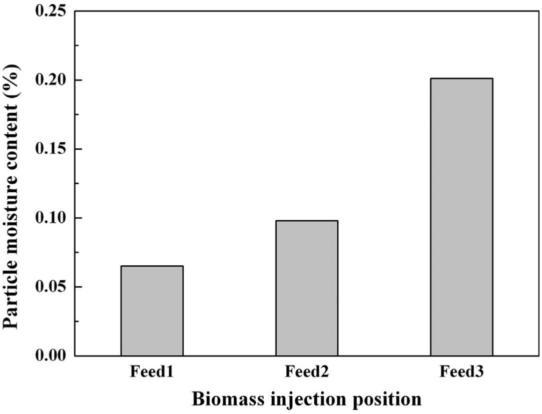

Fig. 16. Average moisture content of biomass particles for the three different injection positions. T_r=820 °C, S/B=1.2.

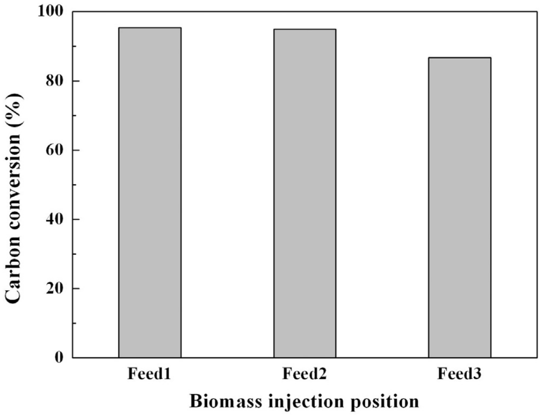

Fig. 17. Carbon conversion at the reactor outlet for the three different injection positions. $T_r = 820\ ^\circ\text{C}$, $S/B = 1.2$.

simultaneously in the process of biomass gasification in a fluidized bed reactor.

Nomenclature

A	pre-exponential factor, 1/s
A_p	particle surface area, m^2
c_p	specific heat of particle, J/(kg K)
C_d	drag coefficient, dimensionless
$C_{\varepsilon 1}$, $C_{\varepsilon 2}$	model constants for ε equation
d_p	particles diameter, m
$dm_{\text{C-H}_2\text{O}}$	change in mass of particle due to char reaction R2, kg
$dm_{\text{C-CO}_2}$	change in mass of particle due to char reaction R1, kg
dm_{devol}	change in mass of particle due to devolatilization, kg
dm_{vapor}	change in mass of particle due to loss of water vapor, kg
D_{eff}	effective mass diffusion coefficient for gas, m^2/s
e_p	particle emissivity, dimensionless
E	activation energy, J/kmol or parameter in Eq. (18), J/kg
$\mathbf{f}_c$	total contact force acting on particle due to collision, N
$\mathbf{f}_g$	gas drag force acting on particle, N
$\mathbf{g}$	gravitational acceleration, m/s^2
G	incident radiation, kg/s^3
G_k	generation term for k
h	heat transfer coefficient, $\text{W/(m}^2\ \text{K)}$
h_s	sensible enthalpy of gas phase, J/kg
I_p	moment of inertia of particle, kg m^2
k	reaction kinetics, $\text{kmol/(m}^3\ \text{s)}$ or turbulent kinetic energy, m^2/s^2
m_p	particle mass, kg
p	gas pressure, Pa
p_i	partial pressure of gas species i, Pa
Q_p	energy source term in particle energy equation, W
R	universal gas constant, J/(kmol K)
Re_p	particle Reynolds number, dimensionless
S_h	enthalpy source term due to homogeneous reactions, W/m^3
$S_{p,m}$	mass source term from particle phase, $\text{kg/(m}^3\ \text{s)}$
$S_{p,h}$	enthalpy source term from particle phase, W/m^3
S_{rad}	radiation source term in gas phase energy equation, W/m^3
S_{p,Y_i}	species source term from particle phase, $\text{kg/(m}^3\ \text{s)}$
S_{Y_i}	species source term due to homogeneous reactions, $\text{kg/(m}^3\ \text{s)}$
$S_{p,\text{mom}}$	momentum source term, N/m^3
t	time, s
T_g	gas temperature, K
T_p	particle temperature, K
$\mathbf{T}_p$	torque acting on particle, $\text{kg m}^2/\text{s}^2$
$\mathbf{u}_g$	gas velocity, m/s
$\mathbf{v}_p$	particle velocity, m/s
V_p	particle volume, m^3
Y_i	mass fraction of species i, dimensionless

Greek letters

α_{eff}	effective thermal diffusivity, kg/(m s)
β	inter-phase momentum exchange coefficient, $\text{kg/(m}^3\ \text{s)}$
ε	dissipation rate of turbulent kinetic energy, m^2/s^3
ε_g	volume fraction of gas, dimensionless
ε_p	volume fraction of particle, dimensionless
μ_g	gas phase viscosity, kg/(m s)
μ_t	turbulent viscosity, kg/(m s)
ρ_g	gas density, kg/m^3
ρ_p	particle density, kg/m^3
σ	Stefan–Boltzmann constant, $\text{W/(m}^2\ \text{K}^4\text{)}$
σ_κ	constant in Eq. (20)
σ_ε	constant in Eq. (21)
$\boldsymbol{\tau}_{\text{eff}}$	effective stress tensor, Pa
$\boldsymbol{\omega}_p$	particle angular velocity, 1/s

Subscripts

c	contact
g	gas phase
i	genreral index
p	particle
t	turbulent

Abbreviations

CC	carbon conversion
CFD	computational fluid dynamics
daf	dry and ash free
DEM	discrete element method
FB	fluidized bed
syngas	synthetic gas

Acknowledgments

The authors would like to thank partners in CenBio, the BioEnergy Innovation Centre, and GasBio for financial support.

References

Abani, N., Ghoniem, A.F., 2013. Large eddy simulations of coal gasification in an entrained flow gasifier. Fuel 104, 664–680.

Backreedy, R.I., Fletcher, L.M., Ma, L., Pourkashanian, M., Williams, A., 2006. Modelling pulverised coal combustion using a detailed coal combustion model. Combust. Sci. Technol. 178, 763–787.

Boyalakuntla, D.S., 2003. Simulation of Granular and Gas–Solid Flows using Discrete Element Method (Ph.D. thesis). Carnegie Mellon University, Pittsburgh, Pennsylvania.

Bruchmüller, J., van Wachem, B.G.M., Gu, S., Luo, K.H., Brown, R.C., 2012. Modeling the thermochemical degradation of biomass inside a fast pyrolysis fluidized bed reactor. AIChE J. 58 (10), 3030–3042.

Chen, W., Chen, C., Hung, C., Shen, C., Hsu, H., 2013. A comparison of gasification phenomena among raw biomass, torrefied biomass and coal in an entrained-flow reactor. Appl. Energy 112, 421–430.

Cundall, P.A., Strack, O.D.L., 1979. A discrete numerical model for granular assemblies. Geotechnique 29, 47–65.

Ergun, S., 1952. Fluid flow through packed columns. Chem. Eng. Prog. 48, 89–94.

Ergüdenler, A., Ghaly, A.E., Hamdullahpur, F., Al-Taweel, A.M., 1997. Mathematical modeling of a fluidized bed straw gasifier: Part I—model development. Energy Source 19, 1065–1084.

Gerber, S., Behrendt, F., Oevermann, M., 2010. An Eulerian modeling approach of wood gasification in a bubbling fluidized bed reactor using char as bed material. Fuel 89, 2903–2917.

Gerber, S., Oevermann, M., 2014. A two dimensional Euler–Lagrangian model of wood gasification in a charcoal bed – Part I: model description and base scenario. Fuel 115, 385–400.

Gidaspow, D., 1994. Multiphase Flow and Fluidization. Academic Press, San Diego, USA.

Gil, J., Corella, J., Aznar, M.P., Caballero, M.A., 1999. Biomass gasification in atmospheric and bubbling fluidized bed: effect of the type of gasifying agent on the product distribution. Biomass Bioenergy 17, 389–403.

Gómez-Barea, A., Leckner, B., 2010. Modeling of biomass gasification in fluidized bed. Prog. Energy Combust. 36, 444–509.

Hoomans, B.P.B., Kuipers, J.A.M, Briels, W.J., van Swaaij, W.P.M., 1996. Discrete particle simulation of bubble and slug formation in a two-dimensional gas fluidised bed: a hard-sphere approach. Chem. Eng. Sci. 51, 99–118.

Jones, W.P., Lindstedt, R.P., 1988. Global reaction schemes for hydrocarbon combustion. Combust. Flame 73, 233–249.

Kafui, K.D., Thornton, C., Adams, M.J., 2002. Discrete particle-continuum fluid modelling of gas–solid fluidised beds. Chem. Eng. Sci. 57, 2395–2410.

Kern, S., Pfeifer, C., Hofbauer, H., 2013. Gasification of wood in a dual fluidized bed gasifier: influence of fuel feeding on process performance. Chem. Eng. Sci. 90, 284–298.

Kim, Y.D., Yang, C.W., Kim, B.J., Kim, K.S., Lee, J.W., Moon, J.H., Yang, W., Yu, T.U., Lee, U.D, 2013. Air-blown gasification of woody biomass in a bubbling fluidized bed gasifier. Appl. Energy 112, 414–420.

Ku, X., Li, T., Løvås, T., 2013. Influence of drag force correlations on periodic fluidization behavior in Eulerian–Lagrangian simulation of a bubbling fluidized bed. Chem. Eng. Sci. 95, 94–106.

Kumar, M., Ghoniem, A.F., 2012. Multiphysics simulations of entrained flow gasification. Part II: constructing and validating the overall model. Energy Fuels 26, 464–479.

Lathouwers, D., Bellan, J., 2001. Modeling of dense gas-solid reactive mixtures applied to biomass pyrolysis in a fluidized bed. Int. J. Multiph. Flow 27 (12), 2155–2187.

Li, X.T., Grace, J.R., Lim, C.J., Watkinson, A.P., Chen, H.P., Kim, J.R., 2004. Biomass gasification in a circulating fluidized bed. Biomass Bioenergy 26, 171–193.

Liu, D., Chen, X., Zhou, W., Zhao, C., 2011. Simulation of char and propane combustion in a fluidized bed by extending DEM–CFD approach. Proc. Combust. Inst. 33, 2701–2708.

Meng, X., de Jong, W., Fu, N., Verkooijen, A.H.M., 2011. Biomass gasification in a 100 kWth steam-oxygen blown circulating fluidized bed gasifier: effects of operational conditions on product gas distribution and tar formation. Biomass Bioenergy 35, 2910–2924.

Nikoo, M.B., Mahinpey, N., 2008. Simulation of biomass gasification in fluidized bed reactor using ASPEN PLUS. Biomass Bioenergy 32 (12), 1245–1254.

OpenCFD Ltd, 2012. OpenFOAM-The open source CFD toolbox-user guide (Version 2.1.1) ⟨http://www.openfoam.org/docs/⟩.

Papadikis, K., Gu, S., Bridgwater, A.V., 2010. A CFD approach on the effect of particle size on char entrainment in bubbling fluidised bed reactors. Biomass Bioenergy 34, 21–29.

Prakash, N., Karunanithi, T., 2008. Kinetic modeling in biomass pyrolysis – a review. J. Appl. Sci. Res. 4 (12), 1627–1636.

Qin, K., Jensen, P.A., Lin, W., Jensen, A.D., 2012. Biomass gasification behavior in an entrained flow reactor: gas product distribution and soot formation. Energy Fuels 26, 5992–6002.

Sadaka, S.S., Ghaly, A.E., Sabbah, M.A., 2002. Two phase biomass air-steam gasification model for fluidized bed reactors: Part I—model development. Biomass Bioenergy 22, 439–462.

Shen, L., Gao, Y., Xiao, J., 2008. Simulation of hydrogen production from biomass gasification in interconnected fluidized beds. Biomass Bioenergy 32, 120–127.

Snider, D.M., Clark, S.M., O'Rourke, P.J., 2011. Eulerian–Lagrangian method for three-dimensional thermal reacting flow with application to coal gasifiers. Chem. Eng. Sci. 66, 1285–1295.

Song, T., Wu, J., Shen, L., Xiao, J., 2012. Experimental investigation on hydrogen production from biomass gasification in interconnected fluidized beds. Biomass Bioenergy 36, 258–267.

Taghipour, F., Ellis, N., Wong, C., 2005. Experimental and computational study of gas–solid fluidized bed hydrodynamics. Chem. Eng. Sci. 60, 6857–6867.

Tsuji, Y., Kawaguchi, T., Tanaka, T., 1993. Discrete particle simulation of two-dimensional fluidized bed. Powder Technol. 77, 79–87.

Tsuji, Y., Tanaka, T., Ishida, T., 1992. Lagrangian numerical simulation of plug flow of cohesionless particles in a horizontal pipe. Powder Technol. 71, 239–250.

Wang, X., Jin, B, Zhong, W., 2009. Three-dimensional simulation of fluidized bed coal gasification. Chem. Eng. Process. 48, 695–705.

Warnecke, R., 2000. Gasification of biomass: comparison of fixed bed and fluidized bed gasifier. Biomass Bioenergy 18, 489–497.

Wen, C.Y., Yu, Y.H., 1966. Mechanics of fluidization. Chem. Eng. Prog. Symp. Ser. 62, 100–111.

Xie, J., Zhong, W., Jin, B., Shao, Y., Huang, Y., 2013. Eulerian–Lagrangian method for three-dimensional simulation of fluidized bed coal gasification. Adv. Powder Technol. 24, 382–392.

Xu, B.H., Yu, A.B., 1997. Numerical simulation of the gas–solid flow in a fluidized bed by combining discrete particle method with computational fluid dynamics. Chem. Eng. Sci. 52, 2785–2809.

Appendix: Additional publication

Paper VI

Numerical investigation on turbulent dispersion of particles in channel flow

Tian Li, Lihao Zhao, Xiaoke Ku, Helge I. Andersson, Terese Løvås

Thermal Science, 160, 1510-1514, 2012

NUMERICAL INVESTIGATION OF PARTICLES TURBULENT DISPERSION IN CHANNEL FLOW

by

Tian LI*[*], Li-Hao ZHAO, Xiao-Ke KU, Helge ANDERSSON,
and Terese LOVAS

Department of Energy and Process Engineering, Norwegian University of
Science and Technology, Trondheim, Norway

Short paper
DOI: 10.2298/TSCI1205510L

This paper investigates the performance of Reynolds-averaged Navier-Stokes model on dispersion of particles in wall turbulence. A direct numerical simulation of wall-bounded channel flow with particles suspensions was set as a benchmark. The standard k–ω model coupled with two different eddy interaction models was used in Reynolds-averaged Navier-Stokes model and compared to the direct numerical simulation. Detailed comparisons between direct numerical simulation and Reynolds-averaged Navier-Stokes model on particle distribution evolving over time were carried out.

Key words: *turbulent dispersion, eddy interaction model, particle distribution, direct numerical simulation*

Introduction

Turbulent particle-laden flow is a significant feature in many industry applications. One of the most widely used methods is Eulerian-Lagrangian approach. Taking the advantage of complete fluid velocity information from direct numerical simulation (DNS), treatment of the particle tracking becomes straightforward. Turbulent dispersion of particles is explicitly obtained by drag through the fluid velocity fluctuations. Eaton *et al.* [1] performed the DNS and experiments on the particle preferential concentration in turbulence. Marchioli *et al.* [2] found that sweeps and ejections are efficient transfer mechanisms for particles. Lin *et al.* [3] explored the effect of Stokes number, density ratio and aspect ratio on the particle spatial and orientation distributions. Yamamoto *et al.* [4] performed a four-way coupled large eddy simulations (LES) in a vertical channel and obtained a good agreement with experimental data. Yu *et al.* [5, 6] performed a LES on nanoparticle coagulation in the planar jet flow and on nucleated vehicle exhaust particulate. However, both DNS and LES are time consuming. More commonly, empirical equations or Reynolds-averaged Navier-Stokes (RANS) models are chosen. Unfortunately, due to lack of turbulent velocity fluctuations information, turbulent dispersion of particles has to be modeled. Lin *et al.* [7] adopted a Fourier series and studied orientation distribution of fibers immersed in turbulent pipe flows. Zhang *et al.* [8] and Lin *et*

---

[*] Corresponding author; e-mail: tian.li@ntnu.no

al. [9] assumed the fluctuating velocities of the fluid as a random variable with Gaussian distribution and investigated the orientation of cylindrical particles in a turbulent T-shaped branching channel flow and a turbulent contraction flow. Smith *et al.* [10] studied particle motion using diffusion force. However, in the model a diffusion coefficient is obscure and usually difficult to be determined. To overcome this, a novel approach called stochastic particle dispersion model was presented. Eddy interaction models (EIM) has been widely applied and also plenty of modified EIM models were proposed. Graham [11] developed an improved EIM model with random length and time scales. Chen [12] studied particle dispersion in inhomogeneous, anisotropic turbulent flows by using Reynolds-stress transport model. Agnihotri *et al.* [13] presented an anisotropic EIM and studied mono-disperse aerosols in a simplified human upper airway and a 90° bend pipe. Among the literatures mentioned above, detailed comparison between DNS and RANS model results on particle distribution is rarely reported. The present study aims to evaluate the performance of RANS model with EIM by comparing the results of particle distribution obtained by DNS.

Modeling approach

The standard k–ω model with low Reynolds number corrections is used to simulate the fluid phase. The trajectories of particle are solved in a Lagrangian frame. The only force taken into account is the Stokes drag $\boldsymbol{F}$. The dispersion of particles is caused by the fluid fluctuation velocity $\boldsymbol{u}'_f$. By using Reynolds decomposition of the fluid velocity, the force acting on the particle is decomposed as $\boldsymbol{F} = 3\pi\mu d(\boldsymbol{u}_f - \boldsymbol{u}_p) = 3\pi\mu d(\boldsymbol{U}_f - \boldsymbol{u}_p) + 3\pi\mu d\boldsymbol{u}'_f$ (μ is the viscosity of the fluid, d – the particle diameter, $\boldsymbol{u}_f$ – the fluid velocity, $\boldsymbol{U}_f$ – the fluid mean velocity, and $\boldsymbol{u}_p$ – the particle velocity). EIM simulates the turbulent dispersion of particles as a succession of interactions between fluid eddies and particles, in which the interaction time t_{int} and velocity fluctuations $\boldsymbol{u}'_f$ both need to be modeled. For t_{int}, the eddy lifetime t_{e} and the particle crossing time t_{c} should be calculated firstly: $t_{\mathrm{e}} = -C_l \ln(r)(k/\varepsilon)$ and $t_c = -\tau_{\mathrm{p}} \ln[1 - (l_e/u_{\mathrm{rel}}\,\tau_{\mathrm{p}})]$ (C_l is a coefficient, r – a random number between 0 and 1, τ_{p} – the particle relaxation time, l_e – the eddy length scale, and u_{rel} – the relative velocity between local fluid and particle). By using t_{c} and t_{e}, the t_{int} can then be determined as $t_{\mathrm{int}} = t_e$, if $u_{\mathrm{rel}} < l_e/\tau_{\mathrm{p}}$, otherwise, $t_{int} = \min(t_{\mathrm{e}}, t_{\mathrm{c}})$. The fluid velocity fluctuations $\boldsymbol{u}'_f$ in terms of Cartesian components are modeled as $u' = v' = w' = \xi\,(2k/3)^{1/2}$, where ξ is a Gaussian random number with zero mean and unit standard deviation. After an interaction time t_{int}, a new value of the velocity fluctuations is obtained by applying a new random number.

Anisotropic eddy interaction model

The original EIM model is based on an isotropic assumption. However, the flow field is indeed not isotropic in wall turbulence. By using damping functions, Wang *et al.* [14] provided a modified EIM which can account for the effects of anisotropy. The damping functions are given by Kim *et al.* [15] and Mansour *et al.* [16]. The fluid velocity fluctuations with the damping functions are [15]: $u' = f_u\xi(2k/3)^{1/2}$, $v' = f_v\xi(2k/3)^{1/2}$, $w' = f_w\xi(2k/3)^{1/2}$, $f_u = 1 + 0.285(y^+ + 6)\exp[-0.455(y^+ + 6)^{0.53}]$, $f_v = 1 - \exp(-0.02\,y^+)$, $f_u = (3 - f_u^2 - f_v^2)^{1/2}$, and y^+ is the dimensionless wall distance). The interaction time as discussed above is modeled in the same manner, including the definitions of the eddy life time and particle crossing time.

Numerical set-up

Figure 1 shows the calculation domain. Apart from non-slip boundaries of the upper and lower walls, all the other boundaries are imposed with periodic boundary conditions. The turbulent channel flow was driven by a constant pressure gradient with $\mathrm{Re}_\tau = 360$ [17]. The Re_τ is defined as $\mathrm{Re}_\tau = U_\tau h/\nu$ (U_τ is the friction velocity, h – the channel height and ν – the kinematic viscosity of the fluid). The pseudo-spectral DNS code consists of 192^3 grid nodes. The mesh contains 31 × 41 × 31 grid points. The particle initial velocity equals to local fluid velocity. The dimensionless relaxation time τ^+ is 30, particle dimensionless diameter d^+ – 0.72, density ratio ρ_p/ρ_f – 1041.7 (ρ_p – the particle density, ρ_f – the fluid density), and the total number of particles N_p is 10^5.

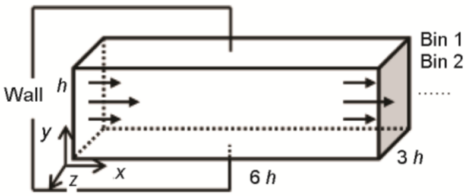

Figure 1. Sketch of the channel model

Results and discussions

To enable an in-depth exploration of turbulent dispersion of particles, the channel was evenly divided into 20 bins in wall-normal direction as shown in fig. 1. The number of particles in each bin was counted and results from bin 1, 4, 7, and 10 are shown in fig. 2. Because of the symmetrical channel, a clear picture of particle distribution evolution can be constructed by the information from those four bins.

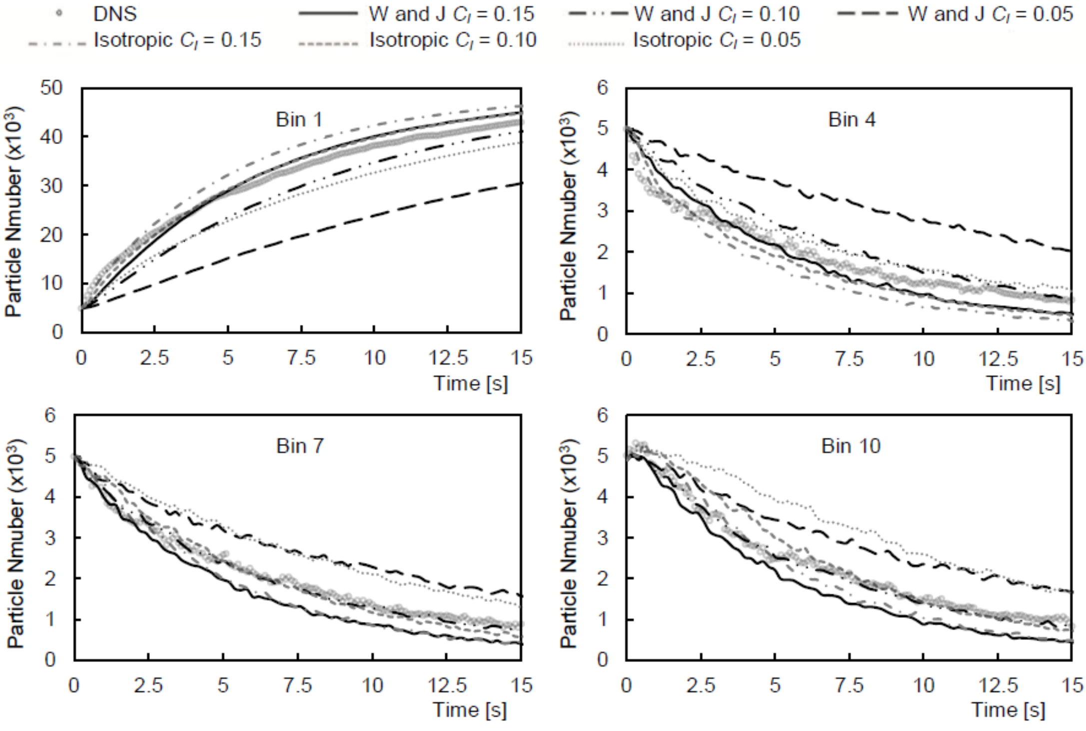

Figure 2. Particle distribution evolution (W and J stands for EIM [14] and isotropic is original EIM)

As shown in fig. 2, a steady increase of the particle number in Bin 1, which is closest to the wall, can be observed. The particle numbers in other bins decreased, *i. e.*, particles in the channel center tend to migrate to the wall. According to the data in fig. 2, the particle numbers in selected bins predicted in EIM [14] is in better agreement with the DNS results than the results given by the original isotropic EIM. The velocity fluctuations in the original EIM cause great deviations of v'. It is the overproduction of v' which accelerates the particle dispersion rate by providing particles with a stronger drag force in wall-normal direction. Consequently, the particle numbers in Bin 4, 7, and 10 reduced faster than DNS result, while correspondingly particle number in Bin 1 increased much faster. With Fluent default setting ($C_l = 0.15$), neither the original EIM nor the EIM [14] can give satisfactory results of particle dispersion. A larger C_l could extend the interaction time between particle and fluid, which also indicates stronger turbulent dispersion effect. By adjusting C_l, the overall optimum is found around 0.10 for EIM [14].

Conclusions

It has been shown that the original isotropic EIM cannot fully reproduce the particle distribution development calculated by DNS. However, with EIM [14], RANS model can give more reasonable particle distribution prediction. By adjusting C_l, the optimal overall distribution trend was obtained when C_l equals to around 0.10 with EIM [14].

Acknowledgments

This work was carried out within the competence building project GasBio, funded by the Research Council of Norway, four International industry partners, and SINTEF Energy Research.

References

[1] Eaton, J. K., Fessler, J. R., Preferential Concentration of Particles by Turbulence, *Int. J. Multiphase Flow, 20* (1994), Suppl. 1, pp. 169-209

[2] Marchioli, C., Soldati, A., Mechanisms for Particle Transfer and Segregation in Turbulent Boundary Layer, *J. Fluid Mech., 468* (2002), pp. 283-315

[3] Lin, J. Z., Shi, X., Yu, Z. S., The Motion of Fibers in an Evolving Mixing Layer, *Int. J. Multiphase flow, 29* (2003), 8, pp. 1355-1372

[4] Yamamoto, Y., *et al*., Large-Eddy Simulation of Turbulent Gas Particle Flow in a Vertical Channel: Effect of Considering Inter-Particle Collisions, *J. Fluid Mech., 422* (2001), pp. 303-334

[5] Yu, M. Z., *et al*., Large Eddy Simulation of a Planar Jet Flow with Nanoparticle Coagulation, *Acta Mechanica Sinica, 22* (2006), 4, pp. 293-300

[6] Yu, M. Z., Lin, J. Z., Chan, T. L., Numerical Simulation for Nucleated Vehicle Exhaust Particulate Matters via the TEMOM/LES Method, *Int. J. of Modern Physics C, 20* (2009), 3, pp. 399-421

[7] Lin, J. Z., Zhang, W. F., Yu, Z. S., Numerical Research on the Orientation Distribution of Fibers Immersed in Laminar and Turbulent Pipe Flows, *J. of Aerosol Sci., 35* (2004), 1, pp. 63-82

[8] Zhang, S. L., Lin, J. Z., Zhang, W. F., Numerical Research on the Fiber Suspensions in a Turbulent T-Shaped Branching Channel Flow, *Chinese J. Chem. Eng., 15* (2007), 1, pp. 30-38

[9] Lin, J. Z., Zhang, S. L., Olson, J. A., Computing Orientation Distribution and Rheology of Turbulent Fiber Suspensions Flowing through a Contraction, *Eng. Computations, 24* (2007), 1, pp. 52-76

[10] Smith, P. J., Fletcher, T. H., Smoot, L. D., Model for Pulverized Coal-Fired Reactors, *Proceedings,* Symp. (Int.) on Combustion, Waterloo, Ont., Canada, The Combustion Institute, 1981, pp. 1285-1293

[11] Graham, D. I., Improved Eddy Interaction Models with Random Length and Time Scales, *Int. J. Multiphase Flow, 24* (1998), pp. 2, 335-345

[12] Chen, X. Q., Heavy Particle Dispersion in Inhomogeneous, Anisotropic, Turbulent Flows, *Int. J. Multiphase Flow, 26* (2000), 4, pp. 635-661
[13] Agnihotri, V., *et al*., An Eddy Interaction Model for Particle Deposition, *J. Aerosol Sci., 47* (2012), 1, pp. 39-47
[14] Wang, Y., James, P. W., On the Effect of Anisotropy on the Turbulent Dispersion and Deposition of Small Particles, *Int. J. Multiphase Flow, 25* (1999), 3, pp. 551-558
[15] Kim, J., Moin, P., Moser, R., Turbulence Statistics in Fully Developed Channel Flow at Low Reynolds Number, *J. Fluid Mech., 177* (1987), pp. 133-166
[16] Mansour, N. N., Kim, J., Moin, P., Reynolds-Stress and Dissipation-Rate Budgets in a Turbulent Channel Flow, *J. Fluid Mech., 194* (1988), pp. 15-44
[17] Zhao, L. H., Andersson, H. I., Gillissen, J. J., Turbulence Modulation and Drag Reduction by Spherical Particles, *Phys. Fluids, 22* (2010), pp. 1702-1708

Paper submitted: August 1, 2012
Paper revised: September 1, 2012
Paper accepted: September 12, 2012